Computational and Experimental Studies of Dye Sensitized Solar Cells

A DISSERTATION
SUBMITTED TO THE FACULTY OF THE GRADUATE SCHOOL
OF THE UNIVERSITY OF MINNESOTA
BY

Rajan Vatassery

IN PARTIAL FULFILLMENT OF THE REQUIREMENTS
FOR THE DEGREE OF
Doctor of Philosophy

Wayne L Gladfelter

September, 2013

Acknowledgements

As I start thinking about who I would like to acknowledge for the successes in my graduate career, I am realizing I should warn the reader that because I took almost twice as long as I should have to complete my PhD, this acknowledgment section should contain about twice as many acknowledgments as well. The reasons for my extended stay in graduate school primarily involved the fact that I started out as an immature student in my early 20s who could not challenge the opinions of "real scientists," working on a project that was particularly challenging for two bosses who did not have experience in that project's subject area. As is said in relation to plane crashes, it was a combination of factors that led to my difficulties and failures, not one factor alone.

In times of difficulty, the people around me mattered most. Beth was always needed and always available; Troy, Margaret, Kathryn, and Mike made it seem like things could be normal once in a while; Pirmin, Brian, Patricia, Brad, Jon, Brandon, Sina, Ian, and Zach formed an unbelievable support network that was invaluable. It would be incredibly difficult to enumerate all the people that helped me out in Chicago because I needed so much help, but the Connell/DePriest family and the Smiths definitely need to be included.

Getting back up off the ground was made much easier because of people like SonBinh, Ramakrishna, and Dr. Miessler who not only vouched for my abilities as a scientist, but also took a personal interest in my success. SonBinh and Dr. Miessler combined taught me most of what I know about how to be a good scientist and how to interrogate data. The start of my upswing to my current position was precipitated by my current adviser Wayne, who plucked me off the graduate student scrap-heap in 2008, and also by Ilja who played a key role in this process. It is interesting that the two people most responsible for my admission to the U of M are the corresponding authors on my two

manuscripts.

At the U of M the successes I achieved were in part because of help from friends and colleagues such as Raghu, Ryan, Kyle (and Christy), Darren, Vince, Toni, Jon, Letitia, Jason, and Chuck, even if they simply listened to my endless complaints, although most of these people did much more. Stephen, Kent, David, and Gregg were very helpful as sounding boards for my ideas.

Throughout the difficulties and successes I experienced in graduate school, my friends from high school and college and my family have been constantly present. My friends from SPA and St Olaf College do not need to be named because they certainly know already how much they have helped. My parents and Jayan have always been able to provide for me and protect me from my own poor choices. My family as a whole — my first teachers and my most important influences — worked with me as a very stubborn young child who did not want to listen to them and made me appreciate that the world was too big and complicated to be arrogant. Because of them (as well as Mrs. Victor), I never will confuse having a well-founded argument with simply making an argument in a strong voice. I am lucky that my family now includes my best friend, Sunayana, and her family as well, all of whom have had a large, positive influence in my life.

Even though few people will read this, it is still unfortunate that there are many people that I will inadvertently leave out. However, I want to thank Derek and Melanie, Ramki Uncle, Tim and Colleen, Archana, and Doug and Maren for supporting Sunayana and I in ways that only they could.

Lastly, I want to share with the reader a poem that helped me along when times were tough. The poem is especially meaningful to me because of the gamble that I took at Northwestern, and my eventual success at the University of Minnesota. I hope that it is able to provide hope to someone else who is currently in the situation I was about 6 years ago.

If you can keep your head when all about you
Are losing theirs and blaming it on you,
If you can trust yourself when all men doubt you,
But make allowance for their doubting too;
If you can wait and not be tired by waiting,
Or being lied about, don't deal in lies,
Or being hated, don't give way to hating,
And yet don't look too good, nor talk too wise:

If you can dream — and not make dreams your master;
If you can think — and not make thoughts your aim;
If you can meet with Triumph and Disaster
And treat those two impostors just the same;
If you can bear to hear the truth you've spoken
Twisted by knaves to make a trap for fools,
Or watch the things you gave your life to, broken,
And stoop and build 'em up with worn-out tools:

If you can make one heap of all your winnings
And risk it on one turn of pitch-and-toss,
And lose, and start again at your beginnings
And never breathe a word about your loss;
If you can force your heart and nerve and sinew
To serve your turn long after they are gone,
And so hold on when there is nothing in you
Except the Will which says to them: 'Hold on!'

If you can talk with crowds and keep your virtue,
Or walk with Kings — nor lose the common touch,
If neither foes nor loving friends can hurt you,
If all men count with you, but none too much;
If you can fill the unforgiving minute
With sixty seconds' worth of distance run,
Yours is the Earth and everything that's in it,
And — which is more — you'll be a Man, my son!

Rudyard Kipling (1895)

Contents

List of Tables

List of Figures

Chapter 1

Introduction

1.1 Background of Solar Energy

Alternative means for generation of electricity have been sought after for many years. The reasons for the focused effort are geopolitical, ethical, and economic. Currently, the United States uses a vast majority of non-renewable resources for electricity generation (Figure 1.1). The country's continued dependence on these resources contributes to economic and geopolitical instability, and environmental degradation.

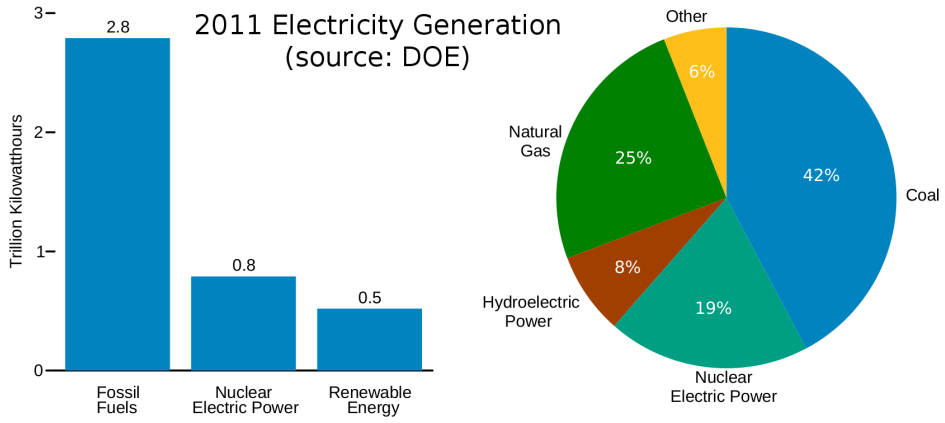

Figure 1.1: Left: Graph showing contributions from various sectors to overall electricity production in 2011. Right: Pie chart showing electricity generation with solar energy included in the "other" category.

Solar energy is an attractive option for generation of electrical energy because it has the possibility of being cheap, clean, and local. Consequently, the solar energy field has been advancing since its inception (Figure 1.2).[1] The available technologies to utilize solar energy for electricity generation include silicon p-n junction solar cells, dye sensitized solar cells (DSSCs), and multijunction solar cells.

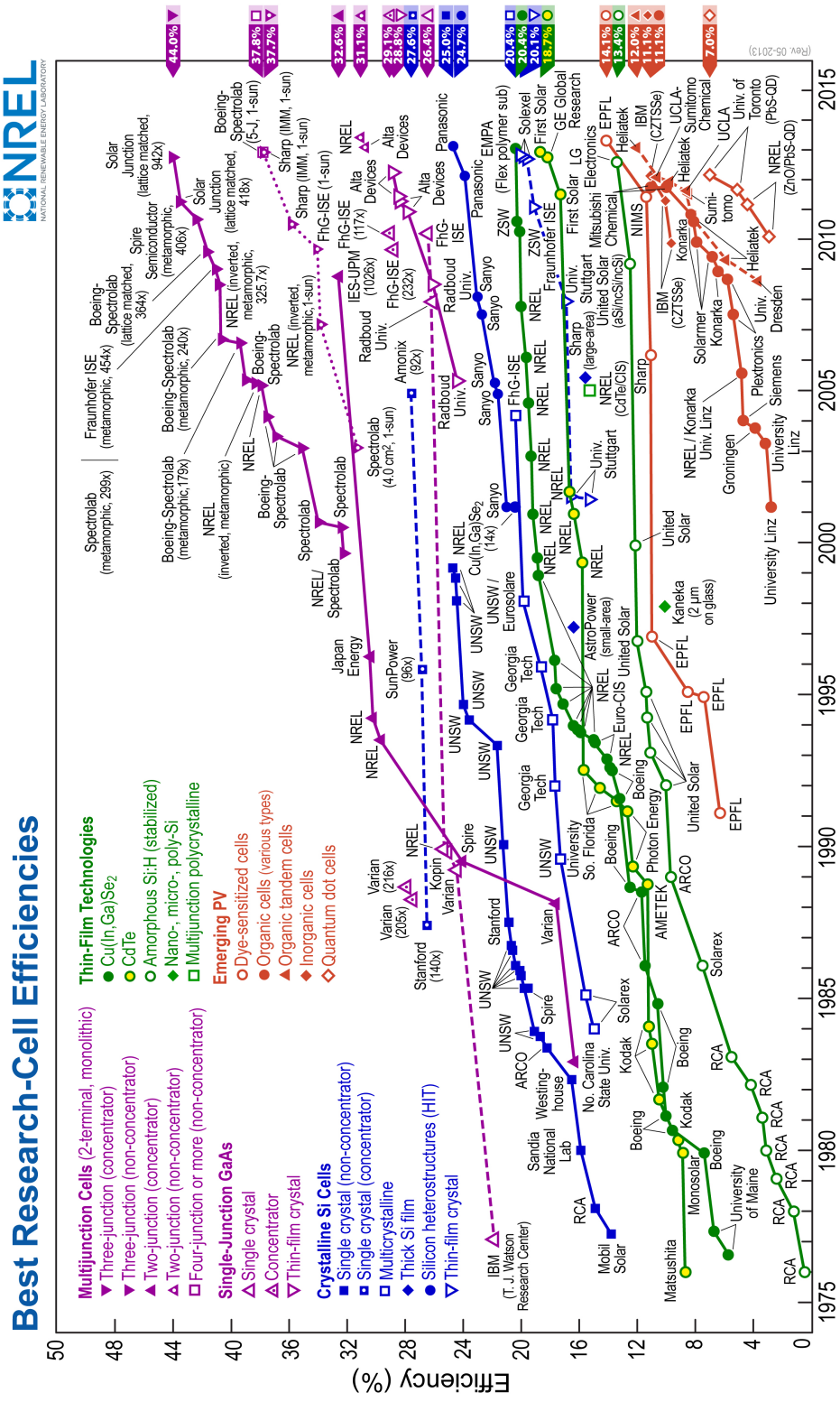

Figure 1.2: Improvement of Solar Power Conversion Cells since 1975 [2]

1.1.1 Silicon p-n junction solar cells

The p-n junction solar cell has traditionally been the most common type of solar cell in production.[1] It consists of a region of p-doped silicon juxtaposed with a region of n-doped silicon. The spatial confluence of these regions is the p-n junction. At this junction, the intrinsic bias voltage allows an exciton to be separated into an electron and a hole, thereby creating the current necessary to power an external load (Figure 1.3).

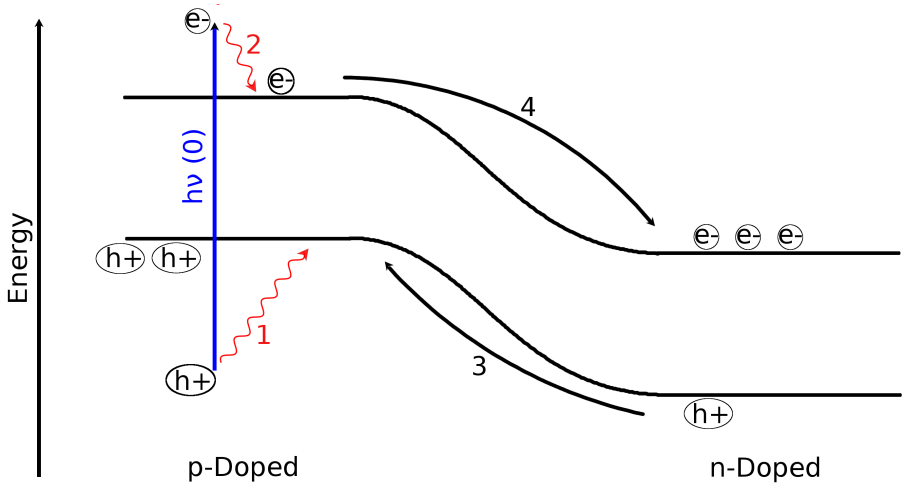

Figure 1.3: Schematic of a p-n junction functioning as a solar cell, where process 0 initiates the creation of an exciton, process 1 and process 2 correspond to hot carrier relaxation to band edge states by the hole and electron, respectively, and process 3 and 4 correspond to charge carrier rectification across the pn junction in the form of holes and electrons moving, respectively.

The simplicity of the silicon p-n junction leads to its durability; these cells are known to retain 85% of the module's original efficiency even after many decades.[3] However, it also leads to a reduction in efficiency because as the exciton is generated each carrier will relax non-radiatively (thermalize), losing any energy obtained from the incoming light in excess of the band gap (processes 1 and 2 in Figure 1.3). In the Shockley-Queisser approximation of "detailed balance," the efficiency limit for a single junction cell of this type is about 32%.[4] While this figure rivals the efficiency of the nation's

electricity production via fossil fuels (see Figure 1.4), solar energy's spatially diffuse nature would require a very large area to produce a similar power output, even if the unrealistic circumstance of reaching the Shockley-Queisser limit was achieved.

An advantage that silicon p-n junction solar cell technology possesses is that a vast amount of information is available on silicon processing. This is due to the past century's enormous advances in microchip development. In fact, when manufacture of crystalline silicon cells was still small scale, it was possible to use high-quality, leftover silicon from the microchip industry for solar cells. But the surge in demand for solar power has necessitated additional sources of highly pure silicon wafers. Since many of the silicon p-n junction solar cells are zone-refined, this process remains a high-energy requirement for generation of silicon solar cells.[5]

Advances past the traditional single crystal, zone-refined p-n junction cells abound in the literature. Polycrystalline and amorphous silicon are both attractive possibilities, but underdeveloped technologically. Multijunction solar cells also get attention due to their consistently high performance, but their complexity renders them cost effective only for space programs. Dye sensitized solar cells are another main player in the research community because of their potential to be cheaply and quickly assembled, and without the requirement for substantial energy inputs.

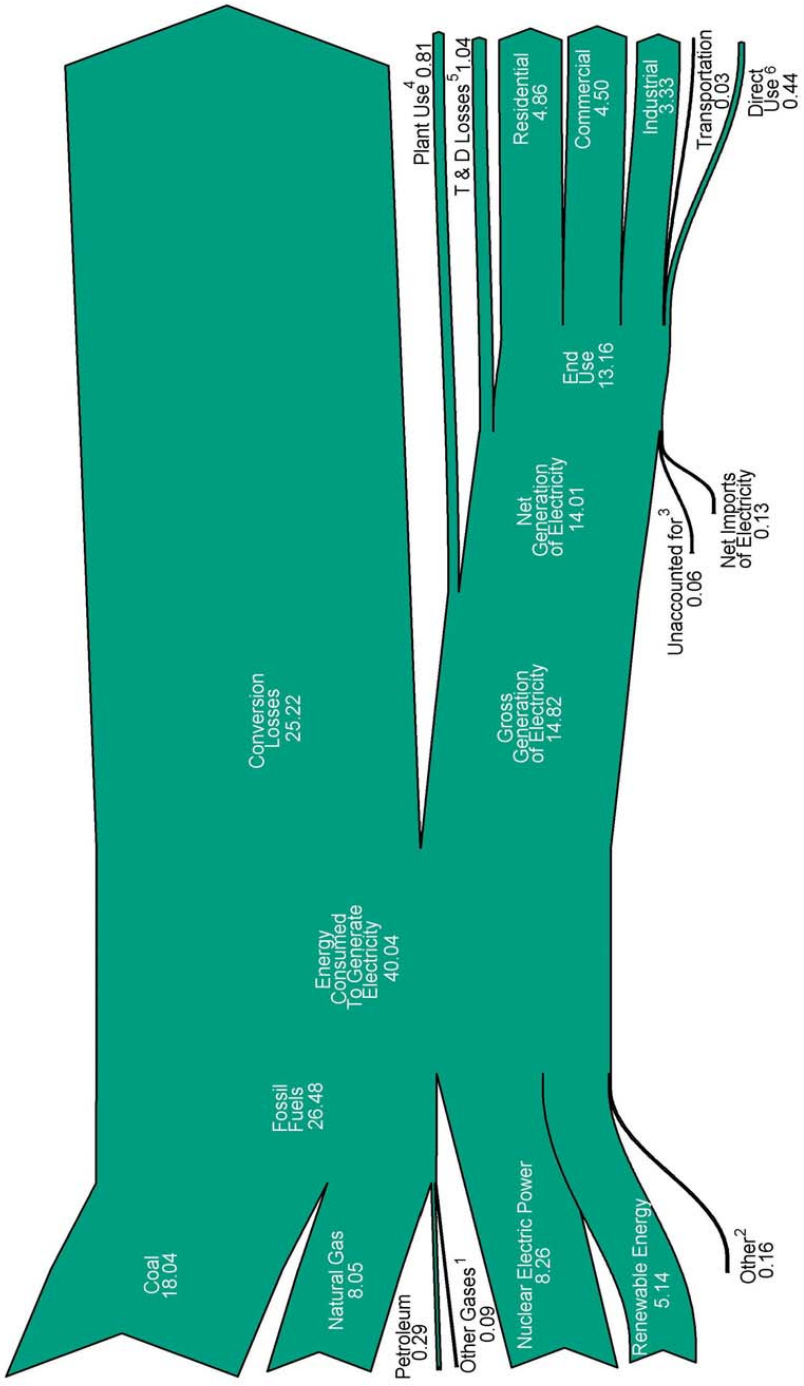

Figure 1.4: Sources and sinks in domestic electrical energy generation industry in quadrillion BTUs. Note that dividing gross energy generated (14.82 quadrillion BTU) by total energy consumed to generate energy (40.04 quadrillion BTU) yields a quotient of 0.37. This means that the efficiency of electrical energy generation in the US is roughly 37% nationwide. Source: DOE

1.1.2 Dye Sensitized Solar Cells (DSSC)

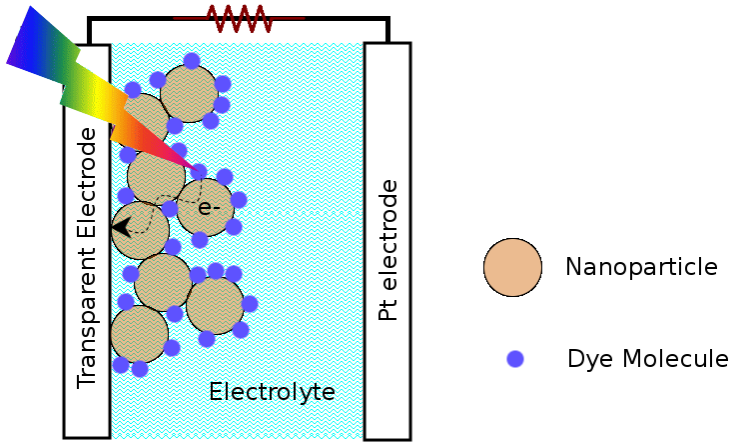

Figure 1.5: The schematic representation of a dye-sensitized solar cell. Initially a photon excites the dye molecule attached to a nanoparticle into a high-energy state. This state then injects an electron into the nanoparticle's bulk, where the electron is able to drift through the nanoparticle network to the transparent electrode. The transparent electrode conducts the electron to an external circuit, where it is able to power a load, after which the electron returns to the cell via the platinum electrode. The platinum electrode transfers the electron to the electrolyte, which then reduces the dye molecule that was originally oxidized by the electron transfer event.

The dye-sensitized solar cell has long been touted as a solution to the solar energy problem. In this type of solar cell, a semiconducting nanocrystal has a dye molecule chemically attached to it (see Figures 1.5 and 1.6). The semiconductor nanocrystal, whose high band gap (usually greater than 3 eV) makes it unresponsive to visible light, needs the dye molecule in order to utilize the sun's natural spectrum (which has the highest photon flux in the region below 3 eV).[6] Originally the DSSC was designed with dye molecules sensitizing large, single-crystalline semiconducting materials, but this design suffered from a lack of surface area onto which the dye molecules could coordinate, limiting the amount of incident light that could be absorbed by the device.[7] In 1991, O'Regan and Grätzel showed that mesoporous, nanocrystalline anatase TiO_2 could be sensitized by a ruthenium dye.[8] The nanocrystalline morphology allowed

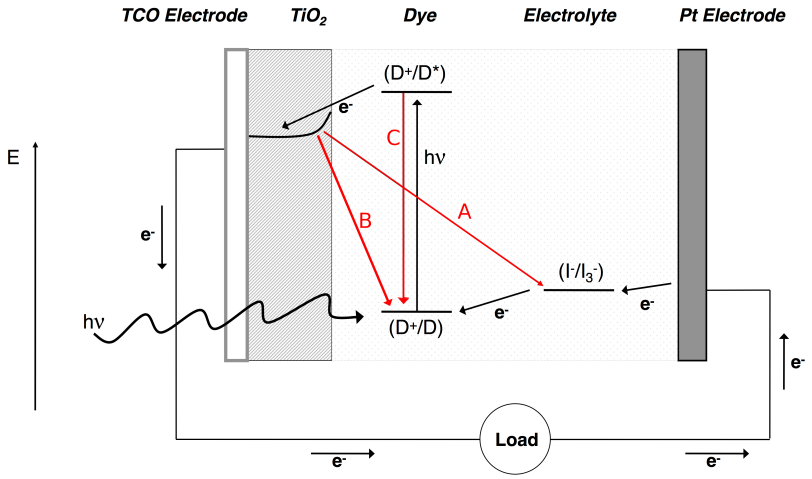

Figure 1.6: Diagram representing energy levels of various components of the DSSC. Red arrows (processes A, B and C) indicate loss mechanisms, and black arrows represent proper function of DSSC assemblies. Process A corresponds to e_{CB} interception by the electrolyte. Process B corresponds to a recombination reaction regenerating ground state dye. Process C corresponds to radiative relaxation of the dye's excited state back to the ground state.

enough dye molecules to interact with the incident light that more than 80% of the photons incident upon the device ($\lambda = 520$ nm) were converted to electrical current.[8]

In the DSSC, the excited state of the dye molecule resides at a higher oxidation potential than the conduction band of the semiconductor nanocrystal. Upon excitation of the ground state of the dye, the small energetic difference between the now-occupied LUMO of the dye and the conduction band of the semiconductor facilitates fast injection of the excited electron into the conduction band (Figure 1.5 and 1.6). The lower energy of the conduction band also provides a small enthalpic driving force for the charge separation. Two processes subsequently compete to determine where the injected electron will end up. The first is a recombination of the conduction band electron (e_{CB}) with the redox couple electrolyte, most commonly iodide/triiodide (process A in Figure 1.6). This process, which will reduce the efficiency of the cell, occurs because of the large amount of the nanoparticle's surface area that is exposed to the electrolyte solvent.

The second process is current flow into the external circuit through the SnO_2:F transparent conducting oxide (TCO, or "transparent electrode" in Figure 1.5) layer. It is this current that can be utilized for applying work to an external load. The voltage that this current is able to sustain is equal to the difference between the Fermi level (E_f) and the redox potential of the iodide/triiodide redox couple.[6] Steps necessary to keep current flowing under incident light exposure, namely ground state dye regeneration, redox couple regeneration, and diffusional transport are also involved, but not shown.

Upon this framework of sensitization of a semiconductor nanocrystal by a dye molecule, many deviations have been reported. Research into these variations has the goal of either increasing efficiency or extending the lifetime of DSSC devices.

Electrolyte and Redox Couples

The components of the electrolyte have been varied, mainly to reduce volatility, but also with the goal of reducing the amount of wasted voltage that can be extracted from a particular cell. Ferrocene/ferrocenium couples have been investigated, but their fast redox kinetics render any cells containing them useless — they are able to recombine with e_{CB} quickly, effectively short-circuiting any photocurrent.[9,10] Blue copper complexes (copper chlorophyllin) have also been investigated, but have similarly failed to gain a foothold in the DSSC research community.[11] It appears that the slow reduction of the iodide/triiodide significantly contributes to the high efficiency of the DSSC — any I_3^- in contact with the surface of the nanoparticle or SnO_2:F electrode has the potential to interrupt the current flow,[9] but the small rate constant of this reaction with respect to the rate of electron flow means that it is not a competitive process. Thus reduction of the I_3^- by e_{CB} does not substantially reduce the efficiency of the cell.[9,12,13] Similar arguments can be made for the Br^-/Br_3^- couple, which is used for cells containing dyes at a higher excited state potential than the common bipyridine ruthenium dyes.[9] The result of all these investigations into the electrolyte and redox couple is that the iodide/triiodide couple is still used, but it is frequently introduced into the cell as part of an ionic liquid.[14–16] This reduces the volatility of the cell's components, which would have otherwise reduced the lifetime of a DSSC device, without substantially hindering charge diffusion through the cell.[17,18]

Research on other electrolytes continues, and is brought about because of large

losses in V_{OC} from the iodide/triiodide redox couple ($\sim$500 mV in combination with N3 as a sensitizer).[19] Use of other electrolytes with faster electron transfer rates (and therefore larger possibilities for recombination losses) are predicated on blocking ingress of electrolyte to the surface of the nanoparticle or the SnO_2:F electrode.[20–26] Dye molecules have had large, bulky, aliphatic groups appended to them to achieve this goal, making some of the previously discarded electrolytes newly relevant.[21,23–26] The most efficient cells at this time are taking advantage of a cobalt (II/III) redox couple, which increases the possible V_{OC}.[27]

Sensitizers: "Dye Molecules"

The first attempts to sensitize large-gap semiconductors with a colored "dye" molecule failed due to the short excited state lifetime of the rhodamine B dye used.[28] O'Regan and Grätzel came up with a novel ruthenium complex that functioned as an antenna to transfer energy from the extrema of the dye molecule into the semiconductor, via a carboxylate linkage to the surface.[7,8] The intramolecular energy transfer step led to this complex (shown in Figure 1.7) having much longer excited state lifetimes, improving injection efficiencies. The intersystem-crossing event also contributed to a longer excited-state lifetime by making the radiative dissipation of the excited state's energy slower (because the $T_1 \longrightarrow S_0$ process is formally forbidden).

As a result, the majority of currently-used sensitizing dyes in the DSSC are still bipyridine or terpyridine ruthenium complexes. Their long excited state lifetimes and rapid charge injections into TiO_2 mean that they favor processes that augment the performance of DSSCs. In the case of the N719 ruthenium bipyridine dye, experiments demonstrate that the steric bulk can actually act as a blocking layer to impede recombination of CB electrons with iodide/triiodide species, which serves to show that intelligent dye design can also overcome some of the other problems with the DSSC ensemble.[29–32] In addition to blocking e_{CB} recombination with electrolyte, rational dye design has also been focused on improving the incident photon to current efficiency (IPCE – equation 1.1).

$$\mathrm{IPCE}(\lambda) = \mathrm{LHE}(\lambda) \times \phi_{\mathrm{inj}} \times \eta_{\mathrm{e}} \tag{1.1}$$

Equation 1.1 shows several components that can be optimized to increase the IPCE

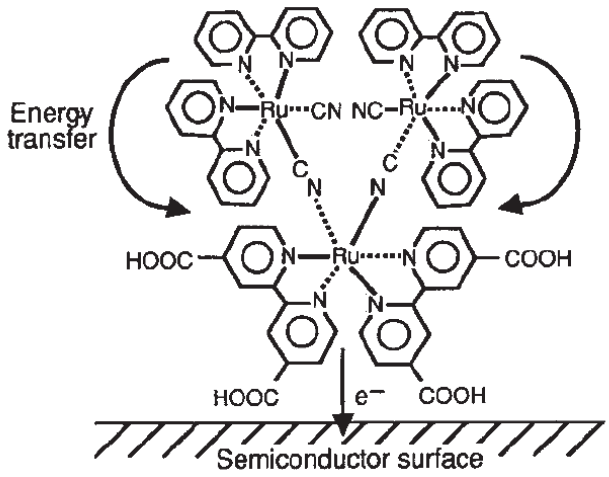

Figure 1.7: The bipyridine ruthenium dye from O'Regan and Grätzel's 1991 Nature paper.[7] This dye's structure is such that after oxidation, the cationic portion of the dye will be separated from the semiconductor surface. This has the effect of reducing recombination of e_{CB} with the oxidized dye.

of a device. The main area for improvement is the light harvesting efficiency (LHE), which is dependent on the sensitivity of a dye molecule to the lower ranges of wavelength in the solar spectrum.[19] This is fertile ground for research because the electron injection efficiency, ϕ_{inj}, and the current collection efficiency, η_e, are already optimized. To increase LHE, dyes have been synthesized that are able to absorb the energy from longer wavelengths, which allow current densities in the area of 15-20 mA/cm^2.[33–36] However, more needs to be done since there is still $\sim$20% (by energy) of the solar spectrum that cannot be absorbed by even "Black Dye" (Figure 1.8).[35]

Further advances in the areas of dye-semiconductor interactions have allowed the durability of DSSCs to skyrocket, with the goal of negligible performance decrease after 1000 hours at 60°C in incident sunlight already achieved.[33,37] Note, however, that even with these gains, DSSCs still lag behind silicon p-n junction solar cells in terms of reliability and durability.

In spite of the advanced and seemingly mature state of the dye technology, research continues because of several reasons, including reactions of the dye with the corrosive iodide/triiodide redox couple and aims to replace the redox couple with a solid state

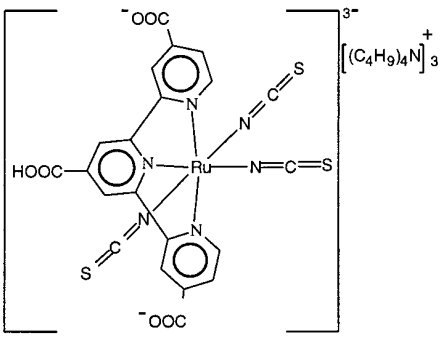

Figure 1.8: "Black Dye" from Nazeeruddin's 2001 Paper [35]

system, which will relieve many of the electrolyte/redox couple's problems.[38–41] These dyes frequently possess conductive portions, which will ostensibly allow for coupling to a polymeric, solid electrolyte, thus bridging the gap between the purely organic solar cells and the Grätzel-type cell.[10,40,41] Also, the relatively low natural abundance of ruthenium in the earth's crust counterindicates widespread use of these types of dyes.

Purely organic dyes avoid these scarcity issues, and have been a subject of investigation for many years.[28] Terthiophenes,[42,43] coumarins,[44] and bodipy-type molecules [45] are especially popular since they have been subjected to scrutiny in other fields. It is possible that a cosensitized-type cell will ultimately be the most efficient — the reasoning being that a cell with a semiconductor nanocrystal being sensitized with two different dye molecules may be able to span the solar spectrum to the greatest extent. However, attempts to achieve this cosensitization rarely exceed the efficiency of the most efficient dye alone.[46] It is thought that this is due to the fact that the dyes compete for space on the semiconductor nanocrystal and thus are limited by a smaller number of dyes absorbing, and thus by their extinction coefficient.[46] This is supported by the fact that generally cosensitized cells reach an efficiency which is lower than a cell made from the higher efficiency dye alone.[46] A notable exception is the current record-holder DSSC, which uses cosensitization based on a porphyrin dye along with an organic triphenyl amino dye.[27]

While not mentioned above, binding mode diversity in an adsorbate's attachment to nanoparticle surfaces, and its effects on electron transfer is also important, but difficult

to ascertain. Young, *et al.* have reported that oleic acid adsorbed onto the surface of nc-CdS will adopt a chelating bidentate binding mode,[47] but other authors have suggested that an ester-type linkage is responsible for most of the attachments of dyes to nanoparticles in the DSSC arena.[48,49]

Sensitizers: "Dye Particles"

Sensitizers need not be organic nor precious metal complex-containing dye molecules. Smaller-band gap semiconductor nanoparticles can also perform the task of absorbing light and injecting electrons into a substrate. Many researchers have tried and succeeded in sensitizing wide-band gap semiconductor nanocrystals such as TiO_2 with semiconductor nanocrystals possessing smaller band gaps, such as CdSe, CdTe, PbS, and CdS.[50–59] The main idea is that one can take advantage of the well-known quantum confinement properties of various photostable semiconductor nanocrystals[60–62] and make a dye out of an easily-manipulated nanoparticulate system.[51–54,56,58,63] Avoiding interferences to charge transport across the interface between the two semiconductor surfaces is of paramount importance, thus coupling the two semiconductors together needs to be done carefully.

The most popular coupling mechanism is a bifunctional molecule with a mercapto group on one end and a carboxylic acid group on the other. This type of molecule preferentially binds oxide nanoparticles at the carboxylate functionality and sulfides at the mercapto group. Thioglycolic acid, 3-mercaptopropionic acid, mercaptosuccinic acid, and cysteine are all among the bifunctional molecules that have been studied to this point.[51,56,58,64–66]

Another way to couple the two semiconductors together is to deposit the lower band gap material onto the higher one using a solution-based deposition, such as successive ionic layer adsorption and reaction (SILAR), electrodeposition or chemical bath deposition. While these ensure a more intimate contact between the two semiconductors, it is difficult to control the size and morphology of the deposited phase, and frequently inhomogeneities arise in the deposition thickness.[50,59,67–69] Furthermore, rods or premade films are often needed for this type of arrangement because the higher band gap semiconductor needs to have at least one side of the crystal exposed to the external circuit. Growing rods on the surface of TCOs is then a logical way to avoid completely

encapsulating the higher band gap semiconductor.[51,70,71] Additional benefits from having a core-shell rod arrangement of sensitizing semiconductor-substrate semiconductor may also exist, such as a larger contact area for the junction and certain charge separation benefits (Figure 1.9).[67]

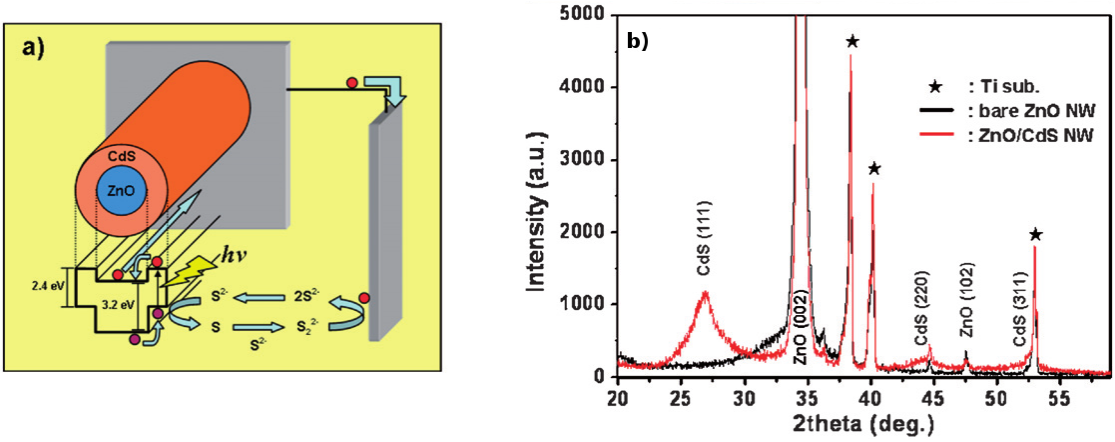

Figure 1.9: (a) Image from Tak 2009 showing a schematic of a CdS-coated ZnO nanorod and the physical processes that are expected to occur to extract energy from a photon. (b) Shows that Tak, et al. have successfully deposited CdS onto ZnO [67]

The last common way to adhere the sensitizing nanocrystal to the sensitizer nanocrystal is physisorption, which takes advantage of the fact that certain nanocrystals such as InP and InAs will naturally adsorb to the surface of large band gap semiconductor nanocrystals.[72–74] These attempts to transfer electrons from the CB of InP or InAs to TiO_2 generally proceed via surface states, but in spite of the intimate contact made via physisorption, electron injection is not efficient.[73,74] As with deposition methods, it is similarly difficult to control the morphology of the sensitizing semiconductor, and this may well play a role in the lower photocurrents.[74,75]

The dye moiety, whether it is a nanoparticle or molecular dye, is the workhorse of any DSSC and therefore needs to be subjected to the most intense scrutiny regarding its reliability, durability and efficacy.

Nanocrystalline Films (Photoanode)

Most DSSCs today use the anatase form of TiO_2 because of its well-known behaviors and properties.[8,76,77] It appears that anatase benefits from a faster reduction reaction with the iodide/triiodide couple than the oxidation reaction. That is to say that anatase will more readily donate a hole to the redox couple than an electron. Furthermore, electron addition to TiO_2 via application of a bias voltage to a potential more negative than the CB drastically increases the conductivity and turns the TiO_2 from transparent to a deep blue.[78] It was previously thought that these effects allowed the anatase nanocrystals to build up a negative space charge, thus creating a gradient which serves to push the CB electrons through to the TCO SnO_2:F layer (the photoanodic contact). The photogenerated gradient therefore was thought to be technically different from a silicon p-n junction-type Schottky barrier, but serving a very similar purpose.[79] Although it was known for decades that small particles may not be able to sustain internal fields,[80] Kronik et al. went on to demonstrate that such fields can exist inside a film composed of semiconductor (CdSe, in that case) nanocrystals, and these fields can indeed induce drift currents. However, in the same study, Kronik et al. conclude that in the case of a photovoltaic cell immersed in an electrolyte, the external surroundings strongly dictate the ability of a particle to sustain a field.[81] Specifically, interaction with the electrolyte will cause a thorough depletion of the particle because mobile ions in the electrolyte will quickly and effectively neutralize any charge buildup.[6,82,83]

Thus charge separation must occur in some other way. In fact, it has been exhaustively detailed that a Helmholtz layer can be found on the surface of the photoanodic TiO_2 nanocrystalline surface.[6,12,83] This electrical potential drop helps separate the charges, and also reduces the possibility of recombination. Additionally, the fact that the density of states inside the nanoparticle is greater than that of the dye molecule contributes to a small entropic force driving the charge injection.[6]

While the nanocrystal material is generally ZnO, SnO_2 or TiO_2, many attempts have been undertaken to modify these nanocrystals to squeeze a small amount of efficiency out. One advance that increases the photocurrent quite unexpectedly is a UV treatment of the cell as a whole. Provided that the cell contains 4-*tert*-butylpyridine, the overall cell efficiency skyrockets. The explanation of this phenomenon is that the UV radiation causes the conduction band of the nanocrystalline TiO_2 to shift more positive and

therefore electron injection is has more of an energetic driving force.[84] A very similar effect was achieved by controlling the types of cations at the interface of the semiconductor nanocrystal and the electrolyte. In this particular case, lithium was proposed to have stabilized TiO_2 acceptor states which made electron transfer more energetically favorable.[85] Molecular dipoles have been used to shift the levels of conduction bands as well. For example, Shalom et al. discovered that depending on the direction of the dipole with respect to the surface, the energy levels of a nanocrystal could shift either up or down.[69] This effect was limited to about 20 mV/Debye. Chenodeoxycholic acid is also widely used to adjust the energy levels of the TiO_2 nanocrystal upwards to increase the photovoltage. It is thought that it also reduces the rate of recombination by blocking the surface from the electrolyte, but evidence shows that it may only serve to remove weakly bound dye molecules that were in a coordination position that was not conducive to electron injection.[86,87] Lastly, 4-*tert*-butylpyridine and ammonia both have also been used to adjust the energy levels of the semiconductor nanocrystals, and both serve to increase the V_{oc} at a given current density.[12] This is thought to be caused by a deprotonation of the surface by the nitrogen group and a subsequent negative charging of the surface.[12,87] The magnitude of this effect is much larger than that of Shalom *et al.* — this effect of pyridine derivatives and basic nitrogens can span almost 200 mV.[13]

The movement of charge carriers (electrons) through the photoanode has become something of a curiosity because generally wide-gap semiconductors like TiO_2 are not very good conductors. However, Brus addressed carrier conduction through semiconducting porous silicon nanocrystals in polar solvents and in vacuum, with the conclusion that the electron-polar solvent dynamic coupling will cause the porous silicon to conduct rapidly and without activation energy.[88] Although this study was a theoretical one using some rather gross approximations, it matched up well with experiments. de Jongh and Vanmaekelbergh's study gives further credence to Brus' assertions by showing that the rate of trapping and detrapping of the photogenerated carriers in interfacial band gap states is controlled by steady-state light intensity and interfacial kinetics.[89] These studies are also corroborated in other carrier-transport analyses on similar materials, as it is shown that trap states are likely the basis of transport, supporting Brus' assertions that the polar environment surrounding a small semiconductor crystal could effectively

stabilize surface charges.[89–91] In fact, according to Boschloo et al. these surface states could rest as far as 0.4 eV below the conduction band edge.[91]

The motion of charge carriers through the photoanodic TiO_2 film can be viewed as involving an intimate couple of the semiconductor nanocrystal and the electrolyte, where carrier transport may be better described as solvent rearrangement at the surface of the semiconductor nanocrystal.[6,83] Cahen et al. likens this type of motion to a small polaron with stabilization energy of ∼0.5 eV to compensate for the charging energy — thus at every step of carrier transport, a particle participating will be electrically neutral.[6,88] Importantly, this means that no additional impetus is required to convey the electron into the electrode contact, which is seen as roughly degenerate, and therefore no energy input is needed to achieve injection into the SnO_2:F.[6] The most salient outcome of this analysis — that transport of electrons is of a diffusional character rather than a drift-based one — is in agreement with the majority of other studies, although some still suggest a larger role of the conduction band in that diffusional transport.[82,83,92]

1.1.3 Energy Conversion

Since the main components have now been reviewed, a synergistic view of the cell is warranted. Figure 1.6 shows a detailed picture of what the source of power is in the DSSC, as well as where the various inefficiencies come from. Two sources of shunt currents can be seen, the recombination of the electron on the particle with the ground state dye (process B, Figure 1.6), and the radiative relaxation of the excited state back down to the ground state (process C, Figure 1.6). The ruthenium dyes have almost completely obviated the radiative relaxation problem because of their very long excited state lifetime and their ultrafast charge injection times.[37] The recombination of electrons in the nanocrystal and the ground state dye is also relatively slow and non-competitive for the ruthenium dyes.

Being able to minimize the shunt currents, and maximize the photocurrent at which the DSSC can sustain useful amounts of photovoltage is critical to making the DSSC as efficient as possible. The various recombinations contribute to dark currents, which will substantially lower both the short-circuit current, I_{sc}, and the maximum power current, I_{mp}.[76,93] The maximum power current is reflected in the fill factor, which is the ratio

defined in equation 1.2 where variables are as above, V_{OC} is the open circuit voltage and V_{mp} is the voltage produced at maximum power.

$$\text{Fill Factor (FF)} = \frac{I_{mp}V_{mp}}{I_{sc}V_{OC}} \tag{1.2}$$

$$\text{Efficiency} = I_{sc} \times V_{OC} \times \text{FF} \tag{1.3}$$

Since the fill factor is related to the overall efficiency by equation 1.3, increasing the fill factor is quite important as well.

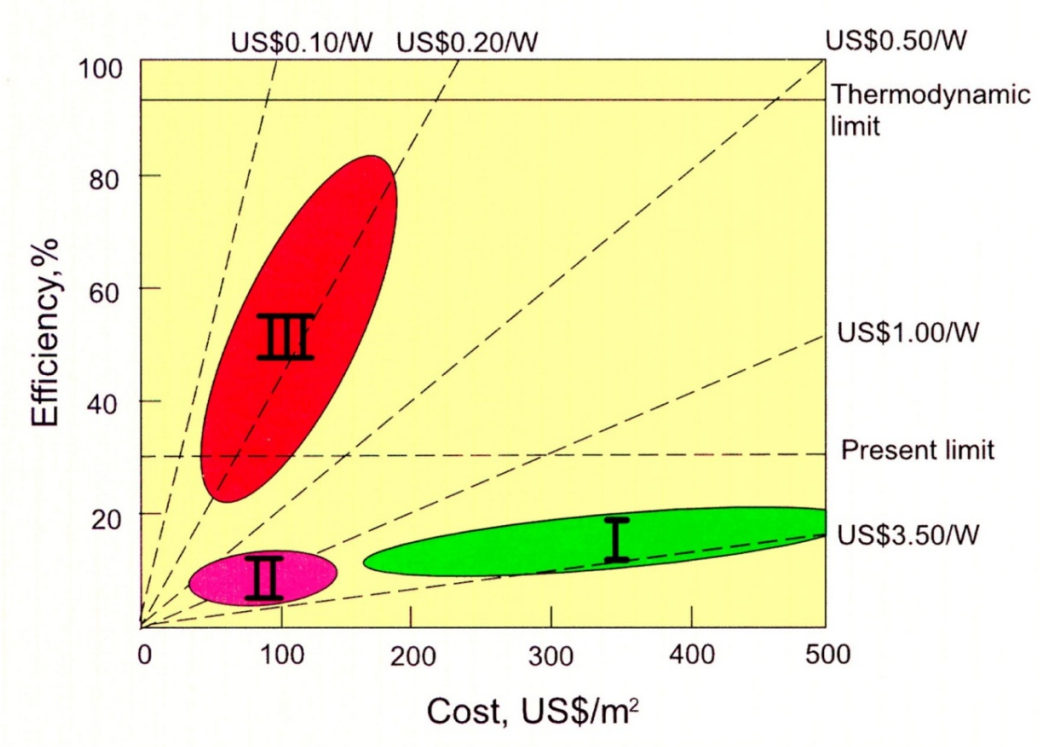

Figure 1.10: The Various Generations of Solar Cells to Date [1]

In order to increase the efficiency of a typical DSSC to a point where they are economically viable (figure 1.10, [1]), we need to pay close attention to how the inefficiency comes about. Many attempts at isolating variables have been successful in increasing efficiencies previously. For example, the careful study of the TiO_2's charge carrier conductivity showed that alternating the various surface potentials could increase or

decrease the photocurrent controllably, and without substantially impacting the photovoltage.[12,13,87]

Eliminating variables like those involved in the film structure, electrolyte dynamics, and diffusional characteristics are key to understanding the most salient aspects of the photovoltaic cell. Being able to identify positively a dye-nanoparticle dyad (the method of attachment of this dyad will be discussed shortly) and characterize it with various analytical techniques is of fundamental importance in our studies of electron transfer.[94] Thus we wish to explore ways to use monodisperse semiconductor nanocrystals as templates upon which dyes can be attached and the photoluminescence (PL) can be monitored in the dispersion state.[94]

1.2 Dispersion Phase Quenching Studies

In order to achieve a successful study of excited state electron transfer from a dye molecule into a nanocrystal, a well-defined system is needed which will allow the use of multiple measurement techniques to measure multiple properties of such a system. Cadmium sulfide nanocrystals, as first synthesized by Yu and Peng,[95] seem to be that well-defined system. Cadmium sulfide is known as a material that can be highly toxic due to the presence of Cd^{2+} ion, and thus it is less attractive as a component in consumer solar products. However, it can be synthesized into highly monodisperse nanocrystals, and that monodispersity can be seen quite clearly by the UV-Vis spectra from the Yu-Peng synthesis (Figure 1.11).[95] In fact, the Yu-Peng synthesis of CdS nanocrystals is so versatile that the size and distribution of the resultant nanocrystals can be easily changed by modifying simple reaction conditions such as concentration of the capping surfactant and reaction time.[95] Due to these benefits, coupled with the fact that our research is focused on basic science rather than near-term consumer products, we focus a large portion of our attention on developing this CdS model system for dispersion phase quenching studies.

More than any other property, the monodispersity of highly-stable oleic acid-capped CdS nanocrystals is of paramount importance. Fundamentally, a monodisperse sample of nanocrystals can be assumed to have the most similar surface chemistry, bulk geometry, crystallographic phase, and electronic properties that can be observed in an

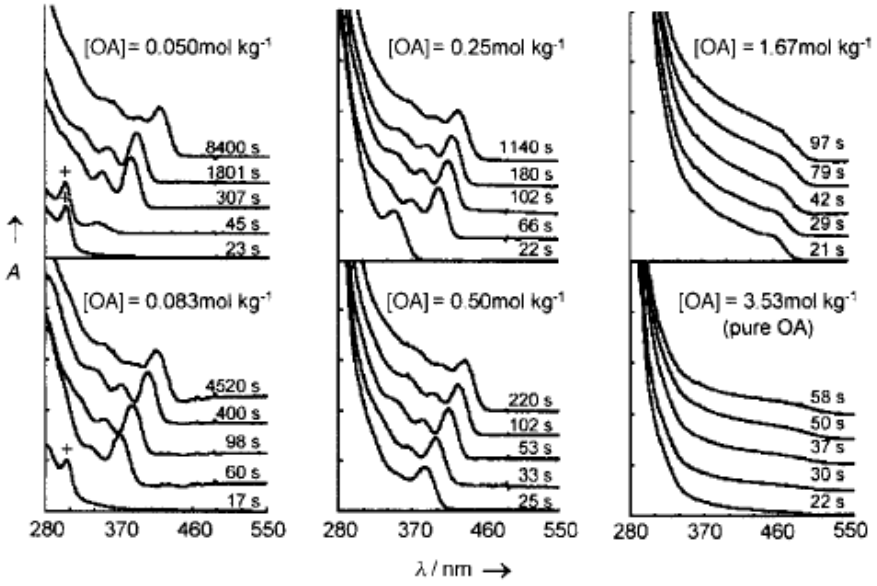

Figure 1.11: UV-Vis spectra of six different reaction mixtures with different [OA] are shown at different times. Magic sized clusters are marked with a (+) [95]

ensemble of kinetically trapped objects. Previously, nearly monodisperse particles of cadmium chalcogenides were synthesized using a highly reactive cadmium precursor, $Cd(CH_3)_2$, and the synthesis was very difficult to perform.[96] The instant nucleation of the organo-cadmium procedure gave the ability to separate the nucleation and growth steps, and thus some control over size distribution, but the Yu-Peng synthesis also does that without highly pyrophoric reactants and without requiring many practice trials. The Yu-Peng monodispersity is thought to come from the slow rate of nucleation, growth, and defocusing that the controlled concentration of $Cd(oleate)_2$ allows. This effect can be seen as due to the variable reactivity of the $Cd(oleate)_2$ monomer at varying concentrations of oleic acid. Evidence that the variability of the monomer reactivity comes from the varying concentration of the monomer can be found in figure 1.12, where it is shown that a lower concentration of oleic acid will consume Cd^{2+} more rapidly than the higher concentrations.[95]

This effect seems to be related to the nucleation of the nanocrystals, which is also influenced by the stability of the monomer,[97] but clearly in Figure 1.11 there is some

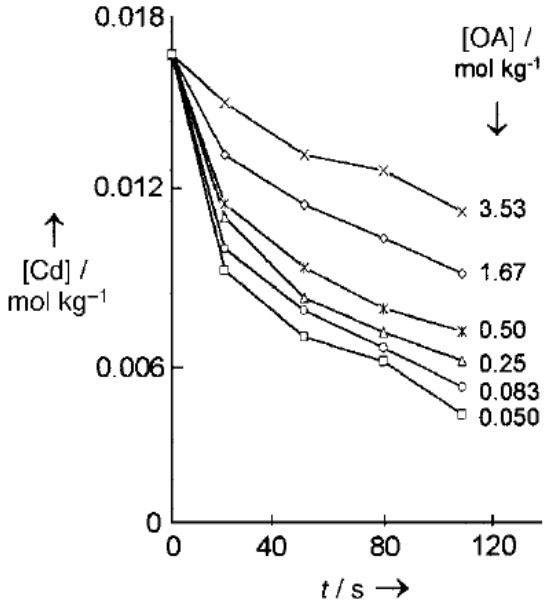

Figure 1.12: Monomer reactivity is apparently dependent on the concentration of monomer – a lower concentration of oleic acid ([OA]) leads to a faster depletion of Cd^{2+} ([Cd]) in the reaction mixture [95]

growth as well. This growth will undoubtedly ripen and defocus a narrow size distribution. This growth is related to the specific surface energy of the nanocrystalline object as described by the Gibbs-Thomson equation (Equation 1.4)

$$S_r = S_b \exp(2\sigma V_m / rRT) \tag{1.4}$$

where S_r and S_b are the solubility of the nanocrystal and of the bulk solid, σ is specific surface energy, r is the radius of the nanocrystal, V_m is the molar volume, R is the Universal Gas Constant, and T is the temperature.[98] Impeding this growth allows the recovery of highly monodispersed nanocrystals. In order to accomplish this, one can reduce the surface energy by capping with surfactants, a very common strategy that has precedent in many different types of semiconductor and conducting nano-objects.[99–101] Upon capping with a functional group capable of donating electrons to a electrophilic surface cation, it is thought that the cations' surface energy is reduced. Heteronucleus crossed-polarization NMR has shown in the case of CdSe nanocrystals

capped by hexadecylamine (HDA) that the HDA's protons strongly interact with cadmium (^{113}Cd, an NMR active nuclide), which appears to confirm the HDA's attachment to the cadmium on the CdSe nanocrystal surface.[102] We also find evidence for binding of capping ligands to Cd sites on the surface of CdS, and this evidence is presented later in this thesis. These surfactant molecules possess an alkyl tail that allows for the creation of an organic phase dispersion.

1.2.1 Surface Characterization of Nanocrystals

Since our research utilizes dyes such as the terthiophene and ruthenium coordination complex dyes containing carboxylate anchoring functional groups, an in-depth understanding of these functional groups with the surface is needed. Study of surface binding properties of carboxylate groups onto II-VI semiconductor nanocrystal surfaces can be carried out using FTIR. Because there exists a significant amount of oleate coordinated to the surface of the as-synthesized nanoparticles,[95] the IR signal from this surface-binding mode is large, and we will start our description of the surface by analyzing data from IR studies.

In studying the CdS particles, synthesized via the Yu-Peng synthesis, Young *et al.* have shown that the attachment of the oleate's carboxylate to the surface is by a bidentate chelate.[47] This can be seen from the fact that the difference, Δ (Equation 1.5), between the symmetric and antisymmetric stretches of the carboxylate group is less where the molecule is attached to the surface than in the case of the solution-phase deprotonated version of the molecule.

$$\Delta = \nu_{assym} - \nu_{symm} \tag{1.5}$$

Furthermore, Young *et al.* show that in their CdS nanocrystals which are drop cast from a dispersion of toluene, they find methylene vibrations characteristic of a close-packed monolayer.[47] This is seen in Figure 1.13 where the oleic acid's antisymmetric and symmetric stretches lie at 2922 cm^{-1} and 2853 cm^{-1}, respectively, which is characteristic of a disordered arrangement. However on the drop cast film of oleate-capped CdS nanocrystals, these vibrations decrease to 2917 cm^{-1} and 2850 cm^{-1}, respectively.[47]

The kinetics of the attachment of oleic acid and oleate species to II-VI surfaces has also been studied extensively.[103] It has been found that equilibrium of sodium

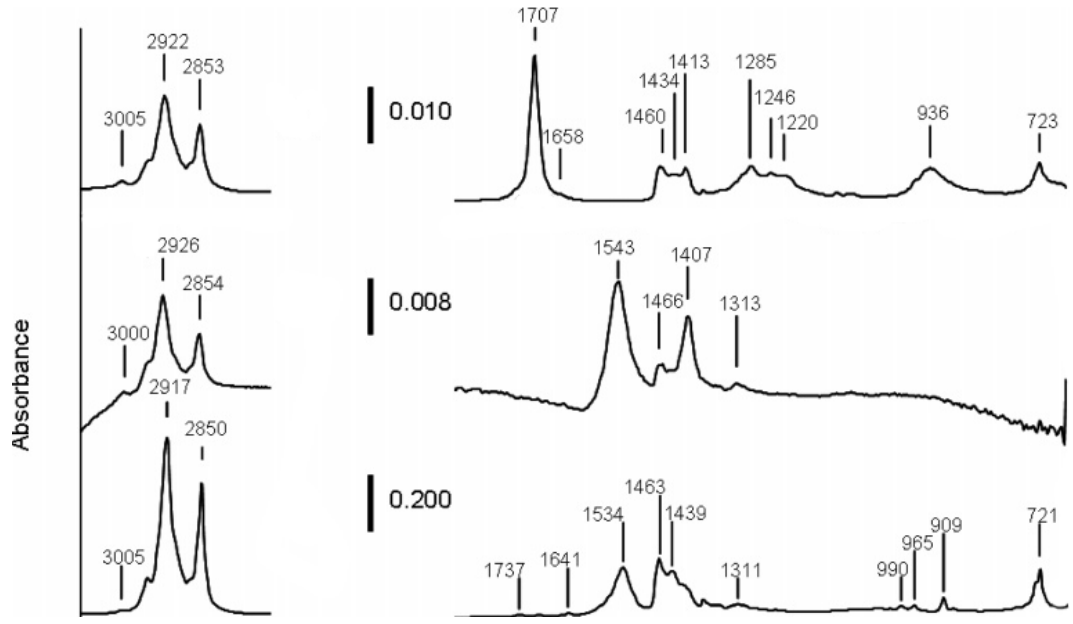

Figure 1.13: FTIR-ATR of oleic acid, neat (top); sodium oleate in water (middle); and dry film of oleate-capped, Yu-Peng CdS nanocrystals (bottom), from Young *et al.* [47]

oleate adsorption onto apatite surfaces occurred within 1-2 hours. These oleate-coated apatite surfaces showed that the methylene groups of the oleate exist in a disordered state, as evidenced by their asymmetric stretching vibration ($\sim$2920 cm^{-1}, spectrum not shown).[103] Mielczarski *et al.* also provides us with more evidence pertaining to the Young *et al.* analysis that the carboxylates are chelating bidentate because Young *et al.* never actually recorded an IR spectrum of the correct metal salt of oleate to compare according to equation 1.5. In order for the Young *et al.* analysis to be valid, they needed to compare the adsorbed oleate to *cadmium* oleate, not sodium oleate, since the surface of attachment contained cadmium and not sodium. However, Mielczarski *et al.* have showed that the Δ for cadmium oleate is similarly larger than that for the adsorbed species (Figure 1.14), and thus the attachment is indeed chelating bidentate.[103]

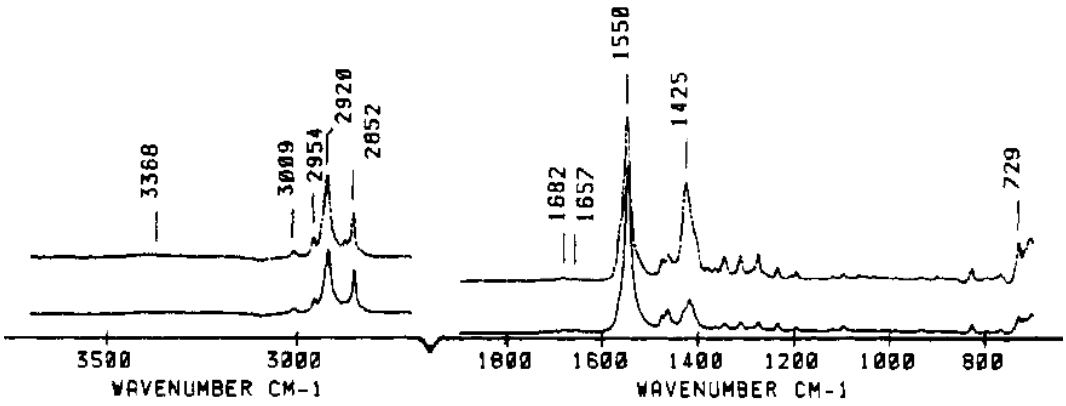

Figure 1.14: FTIR-ATR of cadmium oleate precipitated at pH of 5.2 at p-polarization (top) and s-polarization (bottom) [103]

1.2.2 Characterization of the Bulk Morphology of CdS Nanocrystals

A major reason for our use of cadmium chalcogenide nanoparticles in quenching studies can be found in Yu, *et al.* where the empirical correlation between the first exciton absorbance peak (γ, in nanometers) and the nanoparticle diameter (also in nanometers) is given (Equation 1.6 and Figure 1.15, left).[104]

$$\mathsf{CdS}\text{: } D = (-6.6521 \times 10^{-8})\gamma^3 + (1.9557 \times 10^{-4})\gamma^2 - (9.2352 \times 10^{-2})\gamma + 13.29 \quad (1.6)$$

This is crucially important to be able to find the diameter of the particles without being forced to use TEM. Past this, the same study detailed the extinction coefficient of the nanoparticles, giving us the ability to find the concentration of the particles in a dispersed phase simply by recording a UV-Vis. Yu *et al.* utilized atomic absorption in this case to study the concentration of Cd^{2+} in a monodispersed sample and create this empirical fit (equation 1.7 and figure 1.15, right).[104]

$$\mathsf{CdS}\text{:}\epsilon = 5500\Delta E(D)^{2.5} \quad (1.7)$$

Yu *et al.* continues, detailing corrections for cases in which the breadth of the first absorbance peak is much broader than that for which Equation 1.6 was fit. Using the breadth of the [symmetric] photoluminescence peak, the absorbance can be scaled up accordingly, but Wang *et al.* point out that the bulk emission from the Yu-Peng particle

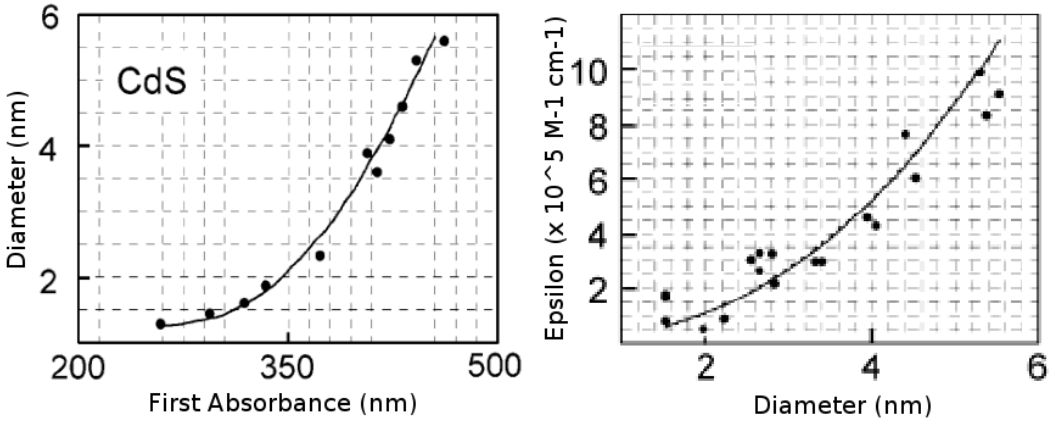

Figure 1.15: Fit of equation 1.6 to actual data from Yu *et al.* 2003, showing the close fit of the size-to-first absorption peak and the epsilon-to-size data [104]

is strongly dependent on the time that the particles have been exposed to oxygenated solvents[105] so this approach may not be as robust as the others.

Using Equations 1.6 and 1.7, one is able to easily quantify and characterize the particles in a dispersion of CdS nanocrystals. Therefore, it is possible to create a "stock solution" of nanocrystals and accurately know both the average size of the particles in the dispersion and the concentration. This is especially helpful when a certain molar ratio of dye to nanoparticle is needed, as is the case in many of the subsequent investigations outlined in this thesis.

The first exciton's dependence on size speaks to an interesting trend pertaining to the CdS nanocrystals. It is clear from Equation 1.8 that when the first exciton's absorption wavelength changes, so too does the band gap.

$$\mathsf{E} = h\nu = \frac{hc}{\lambda} \tag{1.8}$$

Thus the smaller wavelength required for excitation of a small particle means that the conduction band has shifted to a higher energy in response to the quantum confinement that is often seen in particles which are smaller than the Bohr radius of an exciton in that bulk material.[99] Since the bulk band gap for CdS is 2.45 eV, corresponding to roughly a 500 nm photon absorption, a 375 nm absorbance peak (a 2.65 nm diameter particle according to Equation 1.6) means that the band gap has expanded to 3.30 eV. This

amount of quantum confinement is much larger than some other II-VI semiconductor nanocrystals, such as ZnO. In the case of ZnO, a 2.65 nm nanocrystal will only have about 0.5 eV band gap increase.[106] This means that exploration of the quantum size effects will be substantially more sensitive in CdS than ZnO.

1.3 Outline of This Thesis

This thesis details studies that focus on the DSSC, as described above, primarily from an experimental approach, but also with important contributions made possible by computational chemistry techniques developed elsewhere. This thesis is composed of:

- Chapter 1 (this introduction).
- Chapter 2 describes the first experiment in which charge transfer from a dye molecule to a CdS nanoparticle was demonstrated using ultrafast transient absorption methods. This chapter introduces and further develops the topics of NMR-based determination of attachment of dye molecules to nanoparticles, surface-templated aggregation-induced energy loss, and analytical methods by which this aggregation event can be ascertained.
- Chapter 3 develops the previous chapter's ideas of aggregation-induced energy-loss mechanisms and applies them to a broader spectrum of materials. Chapter 3 describes experiments where aggregates are created in environments that they normally would not be expected, and relies heavily on the spectroscopic techniques introduced in Chapter 2.
- Chapter 4 demonstrates the deactivation of the electron transfer reaction observed in Chapter 2 by alteration of the size of nanocrystals used as electron acceptors, and continues on to explain how nanoparticle size can influence concentration quenching efficiency.
- Chapter 5 takes one of the main conclusions from Chapter 2, which is that roughly 20 dyes can saturate the surface of a 2.5 nm diameter CdS particle, and studies whether the limitation of 20 dyes on the surface of the 2.5 nm particle is due to the size of the dye or a limited number of surface binding sites.

- Chapter 6 is principally concerned with the first modeling of an aggregate that has been performed with combinatorial mathematical modeling.
- Chapter 7 contains closing remarks.
- References
- Appendix A contains a derivation of the two-component Stern-Volmer model which may be useful for future researchers who may want to model a system similar to the systems outlined in this thesis, which contain competing excited state energy dissipation pathways.
- Appendix B contains special procedures and modified parameters needed for MD simulations, including the parameters needed to accurately reproduce the dynamics of the terthiophene molecule.
- Appendix C contains a short glossary and a list of acronyms.

1.4 Excluded Work

Portions of the work performed in my time at the University of Minnesota have been omitted from this thesis in an effort to focus on core components of my graduate work. Fundamental research such as the computational electronic structure calculations performed on ruthenium-containing dye complexes and on various porphyrin complexes are not included here. The results of the calculations on ruthenium dye complexes can be found in the Ph.D. thesis of Ryan Hue, as well as publications associated with Dr. Hue. The results of calculations on porphyrins can be found in the Ph.D. thesis of Andrew Bierbaum, as well as publications written on behalf of Dr. Bierbaum. DSSC device construction studies using the same ruthenium dye molecules that were also studied computationally are excluded as well, although they are likely to be published in an upcoming report by Dr. Hue and others. These device construction studies were generally successful and were based on original research that I performed upon arriving at the University of Minnesota, but inclusion into this thesis would not serve to add more information than was made available with Dr. Hue's thesis or will be made available in future publications under his name.

Chapter 2

Excited State Quenching Mechanism of a Terthiophene Acid Dye Bound to Monodispersed CdS Nanocrystals: Electron Transfer vs. Concentration Quenching

Oleate-capped CdS nanocrystals (NCs) dispersed in dichloromethane were found to quench the excited state fluorescence of the terthiophene derivative 3',4'-dibutyl-2-phenyl-2,2':5',2"-terthiophene-5"-carboxylic acid (**1-CO_2H**). Infrared and ^{1}H NMR spectroscopies provided evidence that **1-CO_2H** substitutes for oleate on the surface of the CdS NCs. Upon binding, the fluorescence of **1-CO_2H** is quenched. The importance of the carboxylate group in binding to the CdS NC was further established by examining the behavior of the same fluorophore where the carboxylic acid group was replaced with a bromo substituent (**1-Br**). The CdS NCs did not quench fluorescence of **1-Br** or broaden the NMR linewidths. For **1-CO_2H**, Stern-Volmer plots indicated a nearly linear increase in I_0/I as the CdS NCs concentration was increased, but as the dye/NC

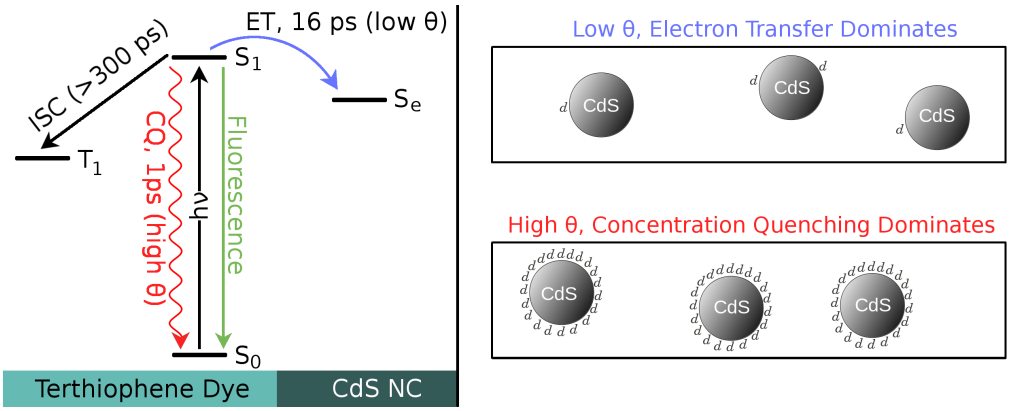

Figure 2.1: Jablonski diagram roughly showing energies of states relevant to charge transfer, along with processes that have been observed to occur in this work.

ratio reached ~20/1, I_0/I reached a maximum of ~8 and began to decrease. By a dye/NC ratio of 2/1 the I_0/I reached a steady value of ~ 2.5. The peak in the Stern-Volmer plot at a 20/1 ratio was consistent with a maximum in the contribution from concentration quenching at this coverage. Based on the appearance of the dyes radical cation spectrum at low dye/NC ratios, ultrafast transient absorption spectroscopy confirmed electron transfer from the singlet excited state of the dye to the CdS NC with a lifetime of 16 ps. At higher dye/NC ratios, the signal from the radical cation was much less dominant, and the decay of the singlet excited state was dominated by the concentration quenching process having a 1 ps lifetime.

2.1 Introduction

The fundamental physics of charge injection in dye sensitized solar cells (DSSC) are currently being explored in order to produce a low cost cell that is competitive with the efficiency and durability of silicon cells.[3,49,82,107–109] The heterogeneity of the nanocrystalline films used in DSSCs complicates the interpretation of the measured electron transfer rates. To minimize this problem, we are focusing on uniform-sized nanocrystal dispersions in a solvent compatible with the free dye, the free nanocrystals and the dye/nanocrystal dyads. This type of dyadic model system has been previously used to eliminate the variables introduced by the heterogeneity of the sintered semiconductor film found in a functional DSSC.[64,75,110–121] Among these studies oligothiophene chromophores were bound to TiO_2,[113,115] CdSe,[122] CdS,[116] and ZnO [120,121], but only in the ZnO case were the kinetics of charge injection measured and the appearance of the oxidized dye observed using ultrafast methods.

We are especially interested in examining the impact that quantum confinement has on charge injection. In quantum confined particles both the energies and densities of acceptor states have the potential to influence the rate of charge injection. The extent of the influence depends strongly on the thermodynamic driving force for the reaction. In previous studies of 3',4'-dibutyl-5"-phenyl-[2,2':5',2"-terthiophene]-5-carboxylic acid, **1-CO_2H**, bound to zinc oxide nanocrystals, the dye excited state was 1.3 eV above the conduction band edge of bulk ZnO and no measurable impact of the nanocrystal size on the rate of ET was observed.[120,121] With a porphyrin-based dye, where the excited state is only 0.8 eV above the bulk ZnO conduction band edge, the small changes observed in electron transfer rates as a function of nanocrystal diameter were attributed to changes in the density of acceptor states.

In the current study, we replace the ZnO nanocrystals with CdS nanocrystals while continuing to use **1-CO_2H**. Cadmium sulfide shows large changes in the band gap for relatively small changes in nanoparticle diameter. Furthermore, Yu and Peng established that monodisperse, oleate-capped CdS nanocrystals form stable dispersions and reported a valuable expression of the extinction coefficient as a function of particle size.[95] The latter is useful for preparing dispersions of known concentrations.[104] In comparison to ZnO the band gap of bulk CdS is 2.5 eV, and importantly, the lower

edge of the conduction band is roughly 0.8 eV higher than the ZnO conduction band edge.[123] We believe this places the acceptor levels at most 0.5 eV below the level of the excited state of the **1-CO_2H**,[120] making this dyad more sensitive to changes in the NC diameter. The ultrafast kinetic measurements were found to be more complicated than those for the **1-CO_2**/ZnO systems and highly dependent on the dye coverage of the NC surface. This paper focuses on the coverage dependence using 2.5 nm CdS NCs. At low coverage electron transfer dominates the quenching behavior. As the **1-CO_2**/NC ratio approaches saturation coverage of the NC surface, a faster event, assigned to concentration quenching, becomes dominant.

2.2 Experimental

Cadmium oxide (99.999 atom % Cd) was obtained from Strem Chemicals, oleic acid and dichloromethane were obtained from Fisher Chemicals, sulfur (USP grade) was obtained from JT Baker, and dichloromethane-D_2 (99.9 % D atom), hexanes (spectroscopy grade), and octadecene (90%) were obtained from Sigma Aldrich. All chemicals were used without further purification.

The terthiophene dye, 3',4'-dibutyl-5"-phenyl-[2,2':5',2"-terthiophene]-5-carboxylic acid (**1-CO_2H**) shown in Figure 2.2 was synthesized by the reported method.[120] Oleate-capped CdS nanocrystals (NCs) were synthesized by a literature procedure,[95] with the exception that the quantity of all reagents and solvents was doubled. Any further scale-up led to a broader particle size distribution and lower yield. The synthesis yielded a dispersion of purified CdS NCs at a concentration of 2.80x10^{-4} M in hexanes.

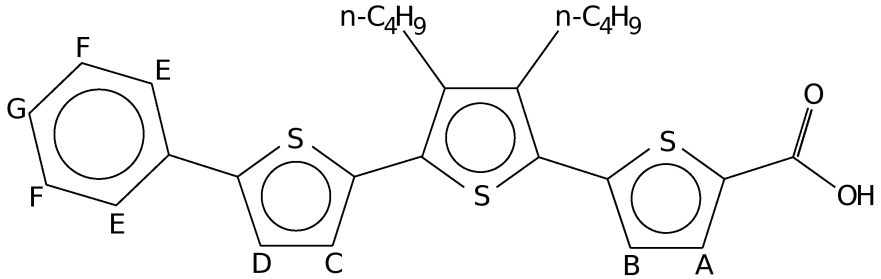

Figure 2.2: Dye structure with hydrogen labels for reference to ^{1}H NMR spectrum

2.2.1 Preparation of 1-CO_2/CdS NC Dispersions

The following procedures were performed in air. A stock solution of **1-CO_2H** was prepared by dissolving 2.11 mg (4.39 μmol) in 15 mL of CH_2Cl_2. The CdS NC stock dispersion was prepared by diluting the NC dispersion in hexane with CH_2Cl_2 to 2.80x10^{-5} M. Samples were prepared by mixing aliquots of each stock solution in 21 individual vials. The ratios of **1-CO_2H** to CdS NCs and corresponding concentrations in these mixtures are described in Table 2.1. The concentration of **1-CO_2H** has been kept constant in these samples at 2.20 x 10^{-4} M. Two dye-alone samples were created, one for analysis before all nc-CdS samples were analyzed and one for analysis directly following analysis of nc-CdS samples. The mixtures were allowed to stand overnight, after which the solvent was removed under a flow of $N_{2(g)}$ and the particles were redispersed in pure CD_2Cl_2 (0.8 mL). Attachment of the dye to nc-CdS and subsequent fluorescence quenching behavior was investigated using PL, FT-IR and ^{1}H-NMR spectroscopy. After UV-Vis, PL, and NMR analyses were completed on each sample, they were drop-cast from this solution onto NaCl plates for FT-IR analysis. In the case of sample 19 (dye:NC ratio of 1:1), a TEM grid was dipped into the final solution (after UV-Vis, PL and NMR) before IR analysis. TEM analysis was then performed to confirm that the NCs had not changed sizes appreciably during the course of the study. The steady-state emission spectra were recorded through two Spex Fluorolog 1680 0.22 m double spectrometer gratings equipped with a 450 W xenon source. All spectroscopy was performed in quartz cuvettes with a 3 mm path length in CD_2Cl_2 unless otherwise noted. ^{1}H NMR spectra were recorded on a 500 MHz Varian Inova with the standard 1D ^{1}H pulse sequence at a gain of 60 dB and 256 transients per spectrum. ^{1}H-NMR spectra for the dye/NC dispersions were scaled to render the noise level between 7.85 and 7.95 ppm equal in each spectrum. UV-Vis spectra were recorded using a DH 2000 BAL Mikropack deuterium/halogen source and an Ocean Optics USB4000 detector. IR spectra were measured on specimens drop cast from solution onto a NaCl plate and dried under a stream of $N_{2(g)}$. A Thermo Nicolet 670 FTIR was used with each spectrum comprising 128 scans. Bright field TEM images were collected on a Tecnai G^2 F30 field emission gun transmission electron microscope.

Sample	Moles of nc-CdS	Concentration of nc-CdS	**1-CO_2H**:nc-CdS Ratio
1	8.79 x 10^{-10} mol	1.10 x 10^{-6} M	200:1
2	1.76 x 10^{-9} mol	2.20 x 10^{-6} M	100:1
3	2.20 x 10^{-9} mol	2.75 x 10^{-6} M	80:1
4	2.51 x 10^{-9} mol	3.14 x 10^{-6} M	70:1
5	2.93 x 10^{-9} mol	3.66 x 10^{-6} M	60:1
6	3.52 x 10^{-9} mol	4.40 x 10^{-6} M	50:1
7	4.40 x 10^{-9} mol	5.49 x 10^{-6} M	40:1
8	5.02 x 10^{-9} mol	6.28 x 10^{-6} M	35:1
9	5.86 x 10^{-9} mol	7.33 x 10^{-6} M	30:1
10	7.03 x 10^{-9} mol	8.79 x 10^{-6} M	25:1
11	8.79 x 10^{-9} mol	1.10 x 10^{-5} M	20:1
12	1.00 x 10^{-8} mol	1.26 x 10^{-5} M	17.5:1
13	1.17 x 10^{-8} mol	1.47 x 10^{-5} M	15:1
14	1.41 x 10^{-8} mol	1.76 x 10^{-5} M	12.5:1
15	1.76 x 10^{-8} mol	2.20 x 10^{-5} M	10:1
16	2.34 x 10^{-8} mol	2.93 x 10^{-5} M	7.5:1
17	3.52 x 10^{-8} mol	4.40 x 10^{-5} M	5:1
18	7.03 x 10^{-8} mol	8.79 x 10^{-5} M	2.5:1
19	1.76 x 10^{-7} mol	2.20 x 10^{-4} M	1:1
DA	0	1.10 x 10^{-6} M	∞
DA	0	1.10 x 10^{-6} M	∞

Table 2.1: Concentrations of nc-CdS in the samples used in titration experiment described in text, and ratio of dye molecules to nc-CdS. Concentration of dye molecules was 2.20 x 10^{-4} M for each sample, and these dye molecules were titrated with nc-CdS.

2.2.2 Reaction of Cadmium Acetate with 1-CO_2H

A small excess of cadmium acetate (1.3 mg, 5.6 x10-6 mol) was mixed with **1-CO_2H** (4.8 mg, 9.7 x 10-6 mol) in methanol. After the mixture was stirred for 20 min following dissolution of the starting materials, the volatiles were removed under vacuum. The sample for NMR spectroscopy was prepared by dissolving the residue in a 2:1 mixture of CD_2Cl_2 and CD_3OD.

2.2.3 Frequency Resolved Pump-Probe Measurements

Pump-probe experiments were performed using a home-built, amplified, 1 kHz Ti:sapphire laser system that produces 1 mJ, 1.51 eV, 80 fs (Gaussian, FWHM) pulses as described previously.[120] The light is split and a portion was frequency doubled in a 1 mm BBO crystal for excitation at 3.02 eV. The resulting light was reflected off 3 dichroic mirrors to remove any residual 1.51 eV light, and 100 nJ/pulse was focused to a spot size of 120 μm at the sample by a 5 cm parabolic mirror. Focusing another portion of the 1.51 eV light into a 2 mm sapphire plate produced a probe continuum (1.25-2.75 eV). This was re-collimated, and then focused and crossed with the excitation light in the sample using the same 5 cm parabolic mirror. Polarization of the 3.02 eV pulse was set to the magic angle of 54.7° relative to the continuum probe to discriminate against anisotropic dynamics. After the sample, the probe was collimated, filtered through a 1 mm cuvette consisting of 1,1'-diethyl-4,4'-dicarbocyanine iodide to remove excess 800 nm light, and focused into a Princeton Instruments 2150 monochromator that dispersed the light onto a Hamamatsu 256 pixel silicon diode array resulting in an effective resolution of 2 nm. The array was collected at the 1 kHz laser repetition rate, and the pump was modulated to 500 Hz using a mechanical chopper. The change in optical density (O.D.) was then calculated for every sequential pair of excitation pulses and subsequently averaged over about 50,000 shot pairs at each time delay between excitation and probe. All data were time corrected for temporal chirp in the probe as described previously.[120] All samples were continuously flowed through the 1 mm optical path length quartz cuvette.

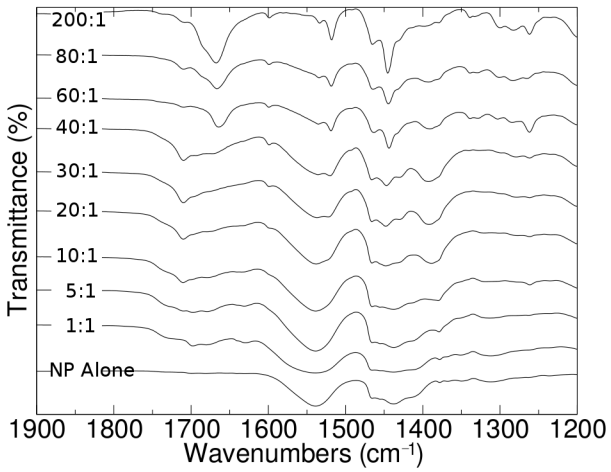

Figure 2.3: IR spectral changes as a function of dye-to-CdS NC ratio. The bottom spectrum represents a nc-CdS sample without dye.

2.3 Results

2.3.1 Infrared Spectroscopy

Figure 2.3 shows the IR spectra of samples with different dye to NC ratios that were drop-cast onto a NaCl window and dried under a stream of $N_{2(g)}$. The strong signal at 1665 cm^{-1}, which corresponds to the ν_{CO} of **1-CO_2H**, diminishes as the ratio of nanocrystals to dye molecules is increased. The increased intensities at 1540 and 1440 cm^{-1} correspond to a combination of frequencies associated with the mixture of NCs capped with **1-CO_2^-** and oleate.[47] The peak at 1712 cm^{-1} corresponds to the carbonyl stretch in free oleic acid, and increases as the concentration of CdS NCs increases up to a ∼20:1 ratio. This signal likely arises from a combination of oleate displaced from the surface by the dye molecule and residual oleic acid remaining from nanocrystal synthesis. As the dye:NC ratio approaches 1:1 the free oleic acid signal diminishes suggesting that some **1-CO_2H** can be accommodated on the CdS NC without causing dissociation of oleic acid.

As the dye:NC ratio is decreased, the point at which the 1665 cm^{-1} stretch can no longer be resolved from the baseline occurs approximately at a dye:NC ratio of 20:1. From this point on, free dye in solution is no longer detectable by IR spectroscopy.

IR spectra were particularly difficult to portray in a fashion that was efficient with usage of space while allowing the reader to detect the relatively small changes that occurred from sample to sample. For this reason, here we present the IR spectra in Figures 2.4, 2.5, 2.6, 2.7 in greater detail than in Figure2.3, which gives a good overview of important trends. It can be seen from analysis of the carbonyl signal of the **1-CO_2H** at 1667 cm^{-1} that **1-CO_2H** is continuously perturbed from sample 1 to sample 8, with the loss of **1-CO_2H** carbonyl stretch roughly compensated for by gain in the carbonyl stretch of oleic acid at 1711 cm^{-1}. This is indicative of a displacement reaction, as was suggested above.

It is also important to recognize that the carbonyl stretch disappears around the same time that the NMR spectrum is most featureless and the UV-Vis develops an isosbestic point. Around spectrum i (sample 9), the carbonyl stretch of **1-CO_2H** is overwhelmed by peaks that begin to grow in at higher concentrations of nc-CdS. These peaks appearing late in the titration are seemingly associated with the surface of the nanoparticle, as is shown in the upper right spectrum of Figure 2.7.

Lastly, it should be noted that the **1-CO_2H** molecule does not lend itself well to drop-casting onto salt plate, and this is the cause of the very weak signal in the **1-CO_2H** spectrum in Figure 2.7. While the carbonyl stretch extends far below the baseline, the rotational fine structure of water vapor can also be seen because of the very minute scale of the y-axis. It is likely that a KBr pellet would have worked better for this purpose, but the aim was to keep everything as similar to the previous samples with nc-CdS that were run as possible.

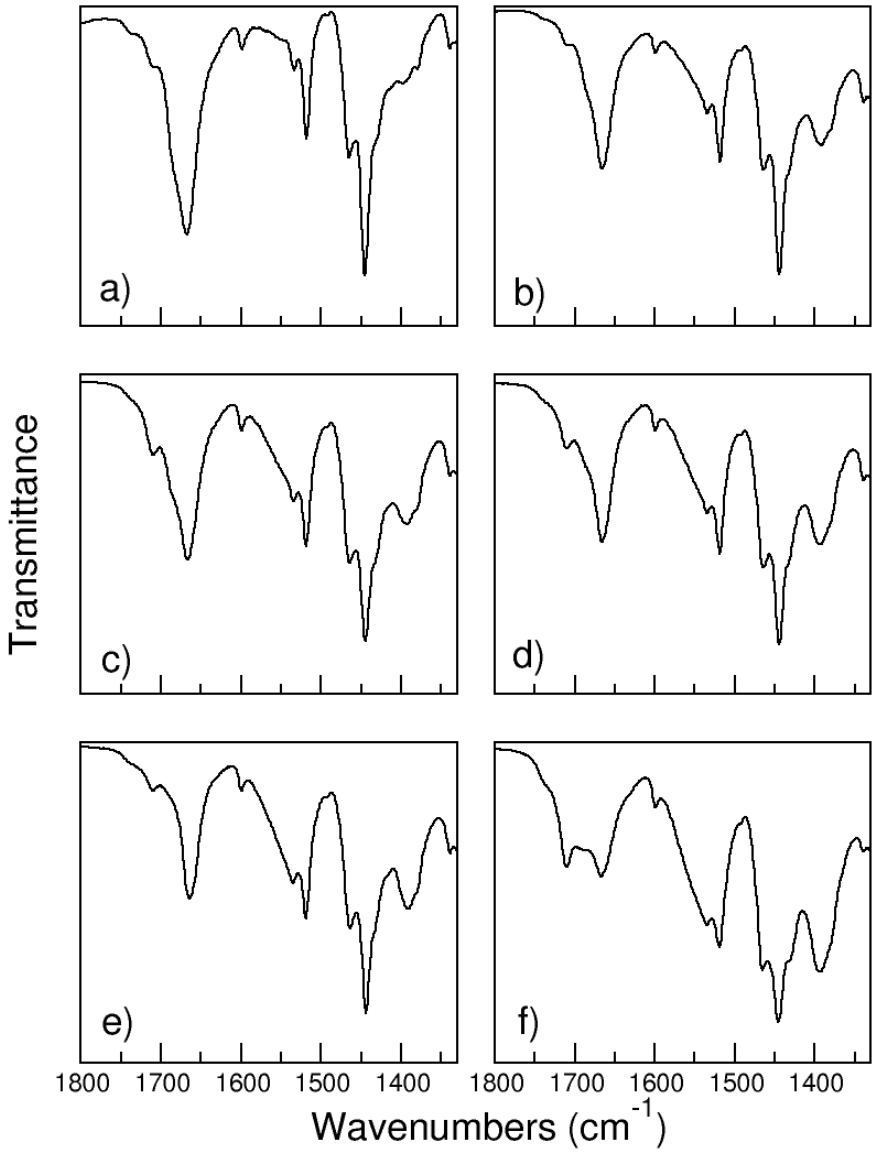

Figure 2.4: IR spectra of **1-CO_2H** with increasing amounts of nc-CdS. Spectra were collected as described above, drop cast from solutions from table 2.1. The ratio of **1-CO_2H**:nc-CdS in each sample from a) to f) is 200:1, 100:1, 80:1, 70:1, 60:1, and 50:1, in that order.

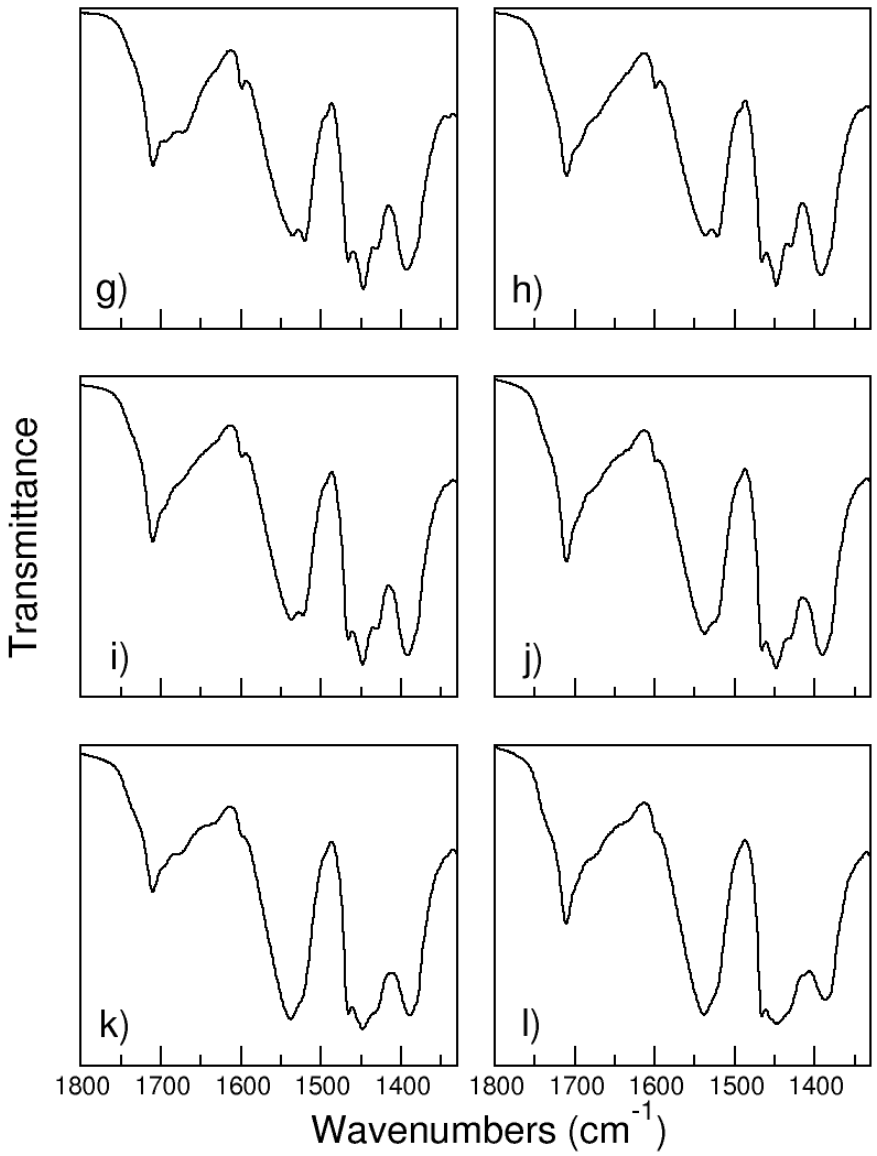

Figure 2.5: IR spectra of **1-CO_2H** with increasing amounts of nc-CdS. Spectra were collected as described above, drop cast from solutions from table 2.1. The ratio of **1-CO_2H**:nc-CdS in each sample from g) to l) is 40:1, 35:1, 30:1, 25:1, 20:1, and 17.5:1, in that order.

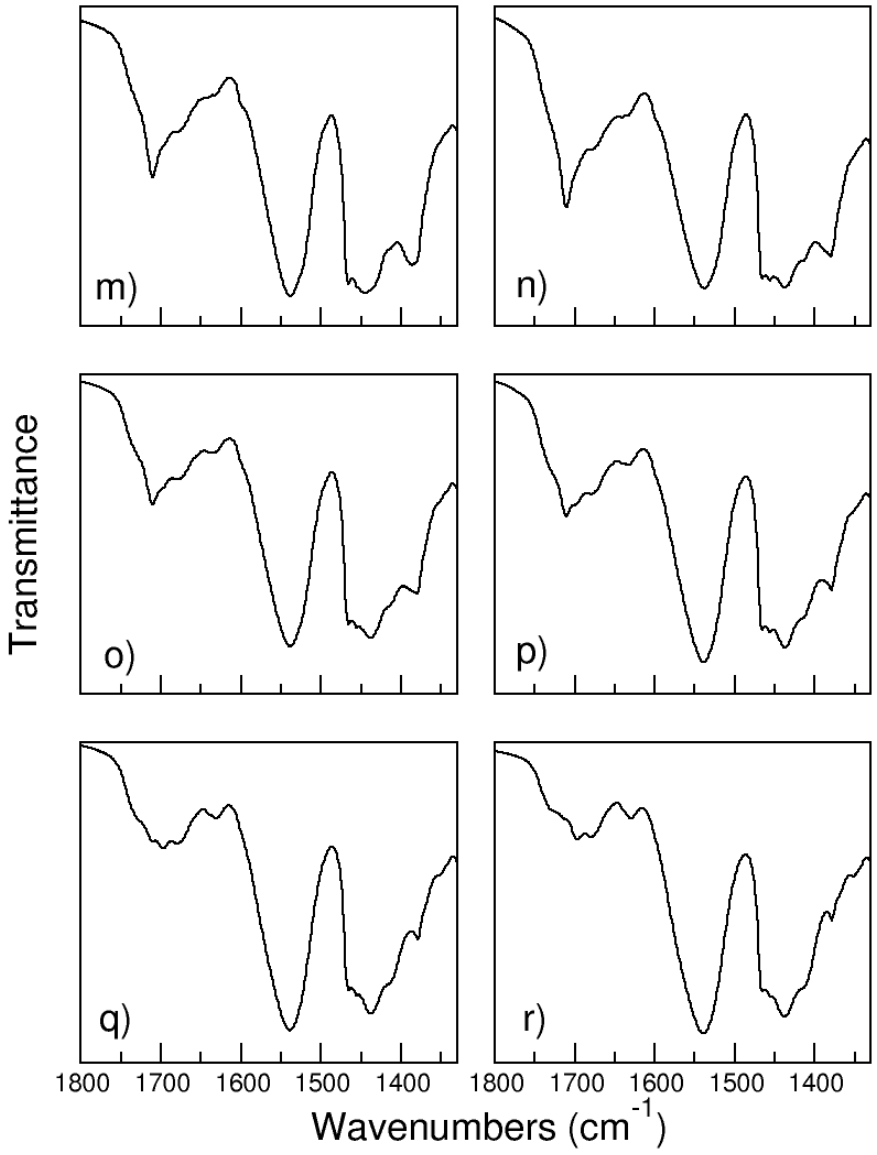

Figure 2.6: IR spectra of **1-CO_2H** with increasing amounts of nc-CdS. Spectra were collected as described above, drop cast from solutions from table 2.1. The ratio of **1-CO_2H**:nc-CdS in each sample from m) to r) is 15:1, 12.5:1, 10:1, 7.5:1, 5:1, and 2.5:1, in that order.

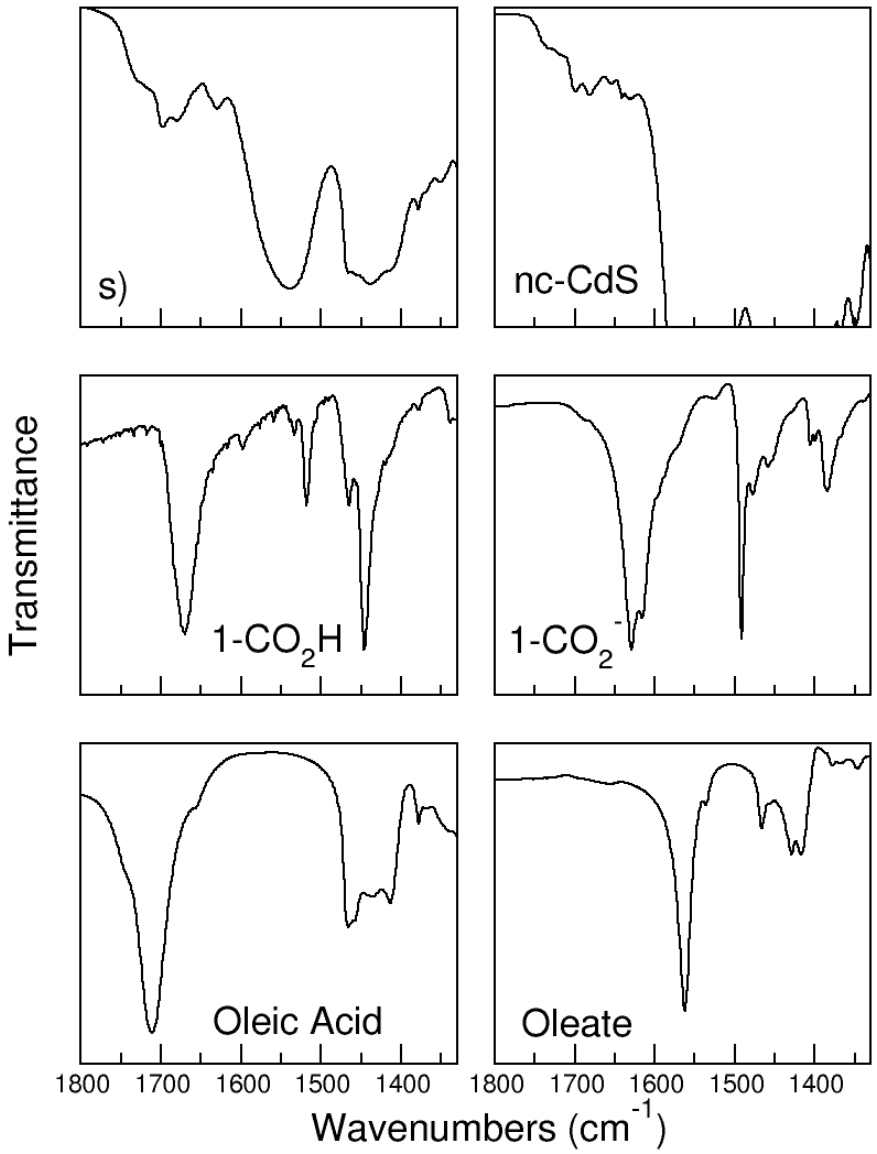

Figure 2.7: IR spectra of **1-CO_2H** in the presence of equimolar nc-CdS (spectrum s), nc-CdS without **1-CO_2H**, **1-CO_2H** alone, **1-CO_2^-**, oleic acid, and oleate. The latter two spectra were collected on KBr pellets, and not drop-cast from solution onto NaCl plates as was the case with the other samples.

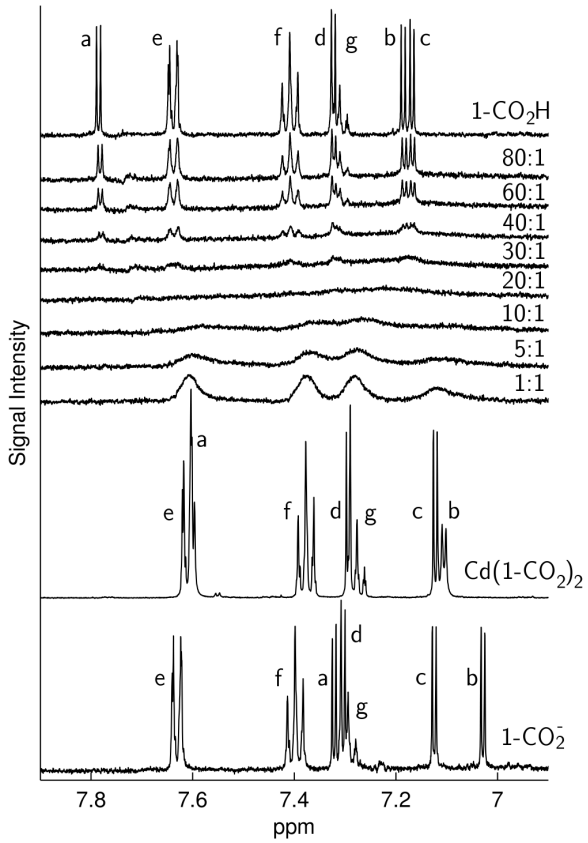

Figure 2.8: ^{1}H NMR spectra in the aromatic region of **1-CO$_2$H**, Cd(**1-CO$_2$**)$_2$, [Bu$_4$N][**1-CO$_2$**], and of solutions with the indicated dye-to-NC ratio.

2.3.2 ^{1}H NMR Spectroscopy

The aromatic region of the ^{1}H NMR spectra of pure **1-CO$_2$H**, Cd(**1-CO$_2$**)$_2$ and [Bu$_4$N][**1-CO$_2$**] in CD_2Cl_2 as well as for a sequence of solutions with decreasing dye to NC ratios is shown in Figure 2.8 along with assignments of the resonances from Figure 2.2. As NCs are added to the mixture, a continuous trend of broadening occurs. Broadened NMR lineshapes of ligands attached to nanoparticles have been reported previously,[124–128] and possible mechanisms for this broadening are detailed below. At a dye/NC ratio of 20 the peaks from **1-CO$_2$H** are broadened into the baseline, and we label this point P_t. Further addition of NCs resulted in signal recovery, albeit as broad resonances. The

phenyl protons showed the largest recovery, and the signal for the hydrogen adjacent to the carboxylate (labeled A) never reappeared. The spectrum of a 1:1 dye/NC dispersion obtained at 50°C in $CDCl_3$ did not exhibit significantly different line shapes. The chemical shifts of the four broad observed resonances in the 1:1 spectrum match well with some of the sharp resonances observed in a solution of the cadmium salt of 1-CO_2^-.

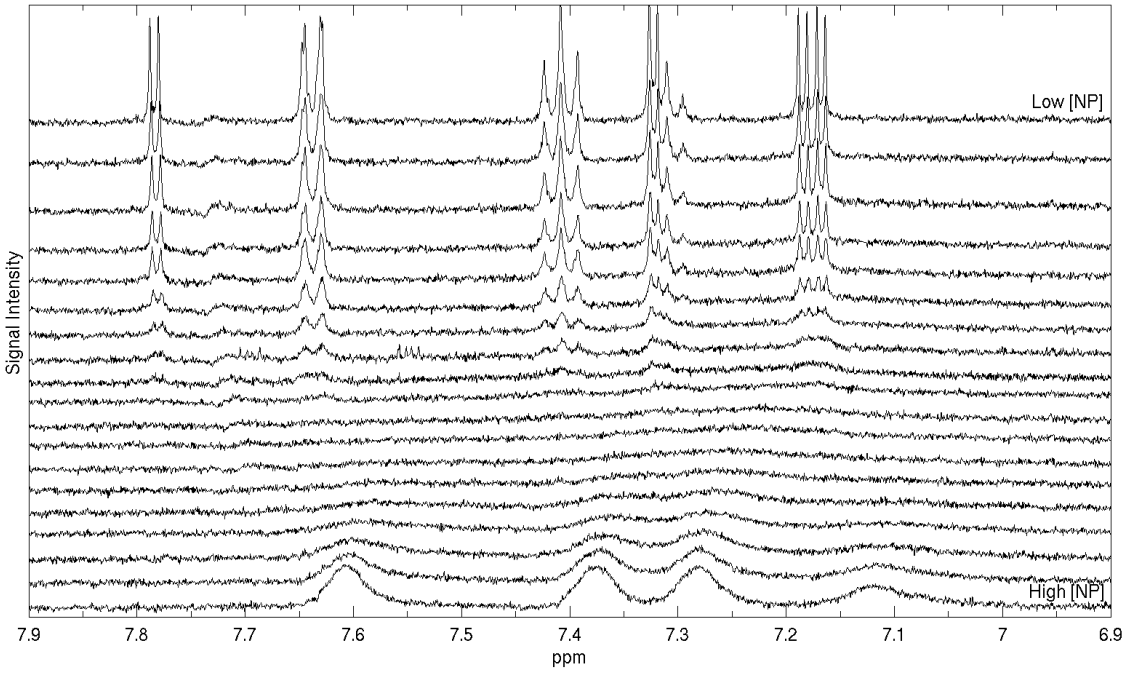

Figure 2.9: NMR of all samples from table 2.1 except the dye alone samples, which can be seen in figure 2.8.

Because the full range of NMR spectra for all nineteen samples is quite crowded, we chose to eliminate some of the spectra in Figure 2.8 for clarity's sake. NMR spectra of each sample in Table 2.1 are presented in Figure 2.9, and it can be seen that the trend is continuous and smooth. The trend is uninterrupted and the only change in the trend is a small amount of impurity in sample 8, which is likely the plasticizer bis(2-ethylhexyl) phthalate. This impurity most probably originated from contact between the cap of the NMR tube and the CD_2Cl_2 solvent.

The spectrum at the beginning of the titration of **1-CO_2H** with nc-CdS is nearly identical to the spectrum of **1-CO_2H** alone, and as the concentration of nc-CdS is

increased, the titration reaches P_t, where the signal from the unperturbed dye is no longer detectable. At the end of the titration, the phenyl peaks are much more intense than the rest of the aromatic protons. This can be seen as a result of the phenyl group rotating freely, whereas the rest of the aromatic protons are constrained by the conjugation across the terthiophene portion of the molecule. The lack of signal intensity in the spectrum near P_t means the aromatic portions of the molecules are constrained, most likely by neighboring dye molecules in a $\pi - \pi$ stacking motif. NOESY experiments were attempted to give a clearer picture of the interactions between the molecules on the surface, but were unsuccessful as the signals showed no cross peak in our short experiment.

Electronic structure calculations (not included) show that the thiophene sulfur can coordinate to metal sites on the surfaces of II-VI semiconductor nanoparticles, so it was necessary to determine what the attachment mechanism is for **1-CO_2H**. NMR spectroscopy was also useful for determining whether or not the **1-Br** molecule (a bromo substituent replaced the carboxylate functional group) could attach via the thiophene sulfurs, **1-Br** was mixed with a CH_2Cl_2 dispersion of the NCs in a 1:1 ratio. The NCs had no effect on the ^{1}H resonances of **1-Br** (Figure 2.10). This does not preclude possibility of the dye molecule from binding to the nc-CdS surface after the carboxylate group from **1-CO_2H** forms a coordinating bond with other atoms on the nc-CdS. However, this seems unlikely given that the phenyl group from **1-CO_2H** would be more constrained on the surface and unlikely to have the freedom to rotate as is seemingly displayed in the 1:1 sample of the NMR (Figure 2.8 and 2.9).

2.3.3 Static Fluorescence Quenching

Figure 2.11 illustrates the UV-Vis absorption and emission spectra of samples of pure nc-CdS and **1-CO_2H** in CH_2Cl_2. In the absence of nanocrystals **1-CO_2H** fluoresces with a max at 501 nm upon excitation at 420 nm. Figure 2.11 shows that the emission quenching upon addition of nc-CdS was complex. As the NC concentration increased the emission maximum remained constant at 501 nm and the intensity decreased to the point where the dye:NC ratio reached ~20:1 (point P_t, as defined above). Further addition of NCs resulted in a sharp decrease in I_0/I and a gradual leveling to a final value of 2.5. Along with the decrease in luminescence intensity, addition of NCs past

P_t caused the emission peak to blue-shift to a λ max of 495 nm for a final dye:NC ratio of 1:1. Stern-Volmer plots detailing experiments using both 400 and 420 nm excitation wavelengths are shown in Figure 2.12, and a Stern-Volmer plot with the 420 nm data compared with a Stern-Volmer-type analysis for the NMR data is shown in Figure 2.13.

From Figure 2.12, it appears the 400 nm wavelength creates an excited state that is quenched better across the range of nc-CdS concentrations than that created by the 420 nm wavelength excitation. The difference can be explained by several theories, including that the higher-energy S_1 state (created by 400 nm excitation) will have overlap with more states in the nc-CdS, and this will make the ET event faster and more competitive with the fluorescence process when both pathways are available.

Figure 2.14 shows the spectra of samples 1-19 from Table 2.1 in their entirety. As the dyes are perturbed from their protonated, unattached states, their peak positions are unaffected. After the **1-CO_2H**:nc-CdS ratio reaches 20:1 however, their peak positions begin to shift to the blue and increase in intensity. This is expected because **1-CO_2^-** has a larger fluorescence quantum yield and bluer peak positions than does **1-CO_2H** (Figure 2.15).

The shift of the PL peak to the blue upon deprotonation is a result of the appearance of a vibrational progression. Estimating the peak positions for the progression puts the coupling frequency at about 1100 cm^{-1} (with two significant digits), which is close to a large 1114 cm^{-1} mode that is visible in the protonated spectrum and a 1102 cm^{-1} mode that is visible in the deprotonated spectrum. C-O modes can be found in this region of the IR spectrum, and this is a reasonable explanation for the sensitivity of the presence of the vibrational progression to the protonation state of the carboxylic acid moiety.

As in the case of the NMR spectral changes, the PL data for **1-Br** shows that the Br-substituted terthiophene is not able to coordinate to the surface of nc-CdS, as the fluorescence intensity is nearly identical between the samples with 1:1 **1-Br**:nc-CdS and **1-Br** alone (Figure 2.16).

2.3.4 UV-Vis Spectroscopy

Figure 2.17 shows select UV-Vis absorption spectra from the titration of **1-CO_2H** in dichloromethane with CdS NCs. As the dye:NC ratio decreased from 200:1 to 20:1, the

molar absorption of the dye molecules increased slightly. Upon further NC addition, a well-defined isosbestic point is observed at 450 nm as well as a monotonic narrowing of the spectra on the low energy side of the absorption peak.

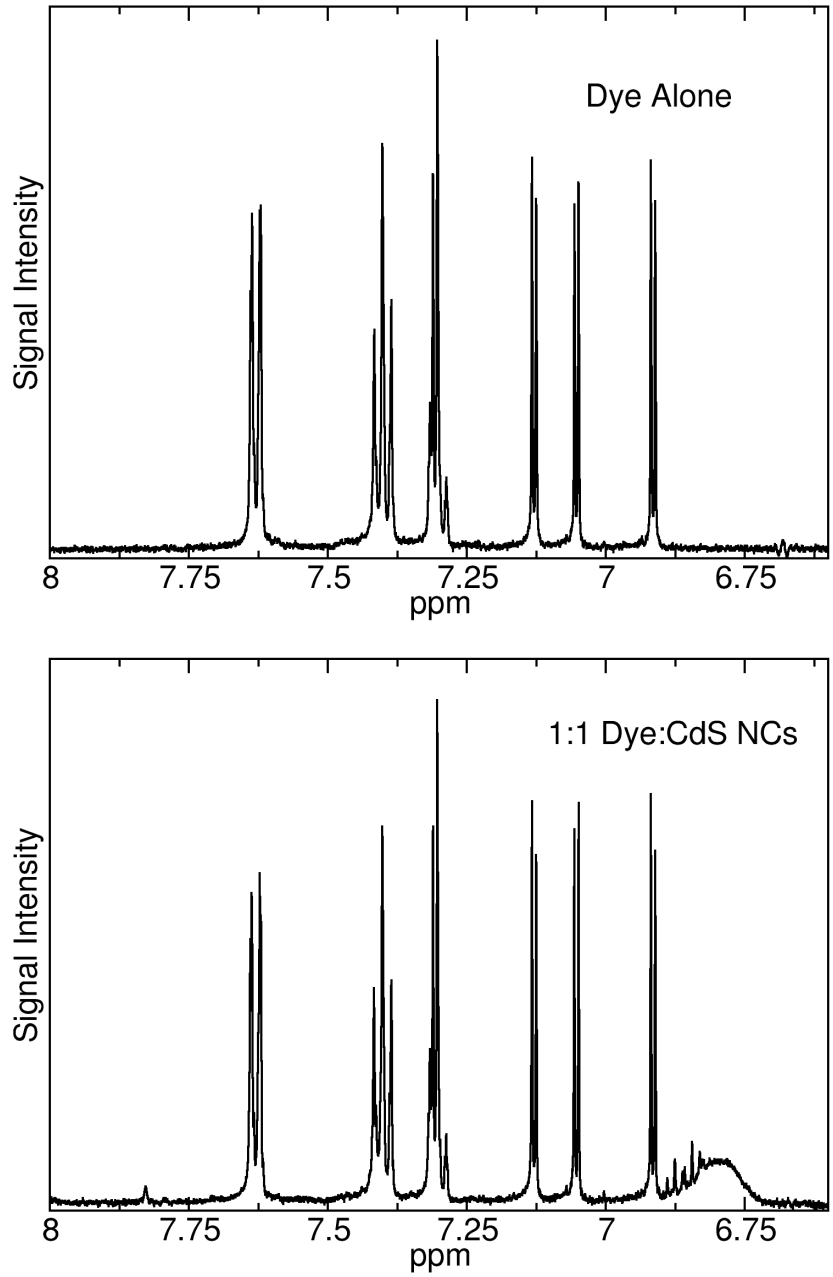

Figure 2.10: NMR of **1**-Br alone, and with a 1:1 ratio of nc-CdS. It can be seen that there is no difference in the dye proton shapes or positions, and the only difference is that the sample with nc-CdS displays a large, broad peak centered at 6.8 ppm. This peak is seen in ^{1}H-NMR spectrum of the nanoparticles alone.

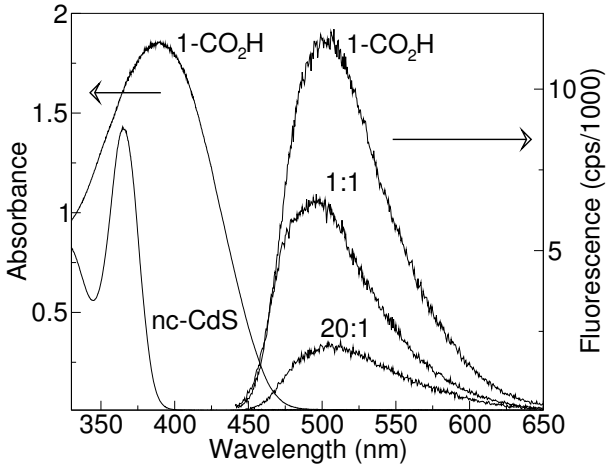

Figure 2.11: UV-visible spectra of nc-CdS and **1-CO$_2$H**, and fluorescence spectra of **1-CO$_2$H** and **1-CO$_2$**/nc-CdS dyads in a 1:1 and 1:20 molar ratio.

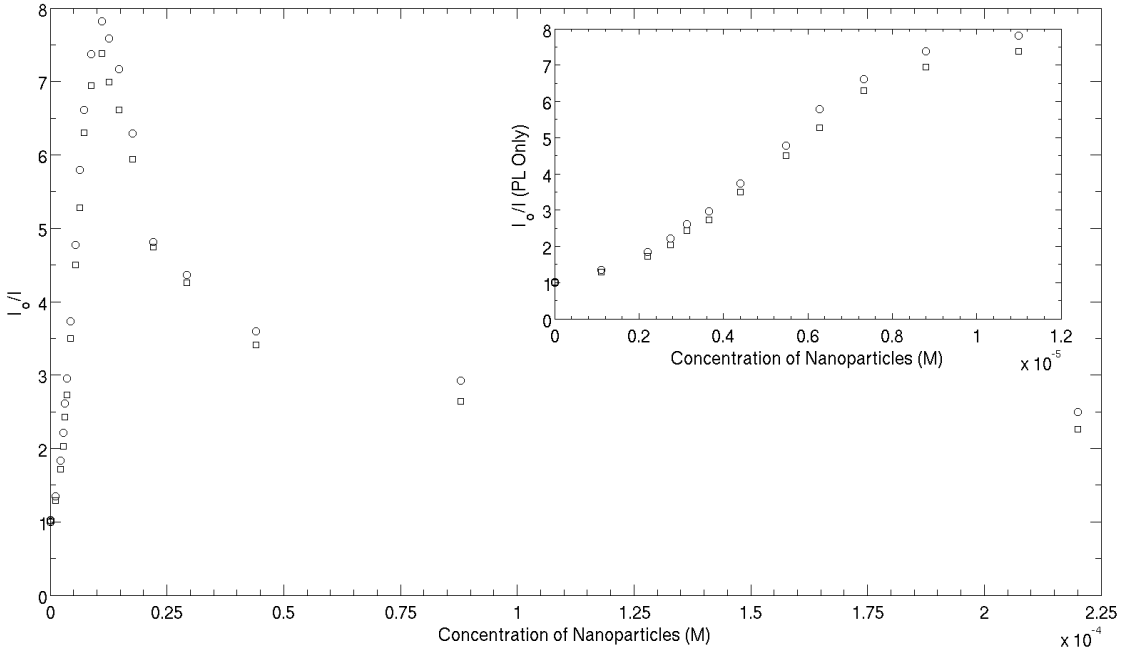

Figure 2.12: Stern-Volmer experiment showing that 400 nm and 420 nm excitation wavelengths behave quite similarly.

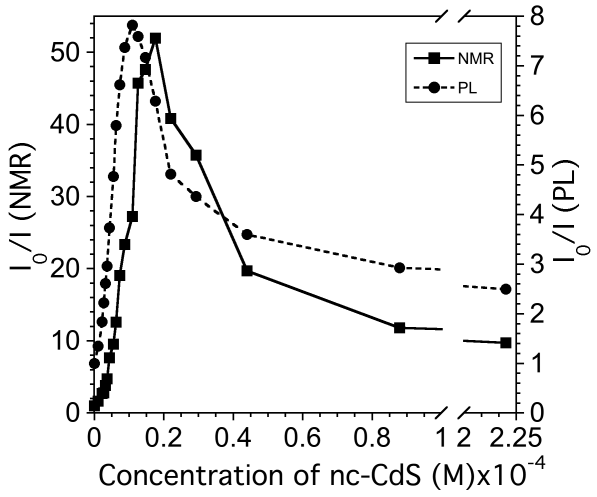

Figure 2.13: Graph comparing the I_0/I for fluorescence (Stern-Volmer) as a function of the concentration of added nc-CdS (dots) to the I_0/I of the ^1H NMR intensity spectral values based on the signal of H_e at 7.65 (squares). In analogy to the Stern-Volmer graph, the I_0 was based on the signal intensity for pure **1-CO_2H**

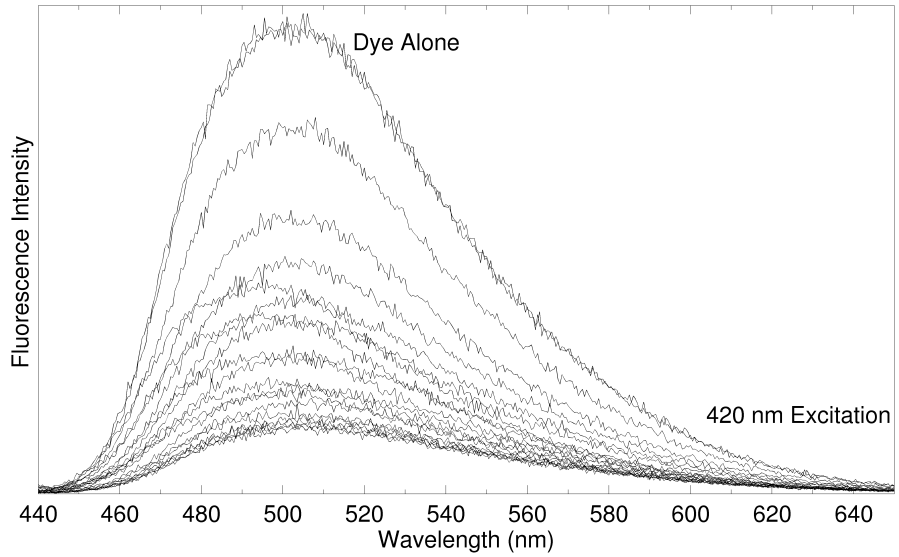

Figure 2.14: All PL spectra are shown. A recovery of the fluorescence intensity can be seen. The samples that show this behavior also show a slight blue-shift in their peak intensity.

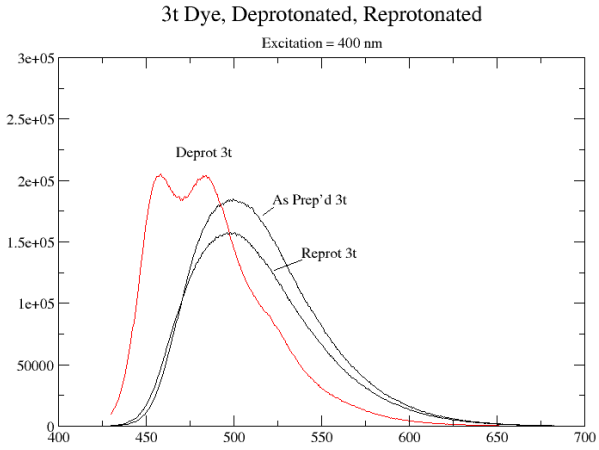

Figure 2.15: PL spectra of **1-CO$_2$H** and **1-CO$_2^-$**, showing that the fluorescence spectrum of the **1-CO$_2$H** molecule is dependent on the protonation state for both quantum yield and peak position of fluorescence. The vibrational progression of the **1-CO$_2^-$** is noticeable, and the inter-peak energy difference is roughly 1140 cm^{-1}, which coincides with certain IR features.

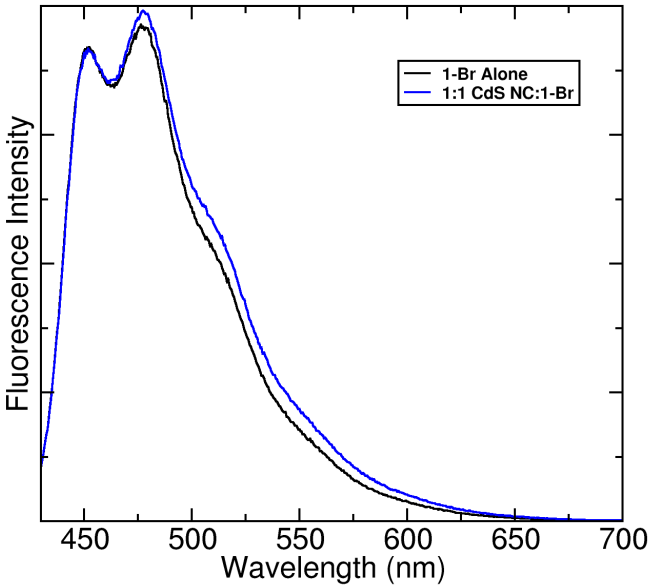

Figure 2.16: **1-Br** both alone and in the presence of nc-CdS in a 1:1 ratio.

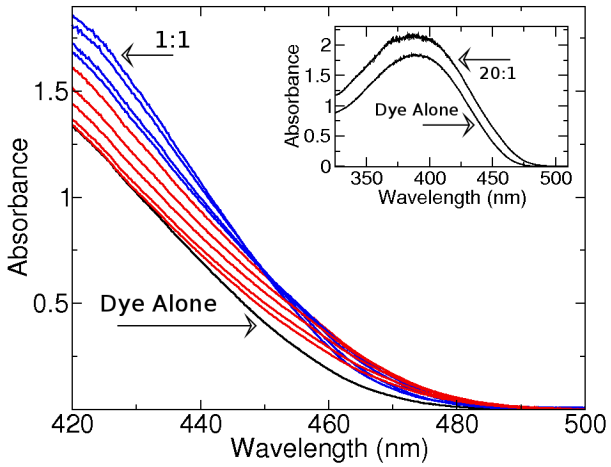

Figure 2.17: Electronic absorption spectrum of the long wavelength tail of **1-CO_2H** as a function of increasing concentration of nc-CdS. The starting concentration of **1-CO_2H** for all samples was 0.22 mM (black line). The red lines correspond to dye/nc-CdS ratios ranging from 100:1 to 25:1. The dye/nc-CdS ratios for the blue lines are 17.5:1, 12.5:1, 5:1, and 1:1. The inset shows the spectrum of **1-CO_2H** (lower) and **1-CO_2**/nc-CdS (20:1).

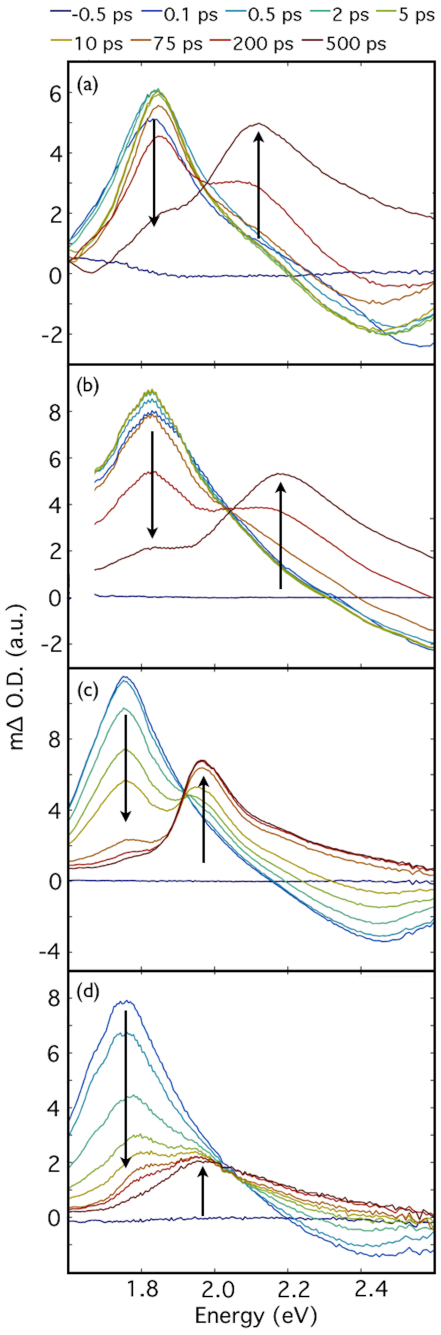

Figure 2.18: Full frequency pump-probe measurements of CH_2Cl_2 solutions of (a) **1-CO_2H**, (b) **1-CO_2^-**, (c) **1-CO_2**/nc-CdS in a 2:1 ratio, and (d) **1-CO_2**/nc-CdS in a 25:1 ratio.

2.3.5 Pump-Probe Spectroscopy

Figure 2.18a shows a selection of transients observed in spectrally resolved pump-probe measurements of **1-CO_2H** in dichloromethane. The negative peak (2.48 eV) observed at early delay times occurs at the same wavelength as the emission from **1-CO_2H** in dichloromethane and is assigned to stimulated emission. The large positive peak around 1.85 eV appears within the <60 fs time resolution of the experiment and is assigned to the transient absorption of the initially excited singlet S_1 state of the dye. The protonated dye alone, Figure 2.18a, is dominated by a single exponential time scale of 315 ps with correlated decay of the low energy feature and growth of the broad peak centered at 2.25 eV with an isosbestic point at 1.97 eV. This process is assigned to intersystem crossing of the singlet to the triplet.[120] The deprotonated dye alone, Figure 2.18b, shows a similar intersystem crossing process as the protonated dye with a time scale of 300 ps. However, in this case the isosbestic point is centered at 2.04 eV and the triplet peak is blue-shifted by 0.06 eV with respect to its protonated version. No significant spectral changes were observed in its singlet state absorption.

Dye Plus CdS Nanocrystals

Pump-probe measurements were conducted on solutions containing two dye:NC ratios, 2:1 and 25:1. In both cases excitation leads to the appearance of a singlet excited state that is red-shifted by 0.1 eV compared to free **1-CO_2H** or **1-CO_2^-** suggesting that the electronic structure of the dye is perturbed upon binding to the CdS NCs. Addition of the NCs results in the appearance of faster time scale decays of the initially excited singlet state and the correlated appearance of a new absorption feature at 1.97 eV that we assign to the radical cation of the dye based on previous work.[120] The decay at 1.70 eV primarily reflects loss of the absorption of the initially excited singlet state, and this was fitted with a sum of exponentials. The resulting fits are shown in Figure 2.19, and the associated fitting parameters are presented in Table 2.2. The fits at 1.70 eV show that in all cases there is a long time scale event, >300 ps, that becomes longer when the NCs are present. In both the 2:1 and 25:1 cases the long decay that remains indicates that roughly 20% of the excited dye relaxes via intersystem crossing to the triplet. This time scale is modestly longer than the ISC time constant for the dye alone

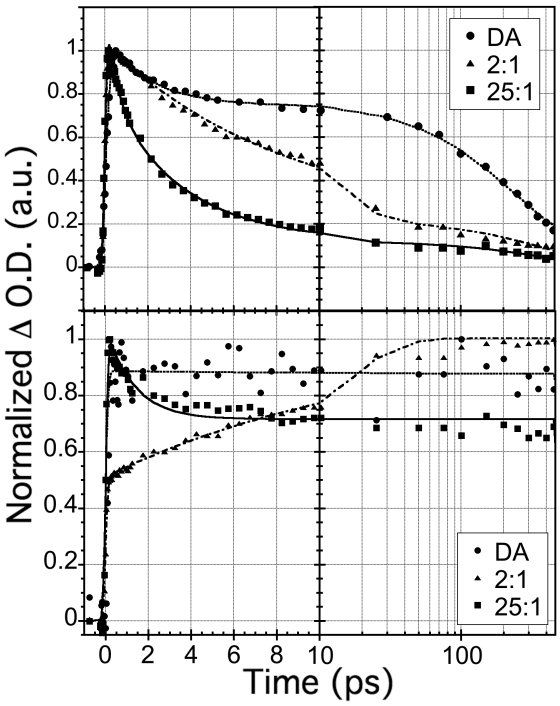

Figure 2.19: (Top) Decay at 1.70 eV, which primarily reflects loss of absorption of the initially excited singlet state. (Bottom) Time evolution at 1.97 eV, which corresponds to the isosbestic point in the protonated dye alone (DA) sample (see Figure 2.18a). Lines represent the fitting to a sum of exponential functions.

in solution, a dilation that appears to result from surface binding.[129] This indicates that about one-fifth of the binding sites are inactive with respect to the faster relaxation pathways, including excited state charge transfer.

In the dye alone there is a faster decay component at 3.3 ps, and a decay of 4 ps remains with the addition of NCs. Given the consistency in the presence and absence of the NCs, we assign this to inherent dynamics associated with relaxation of the excited dye. At a dye:NC ratio of 2:1, we observe an additional decay with a time scale of 16 ps that is correlated with a rise in absorption associated with the cation discussed below. At 25:1 the 16 ps decay is suppressed along with the cation absorption signal and a new, faster decay with a time constant of 1 ps appears. Figure 2.19b shows the time evolution probing at 1.97 eV. By selecting a probe energy that is nearly coincident

dye/nc-CdS (probe, eV)	τ_1 (ps)	a_1	τ_2 (ps)	a_2	τ_3 (ps)	a_3
dye (1.70)	3.3 ± 0.7	0.24 ± 0.02	315 ± 17	0.74 ± 0.01		
2:1 (1.70)	4 ± 1	0.3 ± 0.1	16 ± 6	0.4 ± 0.2	655 ± 198	0.17 ± 0.02
2:1 (1.97)	13 ± 2	0.49 ± 0.03				
25:1 (1.70)	0.96 ± 0.05	0.49 ± 0.06	4.4 ± 0.6	0.52 ± 0.08	485 ± 132	0.11 ± 0.01
25:1 (1.97)	1.3 ± 0.4	0.32 ± 0.12				

Table 2.2: Summary of Fits to Ultrafast Measurements, With Uncertainties

with both the isosbestic point in the dye alone sample and the absorption maximum for the cation, contrast is provided to help isolate the rate of cation formation. In the case of the dye alone, the response is well represented as a Heaviside function representing instantaneous creation of the excited state without subsequent dynamics. At low dye coverage, 2:1, the decay is well fitted with the Heaviside function and an additional exponential rise with a time constant of 13 ps. This rise is single exponential and mirrors the decay of the excited state measured at 1.70 eV indicating charge injection from the singlet excited state. At the higher dye coverage, 25:1, no rise is observed, but there is a 1.3 ps decay. Similarity of this 1.3 ps decay with the 1 ps decay measured at 1.70 eV suggests that the contribution from the decay of the initially excited singlet state has overwhelmed any potential signal from cation rise. As a result, on first inspection of the 1.97 eV slice, there is no direct evidence for the appearance of the cation in the 25:1 sample. Acceleration of the excited singlet decay together with a reduction in the relative cation absorption indicates the addition of an alternative relaxation pathway at high coverage.

2.3.6 TEM

Doubt can be cast onto whether the nanoparticles are still present after dye molecules have been added to them. A reasonable argument is that the carboxylic acid from **1-CO_2H** can etch the surface of the nc-CdS to an extent that there are surface states that can accept an electron from **1-CO_2H**. This question is further discussed in another chapter of this thesis. However, TEM images of particles at the 1:1 point in the titration also suggest that there is a negligible amount of particle size evolution at this point. The images in Figure 2.20 depict nanocrystals that are generally uniform in size and shape.

While certain crystals can be found that are surprisingly free of defects (Figure 2.20c), most of the crystals seem to have irregular lattice fringes which may reveal stacking faults and surface defects.

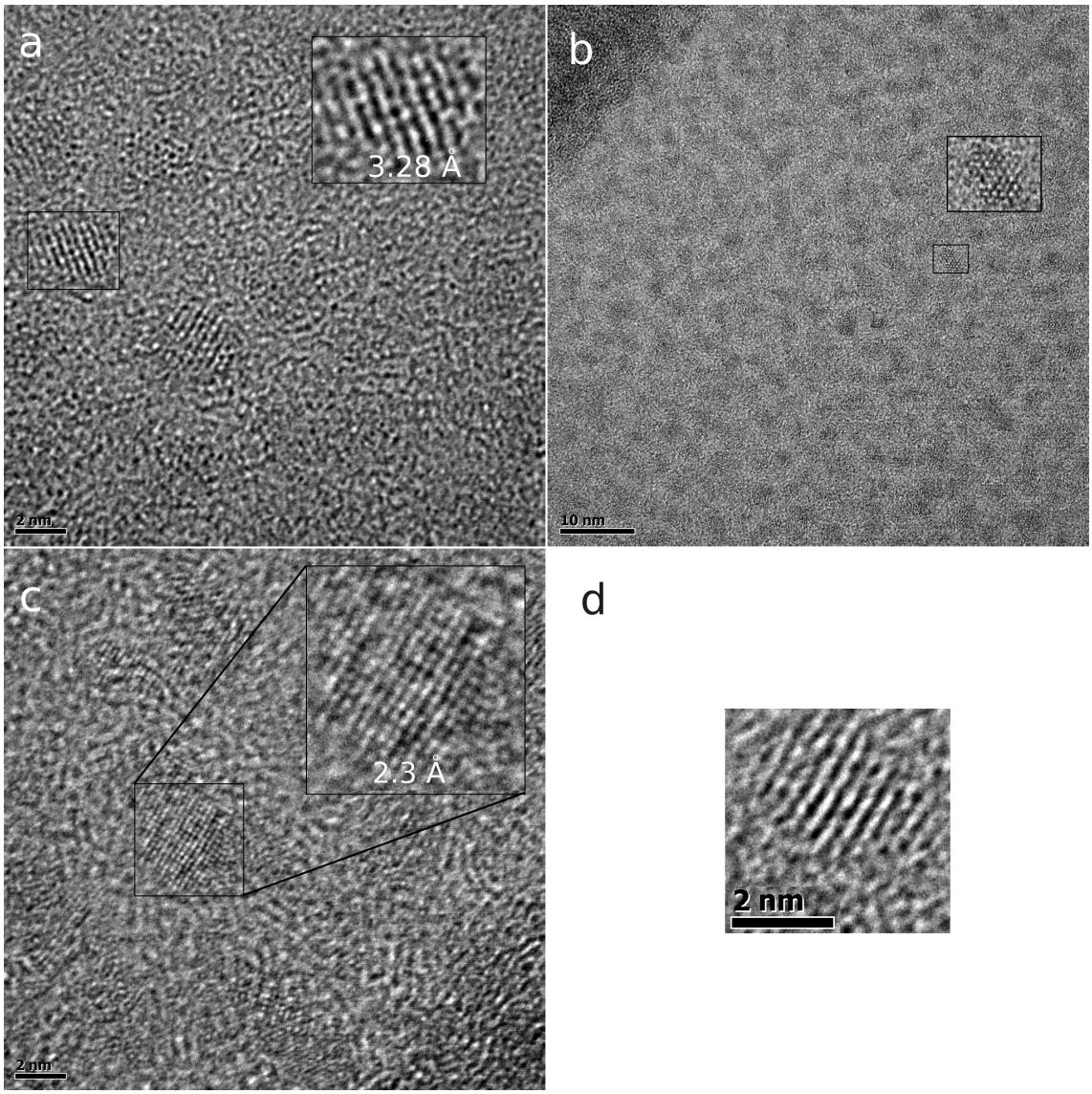

Figure 2.20: Compilation of images from sample 19 in Table 2.1. Lattice fringes can be seen in several images, indicating a crystalline bulk, even if some lattice fringes contain a small amount of disorder. Black numbers are associated with nearby scale bars, and white numbers are lattice spacings.

2.3.7 Spectral Analysis of Ultrafast Results

Sample	Peak of Interest	Center	Area	Width	Height	R^2
25:1 Sample	Cation Radical	1.95 eV	2.43e-04 eV	0.194 eV	0.997 Δ mOD	0.993
	T_1	2.10 eV	6.60-e04 eV	0.457 eV	1.15 Δ mOD	
2:1 Dye:NP	Cation Radical	1.97 eV	5.80e-04 eV	0.114 eV	4.08 Δ mOD	0.992
	T_1	2.10 eV	1.32e-03 eV	0.391 eV	2.70 Δ mOD	

Table 2.3: Details of deconvolutions found in Figures 2.21 and 2.22

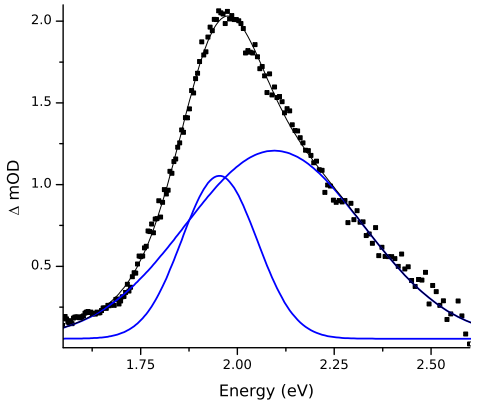

Figure 2.21: The 25:1 sample's spectrum in the pump-probe experiment at 500 ps, deconvoluted to reveal the signal from the triplet and the cation radical.

Deconvolutions of pump-probe spectra with long delay times (500 ps probe delay) are shown in Figures 2.21 and 2.22. Table 2.3 shows the position and size of each component Gaussian after samples are scaled for the initial height of the S_1 peak. It is apparent from this data that the concentration quenching pathway reduces both the triplet (T_1) intensity and the cation radical intensity at long probe delay times. Even though the intensities are scaled to make the initial singlet (S_1) signal's intensity equal, the 2:1 sample has almost double the intensity (by area) in its cation radical and T_1 peaks.

The presence of the cation radical signal in the 25:1 sample is notable. Neither the slice at 1.70 eV nor the slice at 1.97 eV required a ∼15 ps component exponential, which

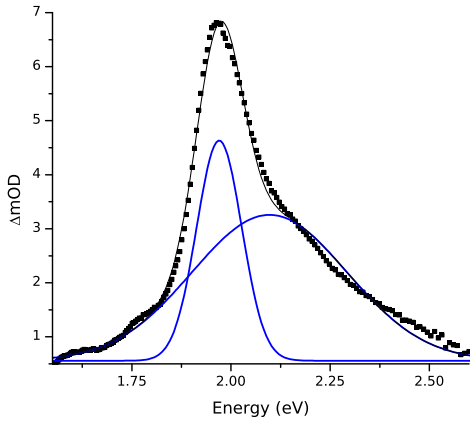

Figure 2.22: The 2:1 sample's spectrum in the pump-probe experiment at 500 ps, deconvoluted to reveal the signal from the triplet and the cation radical.

would be indicative of an electron transfer pathway, to fit the decays at these energies. As mentioned above, this is likely a result of the concentration quenching pathway overwhelming the electron transfer pathway as the processes compete to quench the S_1 state. The deconvolutions do not produce conclusive evidence that the cation radical signal is present, but the peak position is characteristic of it. This leads to the conclusion that the 25:1 sample and other samples near this ratio contain some electron transfer component, even if it is overwhelmed by the concentration quenching pathway and is only a minor contribution to the S_1 decay.

According to simple kinetic theory,[130] if the concentration quenching and electron transfer pathways are in direct competition with each other, the 1 ps rate of concentration quenching should far outpace the 15 ps electron transfer process:

$$\Phi_{\mathrm{ET}} = \frac{\frac{1}{15\mathrm{ps}}}{\frac{1}{15\mathrm{ps}}\frac{1}{1\mathrm{ps}}} = 0.0625 \tag{2.1}$$

$$\Phi_{\mathrm{CQ}} = \frac{\frac{1}{1\mathrm{ps}}}{\frac{1}{15\mathrm{ps}}\frac{1}{1\mathrm{ps}}} = 93.75 \tag{2.2}$$

As seen in Eqs. 2.1 and 2.2, the theoretical quantum yields for lifetimes of processes more than an order of magnitude apart means that the faster process is responsible for

more than 90% of the S_1 state dissipation. Using the same analysis, it can be predicted that if the inter-system crossing (ISC) pathway was in direct competition with either of the two faster processes discussed here, the ISC event would be barely noticeable:

$$\Phi_{\mathrm{ISC}} = \frac{\frac{1}{500\mathrm{ps}}}{\frac{1}{15\mathrm{ps}}\frac{1}{500\mathrm{ps}}} = 0.0291 \tag{2.3}$$

Eq. 2.3 shows that the quantum yield of the ISC pathway would be less than 3% of the population of the excited state.

Thus the final question surrounding the ultrafast spectroscopic data regards the continued presence of the T_1 signal when there should be none left. ISC is a much slower process than electron injection and "contact dimer" mediated concentration quenching, meaning there should be no more T_1 signal once the signals from unattached dyes have disappeared in the NMR and IR (at P_t). The persistence of the ISC process past P_t can be assigned to the fact that there are surface sites with differing properties on the nanoparticle.[102,131] Specifically, it is likely that there are exchange sites on the surface that are not conducive to electron injection or concentration quenching, and that dyes adsorbed here have only a non-radiative pathway or fluorescing pathway. This possibility is discussed in the next section.

2.4 Discussion

2.4.1 NMR Analysis

The difference in the ^{1}H NMR spectrum between bound and unbound signals, gives us an ability to ascertain if a molecule has attached using a standard 1D NMR experiment. The explanation for this phenomenon of spectral broadening upon attachment to a large, slowly rotating object is still a subject of debate. It has been proposed that this broadening is due to hindered motion of the dye. Specifically, this hindered motion will not allow the coupling terms D_{ij} (Eq. 2.4) that are dependent on the angle, θ, between the internuclear vector and the applied field to average to zero, as it would do in a freely tumbling molecule. This means coupling constants that formerly averaged to zero upon fast tumbling will no longer do so, but rather form a distribution of coupling constants centered about zero that will split a coupled proton's signal. This smearing of the peak

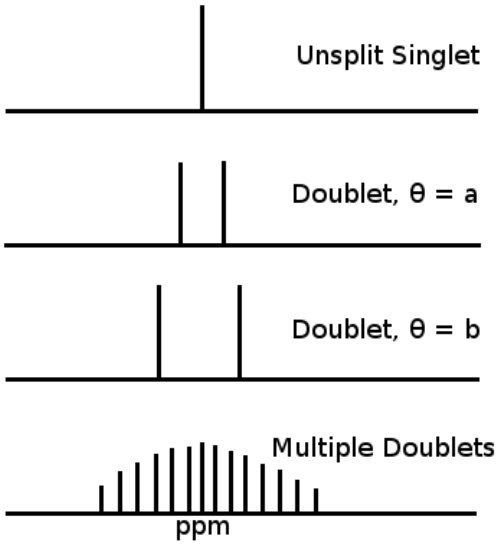

Figure 2.23: A rough NMR schematic showing increments of residual dipolar coupling's broadening of a singlet, into a doublet of certain splitting, and into a different doublet of larger splitting due to a different θ between the interdipole axis and the NMR's permanent field, and then the sum total of several different dipolar splittings. Note in the bottom scheme, the height of each peak roughly corresponds to the number of peaks observed at a certain shift.

intensity will broaden the peak, potentially into the background in the case of highly hindered protons (Fig. 2.23).[132,133] It is important to note that these residual dipole couplings are quite possibly intermolecular couplings.

$$D_{ij} = \frac{\hbar\gamma_i\gamma_j}{4\pi r_{ij}^3}[1 - 3\cos^2\theta] \tag{2.4}$$

Support for this hypothesis has been put forth by several authors. Particularly, Zhou, *et al.* have shown that by spinning a dispersion-phase sample at the magic angle at roughly 2-3 kHz it is possible to recover some of the peak sharpness that was lost when a molecule attached to a large particle.[128]

There is also evidence supporting a competing theory that states the broadening is due to the heterogeneity of the surface of attachment. Kohlmann *et al.*, Badia *et al.*, and Zelakiewicz *et al.* point to the asymmetry of the broadening mechanism to indicate the

previous mechanism is not sufficient to describe all broadening events [125–127]. Their studies seem to show that a molecule attached to the surface of a nanoparticle will have a varying amount of spectral broadening depending on the difference in properties of the surface attachment sites. Backing away from this minor controversy however, there is agreement that attachment to a given particle, protein, or surface will result in signal broadening.

For this study, it is important to note that while aliphatic (*e.g.* alkylthiol) nuclides lose any information regarding binding after a few bonds from the binding group [125–127], the rigidity of the terthiophene moiety makes this portion of **1-CO_2H** sensitive to attachment. The steric barrier to planarity across the thiophene-phenyl bond reduces the probability of coplanarity between these two rings, which allows the phenyl ring more freedom to sample conformational space. This is what is seen experimentally, where in figure 2.8 the phenyl protons' signals recover more than terthiophene signals. The spectrum of sample 19 shows that at low ratios of **1-CO_2H**:nc-CdS the phenyl ring spins freely, but at P_t, the phenyl ring seems to be locked into position.

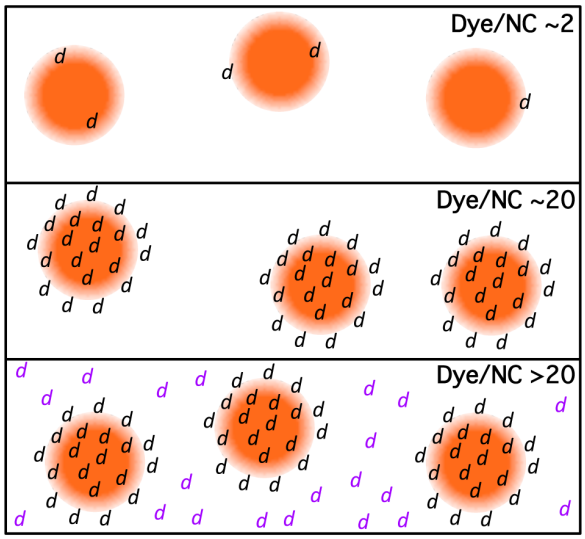

Figure 2.24: Schematic showing the nature of the species present at different dye/NC ratios. The NC bound dye (d) molecules are shown in black, whereas the free dyes are shown in purple.

Figure 2.24 illustrates schematically the structures present in solution as a function

of the dye to nanocrystal ratio, which is in reverse order of the Stern-Volmer experiments in previous sections. At low ratios nearly all of the dyes will be coordinated to nanocrystals. If we were able to examine individual nanocrystals, we would expect to find a distribution of dye to NC values around the nominal concentration ratio. In this stage, the ^{1}H NMR resonances of the dye are broadened, due to slow tumbling of the dye/NC dyad, but observable, especially in the phenyl region as mentioned above. As the dye:NC ratio increases, the dyes become more crowded on the surface resulting in additional steric hindrance causing further broadening of the ^{1}H NMR resonances. This progresses until the dye:NC ratio reaches 20 at which point the NMR spectrum shows no discernible peaks. At still higher ratios, sharp hydrogen resonances appear due to unbound **1-CO$_2$H**.

Given the CdS NC diameter of 2.5 nm used throughout this study, the 20:1 ratio suggests that at saturation each dye occupies $\sim$1 nm^2 of surface area. This is slightly more than twice the area/dye found when **1-CO$_2$H** saturates the surface of ZnO NCs.[121] The larger value observed for the **1-CO$_2$**/CdS dyads is similar to the results reported by Sachleben et al. on thiophenol bound to CdS NCs in which the effective thiophenol radius was between 2 to 3 times larger than the van der Waals radius of the ligand bound in a terminal fashion. Returning to the comparison with the **1-CO$_2$**/ZnO system, it is likely that an important contributor to this difference is that the CdS NCs were initially capped with oleate, whereas the ZnO NCs were capped with acetate. In neither case do we have an independent measure of the number of oleates or acetates that remain bound to the NC when the dye coverage reaches saturation.

Near a CdS NC concentration of 0.2 mM where the NMR spectra indicate that all dyes are bound (dye:NC $\sim$20, at P_t), the Stern Volmer graph (Figure 2.13) indicates a maximum in static quenching efficiency. While both trends rely on the intermolecular interactions of the dyes on the CdS NC surface, we do not necessarily expect that they overlap because the mechanisms impacting the fluorescence quenching and the NMR line broadening differ. The value of I_0/I for fluorescence quenching reaches a maximum of only 8 indicating $\sim$13% of the bound dyes are not quenched. The time resolved results agree well with the time integrated quenching experiments and offer additional insight into the dynamics. At a dye:NC ratio of 25:1, near the maximum in the Stern Volmer quenching experiments, 10% of the dyes decay with a lifetime of 485 ps indicating that

a residual population of dye relaxes via the same mechanism found in the absence of NCs. The observation that they do not have exactly the same lifetime as the free dye or dyes bound at lower coverages is not surprising given that the dyes local environment is a strong function of coverage. One possible explanation for the existence of this minor component is that the dye is bound to an inactive site. For instance it could be bound to a cadmium ion, perhaps at one of the vertices, that itself is only weakly coupled to the electronic structure of the CdS NC core. From basic geometric considerations, such a dye location could also result in reduced coupling with neighboring dye molecules.

At a dye:NC ratio of 2:1, Figure 2.18c shows a strong absorption gain from the radical cation at 1.97 eV providing evidence that the quenching process is due to electron transfer to the CdS NC. The time resolved changes establish a decay time for electron transfer of 16 ps. The 16 ps decay in the excited state of the dye measured at 1.70 eV is correlated, within error, with the 13 ps rise of the radical cation (Table 2.2). As a result, we assign this component of the excited state quenching to electron transfer. We note that the possibility of energy transfer from the bound dye to CdS NCs in a FRET process is small due to the lack of spectral overlap between the dye fluorescence and the CdS NC absorption.

In previous studies on the excited state electron transfer in **1-CO$_2$**/ZnO NC dyads, the excited state energy of the dye was ∼1.3 eV above the ZnO NC conduction band edge.[120,121] In CdS NCs the acceptor energy is higher than in ZnO due to the combined impact of higher electron affinity of the bulk material and the greater sensitivity of CdS to the effects of quantum confinement. The estimated energy of the excited state of **1-CO$_2$H** is -3 eV relative to vacuum. For bulk CdS the position of the conduction band minimum is -3.7 eV relative to vacuum.[123] For a 2.5 nm diameter CdS NC estimates for the Se state range from -3.3 to -3.0 eV.[134] At this small diameter the effective mass approximation overestimates the NC band gap, while the tight binding models tend to underestimate it.[134] This reduces the driving force of electron transfer to a few tenths of an eV, a value that is close to that expected for the reorganization energy. Assuming that -ΔG° and λ are approximately 0.2 eV, we can use the Marcus equation for weakly coupled, diabatic electron transfer to estimate that the electronic coupling for the barrierless transfer is on the order of 10 cm^{-1}. The energetics of this dye/NC system suggest that the electron transfer rate should be sensitive to the NC

diameter.

In our study of **1-CO_2H** bound to ZnO NCs, it was reported that the ultrafast measurements exhibited a ∼3.5 ps electron transfer event at all dye:NC ratios.[120,121] While the dye was the same as used in the current study, the dyads differed by the nature of the semiconducting nanocrystals (CdS vs. ZnO), the surface capping group (the long hydrocarbon chains of oleate groups bound to CdS vs. acetate bound to ZnO) and the solvent (methylene chloride in the CdS study vs. ethanol in the ZnO work). Future experiments are aimed at probing the impact of nanocrystal size on electron transfer rates.

2.4.2 The Quenching Mechanism at High Coverage

When the dye:NC ratio is increased to 25:1, near the maximum in the Stern Volmer quenching experiments, we observe a dominant accelerated singlet decay time of 1 ps and a diminished signal corresponding to the radical cation. Based on the combined evidence presented, the simplest explanation for the additional quenching mechanism observed at high coverage is concentration quenching.[110,135–138] This refers to intermolecular electronic interaction between dye molecules at the surface that results in substantial enhancement in the non-radiative relaxation rate (via internal conversion, IC). The type of strong electronic coupling that would be associated with such a dramatic perturbation of the IC rate can be expected to alter the absorption spectrum. Figure 2.17 shows that despite a blue shift in λ max caused by the addition of NCs, the FWHM increases leading to more absorption on the low energy side of the absorption band. The trend is followed monotonically as the concentration of the NCs is increased to the point where the dye:NC ratio is ∼20:1 at which point nearly all of the dye has been bound to the NCs. Further increase in the NC concentration results in narrowing of the absorption along with appearance of an isosbestic point at 450 nm. We suggest that this narrowing and, ultimately, the appearance of the isosbestic point is due to conversion of a NC surface saturated with dyes to one in which the dyes are isolated. The small magnitude of the change in the absorption spectra could be due to a limited number of dye-dye interactions that actually perturb the electronic spectrum and lead to an enhanced IC rate. It has been previously suggested that significant intermolecular interaction between surface bound dyes, basically dimer formation, is limited to a

minority of dyes on the surface, and this minority acts as an energy sink subsequent to energy transfer.[139,140] In such a scenario, the accelerated time scale that we observe would reflect energy transfer to this sink. Nakashima et al. have proposed this contact dimer quenching mechanism in monolayers of rhodamine B on the surface of organic crystals.[138]

Fluorescence quenching of oligothiophene chromophores has been reported to occur using nanoparticles of TiO_2 [113,115], CdSe [122], CdS [116] and ZnO. [120,121] Only in the ZnO studies did ultrafast pump-probe measurements directly establish the appearance of the transient absorption of the oxidized dye thereby confirming electron transfer as a quenching mechanism. In the current study, the appearance of the oxidized dye was observed using ultrafast methods, however, at high coverage of dye molecules the rate of concentration quenching exceeded that of electron transfer. Given the widespread use of oligothiophenes in photovoltaics, and the detrimental effect that concentration quenching has on light-to-electricity conversion efficiency,[141–144] rational dye design becomes an important consideration. Complicating the picture further is the fact that other groups have shown that certain aggregates not only participate in electron transfer, but also absorb a greater fraction of the solar spectrum due to aggregation-induced changes in their absorption spectra.[145–148] To take advantage of aggregation as a benefit rather than a drawback, it will be necessary to study further the factors that affect the relative rates of electron transfer and energy dissipation in a variety of dyes.

2.5 Conclusion

A combination of techniques (IR, ^{1}H NMR, electronic absorption and emission spectroscopies) established the terthiophene-based fluorophore, **1-CO_2H**, binds to CdS NCs by attachment of the carboxylate anion to cadmium cations on the NCs. For the 2.5 nm diameter particles the maximum number of dyes that could be bound to the NC was approximately 20. The NC-dye binding results in quenching of the dye. When the dye:NC ratio is low, ultrafast pump-probe measurements show the disappearance of the singlet excited state with concomitant formation of the oxidized dye. This electron transfer quenching mechanism exhibits a characteristic lifetime of 16 ps. As the ratio of the dye to NC increases the spectroscopic signature of the oxidized dye becomes less

prominent and a decay mechanism with a decay time of 1 ps ensues. This faster decay is assigned to concentration quenching which is enabled by the high concentration of dye molecules on the NC surface. The current work illustrates that concentration quenching can occur on an ultrafast time scale and that care must be taken in assigning quenching mechanisms.

Chapter 3

Investigation of Concentration Quenching Processes in Various Dyes on Nanocrystal Surfaces

In the previous chapter we have provided evidence that concentration quenching (CQ), a process that rapidly dissipates energy away from aggregated dye excited states, is active in dyads of **1-CO_2H** and nanocrystalline CdS (nc-CdS). The mechanisms underlying this process have been only briefly studied, in spite of CQ's importance in dye-sensitized solar cells (DSSCs) and bulk-heterojunction solar cells. Here we attempt to bring to light more details of the physics behind the CQ process. In addition, we provide evidence that CQ could be more prominent than originally thought.

3.1 Introduction

Concentration quenching (CQ),[110,135–138,149–151] also referred to as self-quenching when in the solution phase,[152–154] is characterized by a reduction in the fluorescence quantum yield (Φ_{Fl}) as concentrations of fluorophores are increased. This paradoxically inverse relationship between concentration of fluorophores and luminescence intensity results from formation of fluorophore aggregates which are able to absorb a virtual photon from a monomeric fluorophore.[151] After a critical concentration of fluorophores is reached (similar to the CMC in surfactant research), aggregates start forming readily and further increases in the concentrations serve to increase their numbers. In the case of molecules whose absorption spectra undergo a red-shift upon aggregation, FRET from a monomeric fluorophore to an aggregate is an exo-energic process as the virtual photon created in the monomeric fluorophore will fluoresce at an energy high enough to excite the aggregate.[151] Thus a higher concentration of fluorophore will lead to a reduction in the luminescence intensity of the solution, as well as some related spectral changes that will be discussed in this chapter.

In our case, the concentration in which we are observing an increase is the surface concentration of the dye molecules that we are adsorbing to the various nanoparticle surfaces. Surface-templated aggregation that is observed upon increases in the surface concentration of dye molecules is expected to be more probable than solution-phase aggregation. This is because the aggregating dyes' attachment to the same nanoparticle makes the surface-templated process of aggregation an intramolecular one.

After dye molecules undergo a surface-templated aggregation event, evidence of the aggregation can be observed in both the ^{1}H-NMR spectrum (Figure 2.8) and the UV-Vis spectrum (Figure 2.17). Both of these spectroscopies are detecting the $\pi - \pi$ stacking motifs that are found in the surface-templated aggregates. Attempts to break up $\pi - \pi$ stacking on nanoparticle surfaces have been made before with significant results.[27,155]

At the beginning of this chapter we address some basic considerations about CQ, and then go on to describe studies modifying the surface of the nanoparticles both before and after the terthiophene dye (**1-CO$_2$H**) is added to the nanoparticle dispersion. Depending on the modifying molecule, the dye molecules may fluoresce with a lower intensity, a higher intensity, or be unchanged. If the dye aggregates are broken up on

the surface of the nanoparticle, we would expect the dye molecules to fluoresce more strongly as a result of the CQ pathway being removed. This may also be accompanied by an increase in the electron transfer reaction yield. If aggregates containing dyes are created where none existed previously, the reverse is expected.

In the middle of this chapter until the conclusion we analyze areas where CQ is unexpectedly found. The conclusion incorporates these studies to build a more complete picture of the prevalence of CQ, as well as some idea of how the unexpected areas in which CQ is found require us to modify our thoughts on CQ's mechanisms.

In these studies, CQ is best analyzed spectroscopically by fluorescence techniques, the results from which are frequently portrayed as Stern-Volmer plots (I_o/I versus concentration of quencher) and fit to Equation 3.1,

$$\frac{I_o}{I} = K_{SV}[Q] + 1 \tag{3.1}$$

where K_{SV} represents the Stern-Volmer constant of association and $[Q]$ represents the concentration of the quencher. The Stern-Volmer model generally implies a single mechanism for luminescence quenching (i.e. ET or CQ), but in our research we have frequently found two mechanisms operating simultaneously. In Appendix A, we provide a derivation for a Stern-Volmer model where there are two mechanisms at work at once, which produces the simply-formed result in Equation 3.2,

$$\frac{I_o}{I} = K_{S1}[Q_1] + K_{S2}[Q_2] + 1 \tag{3.2}$$

where K_{S1} and K_{S2} here represent the Stern-Volmer constants of association for quencher 1 and 2, respectively, and $[Q_1]$ and $[Q_2]$ represent the concentrations of each quencher. While the two-component Stern-Volmer model does not appear in this chapter after the Introduction, its relevance to the studies of systems in which CQ operates alongside ET merits inclusion of reference to it into this chapter.

3.2 Experimental

Cadmium oxide (99.999 atom % Cd) was obtained from Strem Chemicals; oleic acid and dichloromethane were obtained from Fisher Chemicals; sulfur (USP grade) was obtained from JT Baker; hexanes (spectroscopy grade), dichloromethane-D_2 (99.9 %

D atom), and octadecene (90%) were obtained from Sigma Aldrich and used without further purification. Hexylamine (99%) was obtained from Sigma Aldrich and distilled once over CaH_2 before use.

The terthiophene dye, 3',4'-dibutyl-5"-phenyl-[2,2':5',2"-terthiophene]-5-carboxylic acid (**1-CO_2H**) was synthesized by the reported method.[120]

CdS nanoparticles were synthesized as previously reported[156] and we note that these oleate-capped CdS particles are referred to below as nc-CdS. The nc-CdS dispersion in CH_2Cl_2 contained particles of 2.5 nm diameter on average.

Hexylamine-capped ZnO particles were synthesized by the method reported earlier[157], and are referred to below as nc-ZnO. In the experiments reported here, the sample of nc-ZnO had an inflection point in the UV-Vis at 359.4 nm and a concentration of 1.1 $\times 10^{-5}$ M. The average size of the ZnO nanoparticles in dispersion phase was 4.7 nm, based on the empirically created fit of sizes to the inflection point data provided by Sarma et al.[106] The dispersion containing nc-ZnO in hexanes was used as a stock solution in the experiments below.

Acetate-capped ZnO particles were synthesized by the method reported earlier[121], and are referred to below as ac-ZnO. For the lone experiment with ac-ZnO, the concentration of the dispersion was 1.35 $\times 10^{-4}$ M, and the nanoparticles were 3 nm on average. The dispersion containing ac-ZnO in ethanol was used as a stock solution in the experiment below.

For NMR studies of nc-CdS and nc-ZnO, the solvent used was CD_2Cl_2, and in the case of ac-ZnO, the solvent used was CD_3OD.

The steady-state emission spectra were recorded through two Spex Fluorolog 1680 0.22 m double spectrometer gratings equipped with a 450 W xenon source. All spectroscopy was performed in quartz cuvettes with a 3 mm path length in CD_2Cl_2 unless otherwise noted. ^{1}H NMR spectra were recorded on a 500 MHz Varian Inova with the standard 1D ^{1}H pulse sequence at a gain of 60 dB and 256 transients per spectrum. UV-Vis spectra were recorded using a DH 2000 BAL Mikropack deuterium/halogen source and an Ocean Optics USB4000 detector. IR spectra were measured on specimens drop cast from solution onto a NaCl plate and dried under a stream of $N_{2(g)}$. A Thermo Nicolet 670 FTIR was used with each spectrum comprising 128 scans.

3.3 Results and Discussion

A critical, but elementary experiment related to this study is the measurement of luminescence intensity as concentration of fluorophore is increased. In the case of a planar dye like **1-CO$_2$H** the result is almost immediately apparent — an inverse correlation between concentration of fluorophore and luminescence intensity should be observed. The experiment was performed to confirm this hypothesis, and Figure 3.1 shows that the dye molecules indeed fluoresce less at higher concentrations.

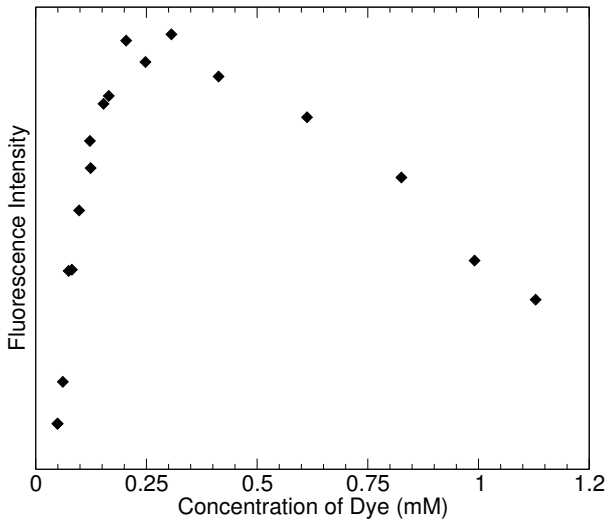

Figure 3.1: Fluorescence intensity of **1-CO$_2$H** dye measured in front-face mode as concentration of **1-CO$_2$H** dye is increased in CH_2Cl_2.

A valid concern regarding the above data is that the divergence of the plot in Figure 3.1 from linearity may not be a result of aggregation-induced self quenching. One possibility is that the beam from the fluorimeter does not penetrate the sample uniformly across the range of concentrations, and this means that different portions of the sample are being excited at different concentrations. Combine this with the possibility that the optics guiding emitted photons into the detector can be similarly position-dependent, and one can observe a non-linear plot of luminescence intensity versus concentration of fluorophore simply as a result of the experimental setup. While it is known that the instrumental setup that was used in this case contributes non-linearities to the

aforementioned plot, Figure 3.2 shows that the point at which the slope of the plot in Figure 3.1 starts to reduce correlates with a red-shift of the luminescence peak. This is indicative of a connection between the reduction in the luminescence intensity and the introduction of a red-shift, which is commonly associated with aggregation. Thus, solution-phase self-quenching is active in solutions of **1-CO_2H** in CH_2Cl_2 at concentrations higher than 2.0 $\times 10^{-4}$ M.

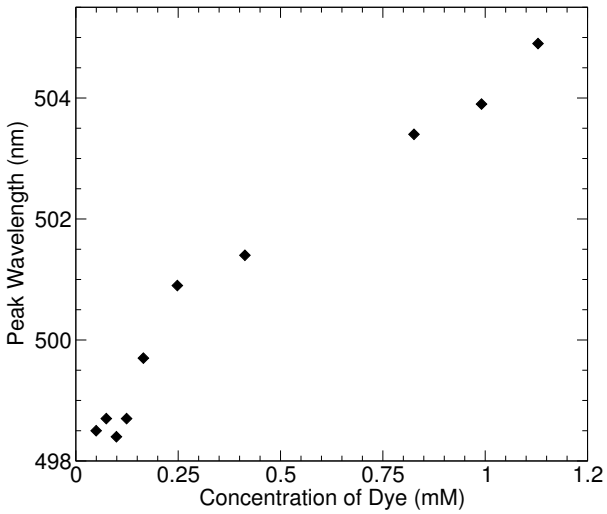

Figure 3.2: Correlation between the concentration of the **1-CO_2H** dye molecules in CH_2Cl_2 and the amount of red-shift observed in the peak position. It can be seen that the onset of the red-shift is roughly aligned with the divergence of the plot in Figure 3.1 from linearity.

3.3.1 Carboxylic Ligand Exchange and Co-adsorption Studies

Similar to the use of chenodeoxycholic acid on the surface of nanoparticles in DSSC applications,[155,158,159] we have performed experiments coadsorbing various carboxylic acid-containing molecules along with **1-CO_2H** onto the nc-CdS surface. However, in our experiments we do not try to disrupt molecular aggregate formation, but rather we try to artificially create concentration quenching pathways. Clearly if one can turn on the process at will, the reverse is also true. Figure 3.3 shows the carboxylic acid-containing

molecules that we have used in efforts to reproduce the concentration quenching environment.

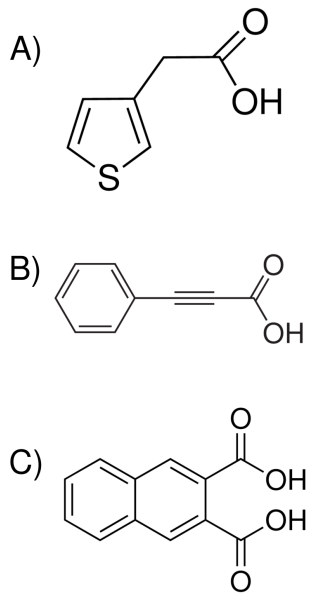

Figure 3.3: Various carboxylic acid-containing molecules that have been coadsorbed to nc-CdS along with **1-CO_2H**. A) corresponds to 3-thiophene acetic acid, B) corresponds to phenyl propiolic acid, and C) corresponds to 1,2-naphthalene dicarboxylic acid.

3-Thiophene Acetic Acid

Figure 3.4 shows that 3-thiophene acetic acid (3-TAA) can indeed attach to the surface of nc-CdS even though the surface is expected to be saturated by oleate molecules. Figure 3.4 also shows that the 3-TAA molecules do not desorb **1-CO_2H** already on the surface of the nc-CdS. This can be seen from the peak in Figure 3.4 at 7.6 ppm that corresponds to a phenyl proton on **1-CO_2H**. This peak is unchanged from the sample containing **1-CO_2H** and nc-CdS in a 1:1 ratio (second-to-bottom) all the way to the sample containing 3-TAA, **1-CO_2H**, and nc-CdS in a 20:1:1 ratio.

Similar to the work that has been done before[156] wherein **1-CO_2H** displaces oleate from the surface, Figure 3.6 shows increasing amounts of 3-TAA correlate with larger carboxylic acid stretches at 1712 cm^{-1} which has been previously assigned to oleic acid.

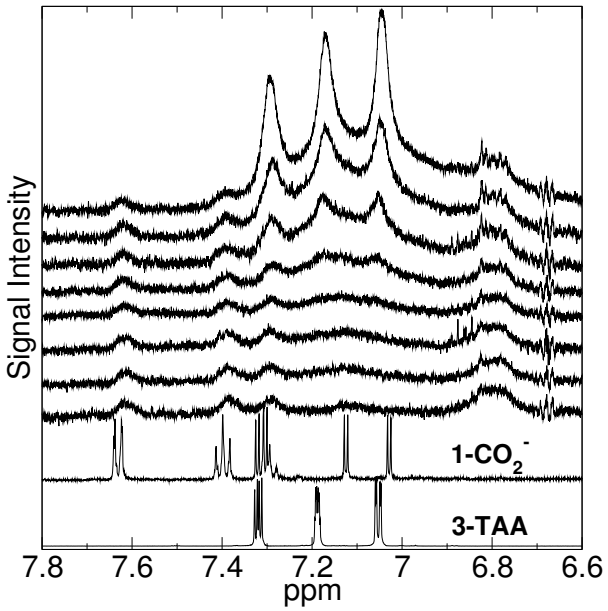

Figure 3.4: NMR of a series of mixtures with increasing concentrations of 3-TAA from bottom to top. The bottom spectrum is pure 3-TAA in a concentrated sample alone, and the next spectrum up is of the deprotonated salt, **1-CO$_2^-$**. The next lowest spectrum is a 1:1 mixture of **1-CO$_2$H** and nc-CdS. Going higher from this spectrum is a 1:1:1 mixture of 3-TAA, **1-CO$_2$H**, and nc-CdS, a 2.5:1:1 mixture, a 5:1:1 mixture, a 7.5:1:1 mixture, a 10:1:1 mixture, and a 20:1:1 mixture of the same.

It is not clear why the oleate is selectively displaced and **1-CO$_2$H** is not affected by the presence of 3-TAA. One explanation is that the oleate molecule is quite flimsy and therefore releasing this molecule into solution from the surface of a nanoparticle results in a large gain in entropy. We have noted before that the differences in K_a values between **1-CO$_2$H** and oleic acid could make **1-CO$_2^-$** anion a more stable adsorbate than would be oleate. However, this is not a conclusive argument.

Photoluminescence spectroscopy (PL) was carried out on the same samples as with the IR and NMR samples above. Figure 3.7 shows that the presence of 3-TAA strongly perturbs the emission of **1-CO$_2$H**. Even a small amount of 3-TAA is capable of reducing the luminescence intensity of **1-CO$_2$H**, and the sample with a 20:1:1 ratio of 3-TAA to

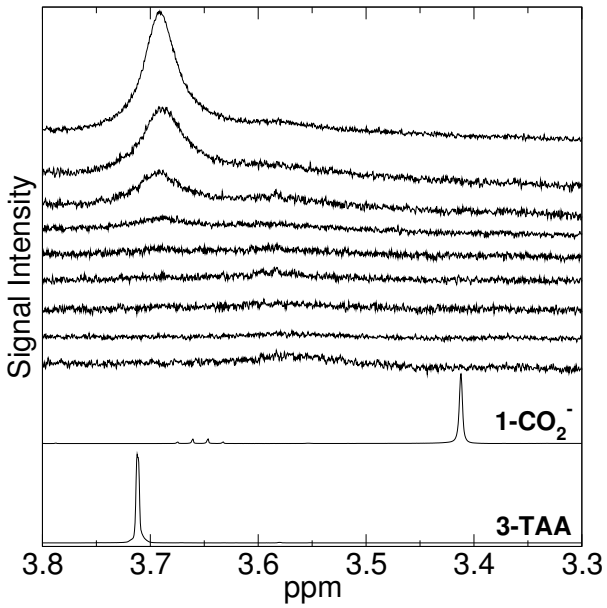

Figure 3.5: The spectra from Figure 3.4 are shown with a different region highlighted. The bottom spectrum is pure 3-TAA in a concentrated sample alone, and the next spectrum up is of the deprotonated salt, **1-CO$_2^-$**. The next lowest spectrum is a 1:1 mixture of **1-CO$_2$H** and nc-CdS. Going higher from this spectrum is a 1:1:1 mixture of 3-TAA, **1-CO$_2$H**, and nc-CdS, a 2.5:1:1 mixture, a 5:1:1 mixture, a 7.5:1:1 mixture, a 10:1:1 mixture, and a 20:1:1 mixture of the same.

1-CO$_2$H to nc-CdS fluoresces at less than half the intensity as does the 1:1 **1-CO$_2$H**/nc-CdS sample.

The spectral changes that accompany the diminution of fluorescence intensity are also instructive. Examining the sample containing an equimolar ratio of **1-CO$_2$H** and nc-CdS, we can see a peak in the spectrum that is nearly-flat but with a slightly positive slope when plotted in wavelength units. As mentioned in the previous chapter (Figure 2.15), this spectrum is reminiscent of the vibrational progression seen in the deprotonated spectrum, but which is not seen in protonated **1-CO$_2$H**. For reasons that we are not able to explain, previous experiments[156] show the vibrational progression only appears when the dye molecules become more isolated from one another on the surface of the nanoparticles. We are able to not only reduce the fluorescence intensity, but the

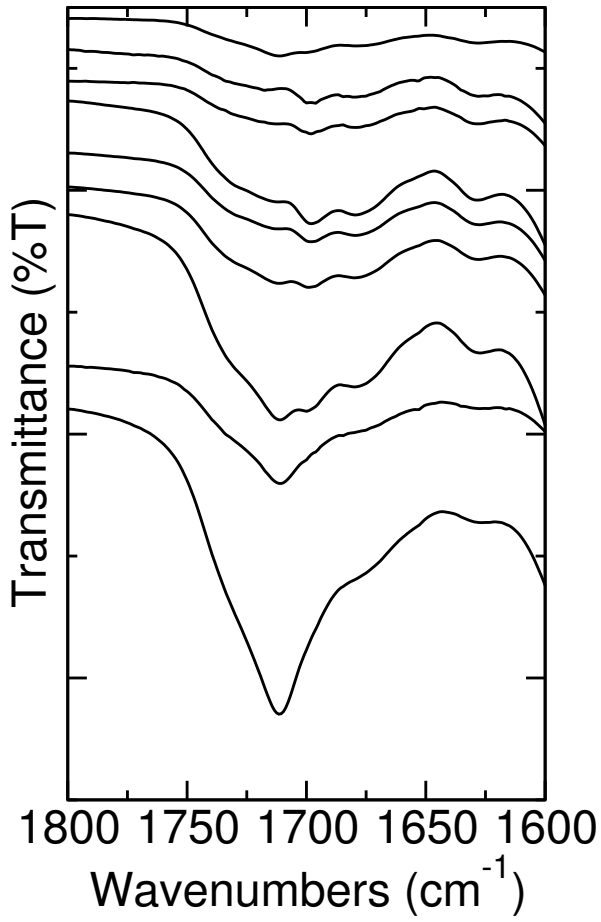

Figure 3.6: IR showing the C=O region of the spectrum. The top spectrum is the nanoparticle alone, then the 1:1 Dye:nc-CdS. Going downwards increases amount of 3-TAA. The peak growing in is the oleic acid peak. This is indicative of the fact that 3-TAA is displacing oleate.

luminescence spectrum also resembles the surface-saturated spectrum where concentration quenching is active. This seems to support our claims that we have reproduced the concentration quenching effect even though **1-CO_2H** adsorbs to the surface at ratios of roughly one **1-CO_2H** molecule per nc-CdS.

Another important piece of information that we can take from the above data is that the oleate molecules that are ejected from the surface by 3-TAA are neighbors of

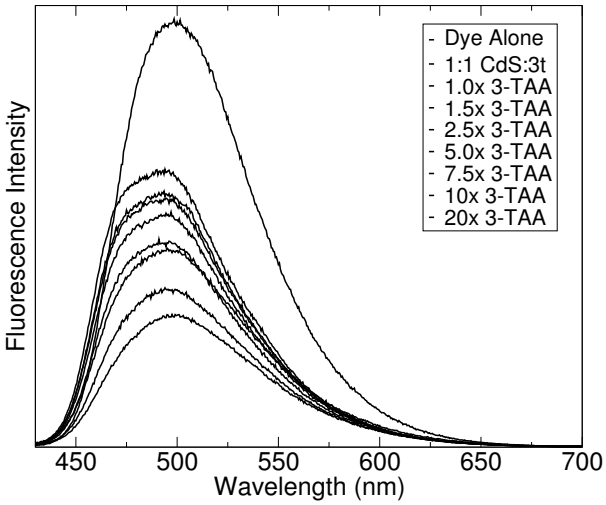

Figure 3.7: PL of the series of mixtures listed in the legend. Dye alone is the top spectrum, followed by the next highest which is **1-CO_2H** and nc-CdS in equimolar amounts. This latter mixture is replicated and increasing amounts of 3-TAA are added until a ratio of 20:1:1 3-TAA:**1-CO_2H**:nc-CdS is reached at the lowest spectrum.

the **1-CO_2H** on the surface of nc-CdS. We conclude this because in an ordinary place-exchange reaction where one 3-TAA molecule displaces one oleate molecule (which leaves as a neutral oleic acid molecule) 3-TAA will occupy the same location on the surface as did the oleate. From Figure 3.6, we can see 3-TAA liberating oleic acid from the surface of nc-CdS. As noted above, the sharpened peak for the sample with the highest concentration of 3-TAA in Figure 3.7 means that **1-CO_2H** on the surface is no longer isolated. Thus the increased concentrations of 3-TAA resulted in replacement of the oleates on the surface, and the spectral changes seen in the PL suggest that 3-TAA is mostly next to **1-CO_2H**. Gathering information on ligand replacement reactions is quite difficult because of the amorphous nature of most nanocrystalline surfaces, but in this case it seems that we are able to show that the ligands being replaced are on facets and not on vertices or edges.

Phenyl Propiolic Acid

Phenyl propiolic acid (PPA) was used in a similar fashion as was 3-TAA. Figure 3.8 shows the IR spectra of a series of mixtures of **1-CO_2H**, nc-CdS and PPA. The top spectrum shows the sample containing an equimolar mixture of **1-CO_2H** and nc-CdS. The next highest spectrum in the figure is a sample containing equimolar amounts of **1-CO_2H**, nc-CdS, and PPA. The signal at 2218 cm^{-1} and its shoulder at 2178 cm^{-1} are the C≡C stretching frequencies from PPA, and the correlation of these signals with the oleic acid C=O stretching frequency at 1712 cm^{-1} means that as the concentration of PPA in solution increases, so too does the amount of free oleic acid. The peak positions of the C≡C stretches do not correlate with any previously reported positions for the C≡C stretch in the PPA molecule alone, including as it is prepared in a KBr pellet (FT-IR: 2204 cm^{-1} and 2238 cm^{-1}), a nujol mull (FT-IR: 2203 cm^{-1} and 2237 cm^{-1}), a CCl_4 solution (FT-IR: 2207 cm^{-1}), or a powder (Raman: 2209 cm^{-1} and 2243 cm^{-1}). The shift of the stretching frequencies to lower energies by ∼20 cm^{-1} leads us to believe that the 2218 cm^{-1} and 2178 cm^{-1} C≡C stretching modes can be assigned to a PPA molecule that is bound to the nc-CdS surface. Based on this evidence, along with the fact that the similar molecule 3-TAA attaches in similar environments, it is reasonable that the PPA molecule is attaching to the nc-CdS surface by a simple place-exchange reaction. In this type of reaction a given number of oleate molecules (likely 1) displace from the surface and are replaced, after proton transfer, by a PPA carboxylate.

PL spectroscopy does not reveal changes in the PPA-coadsorption system as drastic as in the 3-TAA-coadsorption system. The diminution of the fluorescence emitted from **1-CO_2H** is reduced in the 10:1:1 3-TAA:**1-CO_2H**:nc-CdS sample by almost 50% as compared to the 1:1 **1-CO_2H**:nc-CdS sample. This is substantially greater of a reduction than that of the PPA-coadsorption system, where the analogous 10:1:1 PPA:**1-CO_2H**:nc-CdS sample has 13% less fluorescence than in the 1:1 sample of **1-CO_2H**:nc-CdS. In both coadsorption systems the peak shape changes, which seems to indicate that the coadsorbed PPA molecules are once again adsorbing in the vicinity of **1-CO_2H** on the surface.

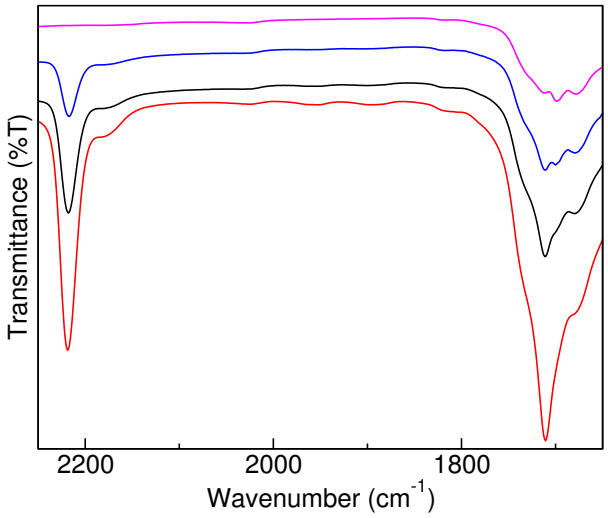

Figure 3.8: IR of phenyl propiolic acid (PPA). Top spectrum contains a 1:1 ratio of nc-CdS:**1-CO_2H**, second spectrum contains a 5:1:1 ratio of PPA:**1-CO_2H**:nc-CdS, third spectrum contains a 10:1:1 ratio of PPA:**1-CO_2H**:nc-CdS, and the fourth spectrum (bottom) contains a 20:1:1 ratio of PPA:**1-CO_2H**:nc-CdS.

1,2 Naphthalene Dicarboxylic Acid

As was done with the 3-TAA and PPA molecules, the 1,2 naphthalene dicarboxylic acid molecule (NDCA) was also coadsorbed to the nc-CdS surface along with **1-CO_2H**. NDCA was not as soluble in CH_2Cl_2 as were 3-TAA and PPA, thus sample handling was more problematic, and only two coadsorption samples were suitable for analysis. The two samples showed signs of coadsorption similar to the cases of 3-TAA and PPA. Figure 3.10 shows that the coadsorption of NDCA onto the CdS surface displaces oleate (as oleic acid, once again) and does not show displacement of **1-CO_2H**. The PL spectra show a different trend from what was observed in the 3-TAA and PPA experiments. While the peak shape as the surface concentration of NDCA increases is similar, the intensity is not that of a monotonic decrease with increasing NDCA surface concentration. After a slight preliminary decrease, the intensity then increases to a value higher than that of the 1:1 sample of **1-CO_2H**:CdS. In the case of NDCA (as well as all of the molecules displayed in Figure 3.3) none has an absorption spectrum overlapping with the emission of **1-CO_2H**, so FRET-type quenching is not possible. It is reasonable that the NDCA molecule in low

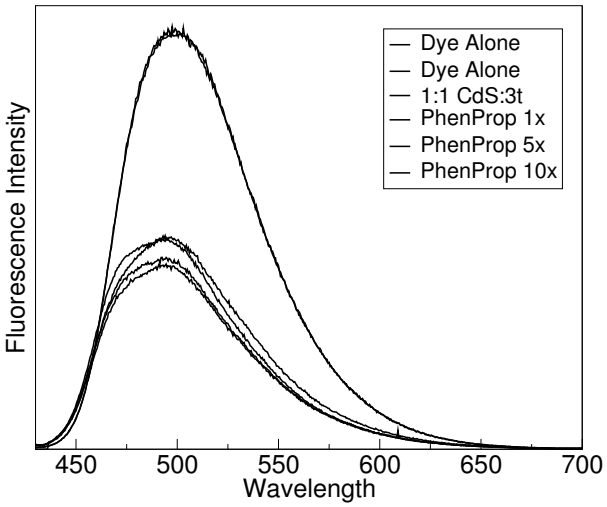

Figure 3.9: PL spectroscopy of **1-CO_2H**'s emission as PPA is coadsorbed to nc-CdS with **1-CO_2H**. Top two spectra, which are nearly coincident, correspond to solutions of **1-CO_2H** alone. The next spectrum down which possesses a shoulder on the blue side of the spectrum is the 1:1 **1-CO_2H**:nc-CdS spectrum. The spectrum at nearly the same height is the 1:1:1 sample containing PPA:**1-CO_2H**:nc-CdS in this ratio. Downwards from there is the 5:1:1 sample, and the 10:1:1 sample.

surface concentrations on CdS nanoparticles is capable of forming aggregates with **1-CO_2H** that are conducive to concentration quenching. If the aggregates form a different phase at higher surface concentration of NDCA, **1-CO_2H** in this milieu may be better equipped to produce fluorescence than to dissipate energy non-radiatively.

3.4 Concentration Quenching in Other Dyes on CdS

Cadmium sulfide nanocrystals have also been observed to produce spectra showing CQ with dyes other than **1-CO_2H**. 4-(4,4-difluoro-1,3,5,7-tetramethyl-4-bora-3a,4a-diaza-s-indacene-8-yl)benzoic acid (BODIPY, Figure 3.12) is a highly luminescent dye that is frequently used in biological applications because of its large extinction coefficient and large fluorescence quantum yield.[153] Here, we have added the BODIPY molecule to CdS dispersions in a similar fashion as we have done with **1-CO_2H**.

Figure 3.13 shows the UV-Vis and PL spectra of the BODIPY dye and its conjugate

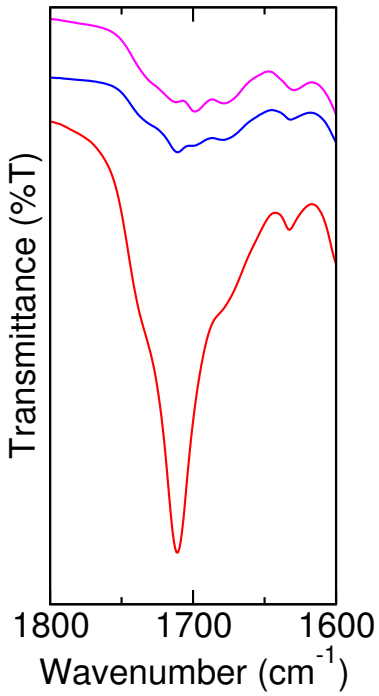

Figure 3.10: IR spectra of coadsorbed samples containing 1,2 Naphthalene dicarboxylic acid (NDCA) along with **1-CO_2H** on CdS NCs. The top trace is a sample containing a 1:1 ratio of CdS:**1-CO_2H**, the second from top is a 5:1:1 sample of NDCA:**1-CO_2H**:CdS, and the bottom is a sample is a 20:1:1 ratio of NDCA:**1-CO_2H**:CdS.

base, as deprotonated by tetramethyl ammonium hydroxide, as well as the UV-Vis absorption spectrum of the CdS nanoparticles used. The CdS nanoparticles are the same size as used in the previous chapter (2.5 nm) and they are expected to have the same surface and bulk properties. The UV-Vis absorption spectra of the BODIPY in the deprotonated state shows a slight red-shifted absorption from the protonated form, and the PL emission spectrum of BODIPY shows a blue-shift in the deprotonated state. This means that the Stoke's shift of the deprotonated version is smaller than that of the protonated version, which in turn means that the solvent stabilization of the deprotonated dye's excited state is smaller. This usually arises from an excited state with less intramolecular charge-transfer character.

In the presence of nc-CdS BODIPY adsorbs onto the surface, as can be seen in the

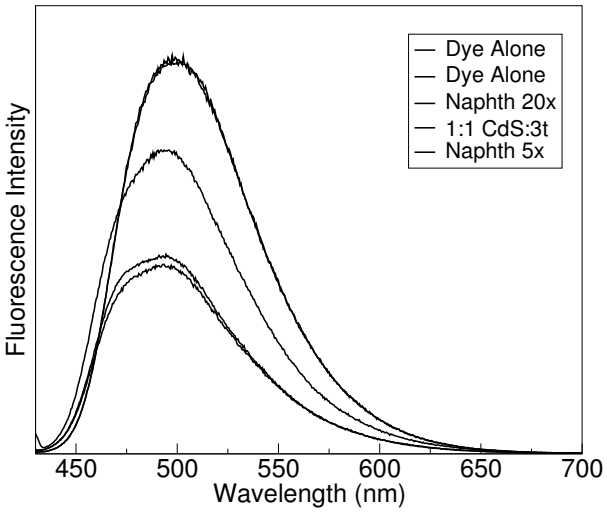

Figure 3.11: PL spectroscopy of **1-CO_2H**'s emission as NDCA is coadsorbed along with it to CdS surfaces. The upper two spectra correspond to samples of **1-CO_2H** alone before and after the other samples were analyzed. The next highest spectrum is that of a sample containing a 20:1:1 ratio of NDCA:**1-CO_2H**:CdS. The sample below is a 1:1 ratio of **1-CO_2H**:CdS and the lowest sample is a 5:1:1 ratio of NDCA:**1-CO_2H**:CdS.

NMR spectra in Figure 3.14, where the peak intensities from the BODIPY molecule in the aromatic region are slowly decreased until the 4:1 BODIPY:CdS sample. From the 4:1 sample to the 1:1 sample the peaks in the aromatic region of the NMR spectrum go from small and featureless, as they were in the 20:1 sample of **1-CO_2H**:CdS, to larger and broad, as they were in the 1:1 sample of **1-CO_2H**:CdS. From this observation it appears that the BODIPY molecule is able to attach to the CdS surface in lower numbers than is **1-CO_2H**. BODIPY's structure should be able to cover more surface area than would **1-CO_2H**, and this explains the difference between the maximum coverages. In order to ensure that the ratios are exact, atomic absorption spectroscopies are needed.

The appearance of broad, large peaks in the NMR spectrum of the 1:1 sample is revelatory. In the case of the samples of **1-CO_2H** adsorbed onto CdS NCs (see previous chapter), the disappearance of sharp peaks as CdS concentration was increased correlated with dye molecules aggregating on the surfaces of CdS NCs. This was corroborated with UV-Vis spectra showing aggregation in the same samples. At a certain point the

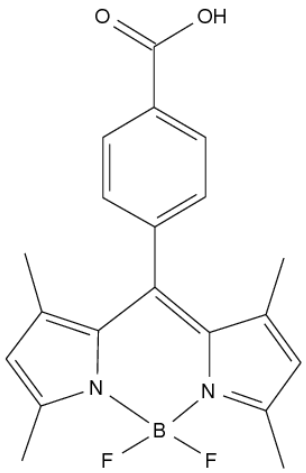

Figure 3.12: 4-(4,4-difluoro-1,3,5,7-tetramethyl-4-bora-3a,4a-diaza-s-indacene-8-yl)benzoic acid, the BODIPY molecule

disappearance of signal intensity reversed and large, broad peaks similar to those in Figure 3.14 were seen that correlated to the Cd salt of **1-CO_2H**. These peaks showed that dye molecules on the surface had a greater amount of conformational freedom as their surface concentration decreased. This is also true for the BODIPY-CdS system here where the protons on the pyrrole rings (∼6 ppm) are more pronounced than the phenyl protons which are closer to the attachment site. The phenyl protons ortho to the carboxylic acid group are expected to be downfield of the protons meta to the same, and this is shown in the NMR spectrum of the 1:1 sample. The peak at 6.8 ppm appears to correspond to the meta protons and is more intense than the peak at 7.35 ppm. From this we can conclude that the carboxylic acid group is the site of attachment because the protons moving away from this site are increasing in both sharpness and intensity.

FT-IR spectra of BODIPY in varying concentrations of CdS NCs are shown in Figure 3.15. It can be seen that the C=O peak of BODIPY's carboxylic acid group is gradually eliminated as the C=O peak of oleic acid grows in. Not only is this evidence for an alteration of the carboxylic acid group of BODIPY, it is also evidence that the BODIPY molecule displaces oleate as oleic acid in a similar way as did **1-CO_2H**, 3-TAA, PPA, and NDCA. In the previous chapter (Figures 2.5, 2.6, and 2.7) the nanoparticle

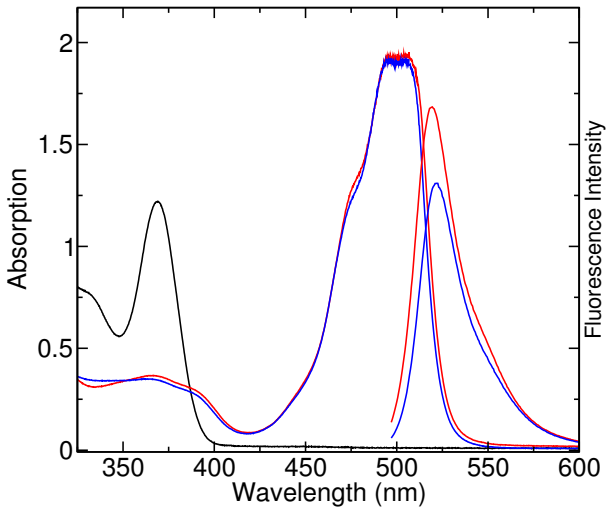

Figure 3.13: UV-Vis and PL spectra of the BODIPY dye (blue and red) and UV-Vis spectrum of the CdS (black) used in experiments with BODIPY. Blue spectra correspond to the deprotonated BODIPY dye and red spectra correspond to the protonated version of the BODIPY dye. The PL spectra in this figure were collected using a 490 nm excitation.

contributed several peaks to the region of the IR spectrum from 1800 cm^{-1} to 1600 cm^{-1} in increasing amounts as the concentration of those nanoparticles increased. This made the samples with ratios of roughly 15:1 or 20:1 **1-CO_2H**:CdS show the displacement of oleic acid by **1-CO_2H** most clearly because they did not contain significant interference from CdS surface signals.

Figure 3.16 shows that the BODIPY molecule's absorption spectrum changes as it is undergoing environmental changes that are alluded to in the NMR array (Figure 3.14). These changes may be partially related to aggregation, but they seem more complex than the simple changes that were seen in the **1-CO_2H**-CdS case where a clean isosbestic point was observed. The added complexity is that the protonation/binding state of the carboxylic acid/carboxylate functional group appears to affect the position of the absorption peak in the UV-Vis spectrum. This leads to a blue-shift that is added to the blue shift that would be expected from the BODIPY dye transitioning from an aggregated state to an isolated one.

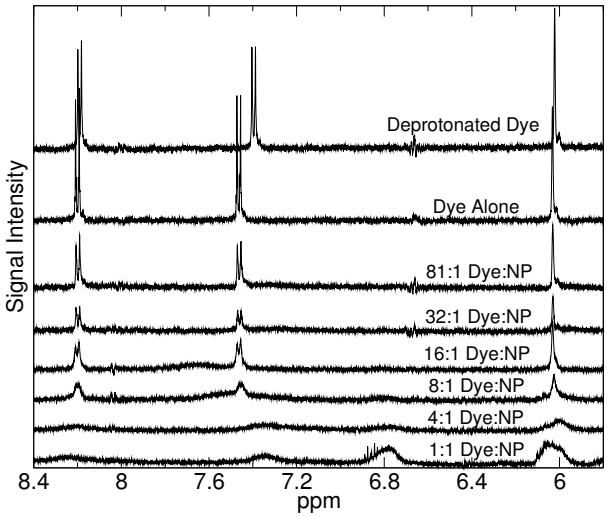

Figure 3.14: NMR spectra of BODIPY with increasing concentrations of CdS NCs from top to bottom.

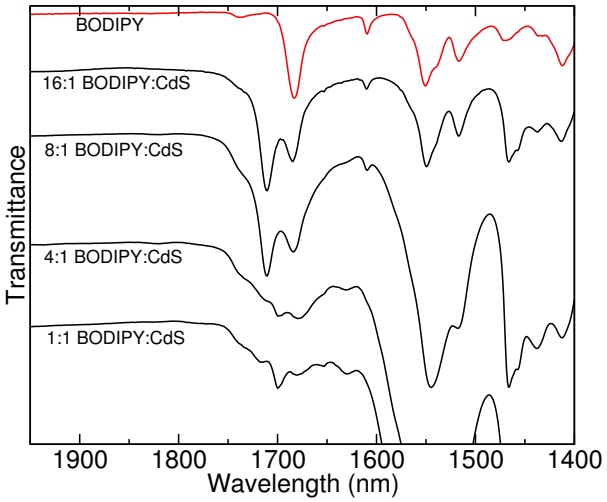

Figure 3.15: IR spectra of BODIPY with varying concentrations of CdS NCs. The peaks at 1683 cm^{-1} and 1609 cm^{-1} come from the BODIPY molecule, with the former being the C=O stretch of the carboxylic acid. The 1711 cm^{-1} peak is oleic acid's C=O stretch and it grows in as oleate is displaced as oleic acid. In the 4:1 and 1:1 samples, the nanoparticle's peaks dominate the spectrum.

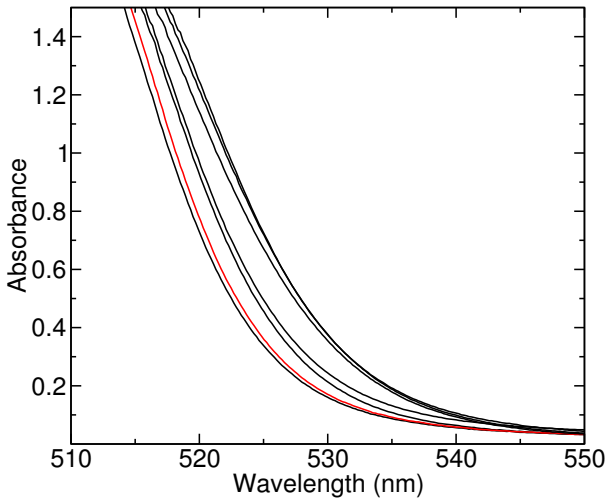

Figure 3.16: Low energy portion of UV-Vis spectra of BODIPY with increasing concentration of CdS NCs. These are the same samples as from Figure 3.14. The two most red-shifted spectra are the 16:1 and the 32:1 BODIPY:CdS samples, and inwards from there (towards the blue end of the spectrum at roughly 530 nm) is the 81:1 sample, the 8:1 sample, the 4:1 sample, the sample of only BODIPY, and the 1:1 sample.

PL spectroscopy solidifies the picture outlined above by the IR, UV-Vis, and NMR spectroscopies. In the PL spectra shown in Figure 3.17 the dye alone sample is in red, and the deprotonated dye sample is in blue. The increase in luminescence intensity and blue-shift from the protonated BODIPY to the deprotonated version was seen in Figure 3.13, but it is worth emphasizing. The dye at very low concentrations of CdS (or at high ratios of BODIPY:CdS) has a peak position that is different from both the protonated version and also the deprotonated version. This behavior has been seen previously in oligothiophene adsorption to nanoparticle surfaces. A close association of BODIPY with CdS is possibly the reason that the fluorescence peak is unique — this would provide the dye with an environment different from the solution phase. Throughout the titration, BODIPY's emission peak blue shifts, indicating that the carboxylic acid functional group is undergoing a change. The increase in luminescence intensity from the 81:1 sample to the 8:1 sample is different from what has been seen previously, however the increase from 8:1 to 1:1 is consistent with a decrease in CQ. Changes in the NMR spectra from 8:1 to 1:1 also favor a change from a CQ environment to one where CQ is

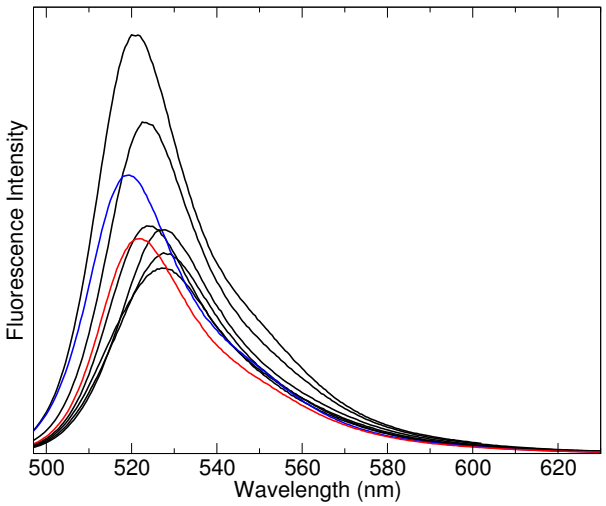

Figure 3.17: PL spectroscopy of BODIPY's emission upon excitation by 490 nm light. The red spectrum is BODIPY alone, and the blue spectrum is BODIPY deprotonated. The black spectra from bottom are 81:1 sample, 32:1 sample, 16:1 sample, 8:1 sample (blue-shifted from 16:1 sample by 3.5 nm), 4:1 sample, and the 1:1 sample.

not active. In the case of BODIPY adsorbed to CdS, it does not seem to be the case that ET pathways are active. If ET was possible it should be active in the 1:1 sample which would result in a lower fluorescence quantum yield for this sample. The fluorescence quantum yield is actually higher in the 1:1 sample than in either the BODIPY or the deprotonated BODIPY spectra, and this can be explained by the rigidization that the BODIPY molecule undergoes as it adsorbs to the surface. With fewer degrees of freedom available, the BODIPY molecule is less likely to non-radiatively dissipate the energy of the excited state. This type of behavior has been observed previously.[129]

It is known that the E_{cb} of a semiconductor nanoparticle such as TiO_2 can be lowered upon addition of strong acid. This lowering of the E_{cb} has been shown to induce electron transfer events where there was no ET before. We believe this is not the case in our nanoparticle system because of the capping nature of the oleate, the inability of highly charged species to penetrate into the oleate, and the relative weakness of the acid used. We cannot dismiss the possibility of a various array of binding sites, one of which is very sensitive to pH and which is also exposed to the solvent (such as a vertex of a

nanoparticle).

Considering the data collected with BODIPY on CdS as a whole, it appears that ET is not active from BODIPY to CdS. This can be a result of an excited state that has large amounts of electron density located far from the carboxylate attachment site, or that does not have sufficient thermodynamic driving force for ET. Based on calculations using CV data from literature reports[160] and absorption/emission data from Figure 3.13, the excited state oxidation potential of BODIPY in CH_2Cl_2 is roughly -3.2 V versus vacuum and this would make it slightly too low-energy to inject into the conduction band of nc-CdS. A combination of the two is also possible which would make ET even less probable. CQ is active, however, as can be seen from the diminished peaks in the NMR which correlate with site-exchange in the IR, and luminescence quenching in the PL. The fact that CQ is active in a dye molecule that is planar and aromatic is not surprising, but we have also provided evidence that BODIPY needs more room on the surface of the nanoparticle than does **1-CO_2H**. The lower coverage that BODIPY can achieve on the CdS surface is important because it is another step in the direction of fleshing out the structure of the surface of the CdS. If the distance between binding sites on nc-CdS can be deduced, the crystallographic faces that are active in adsorption of carboxylic acid-containing dyes may be identified. This would allow the design of ligands that could perform many tasks better than current ligands, such as blocking approach of solvent or electrolyte molecules, allowing faster/higher yield ligand exchange reactions, or adjoining nanoparticles to one another.

Implicit in the previous paragraph is the assertion that certain crystallographic faces are active in binding of carboxylic acid-containing molecules. From the current chapter's contents to this point, there is sufficient evidence to believe such an assertion. Specifically, PL and IR evidence show the carboxylic acid ligand exchanging molecules (3-TAA, PPA, and NDCA) adsorb to the same faces that **1-CO_2H** does. The limited amount of surface coverage that BODIPY reaches is further evidence that only certain faces of the crystal are active, and the TEM images from the previous chapter show that the CdS nanoparticle does have definite crystalline structure.

3.5 ZnO and Concentration Quenching

In this thesis there has only been reference to CQ as it relates to a surface-templated aggregation event where CdS is the surface. Below is presented evidence regarding surface-templated aggregate formation leading to CQ on ZnO surfaces as they are found on ZnO nanoparticles (nc-ZnO).

3.5.1 Ru(2,2'-bpy-4,4'-$(DEA)_2)_2$(2,2'-bpy-4,4'-$(COOH)_2)^{2+}$ (RuDEA)

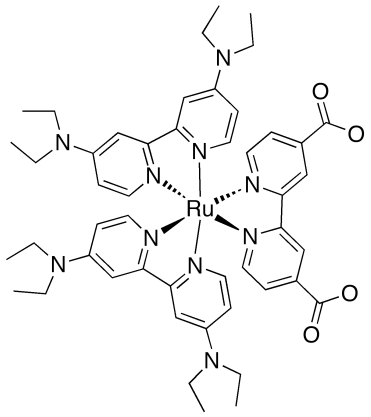

Figure 3.18: The RuDEA dye

Ruthenium complexes have been widely studied as sensitizer dyes for DSSC applications.[6,8,19,29,35,38,161] As noted in the Introduction, these molecules have very long excited state lifetimes, which makes the quantum yield of ET reactions where they are electron donors very high. In order to create a dye molecule with quantitative yields in ET reactions and faster regeneration times after ET reactions, alkylamine groups can be added to the 4,4'-positions of the most common Ru complex, Ru(2,2'-bpy)$_2$(2,2'-bpy-4,4'-$(COOH)_2)^{2+}$.[161,162] The electron-donating character of the alkylamine groups will drive the ET reaction towards completion and they will also produce excited states of higher energy.

The first molecule that will be discussed here is the RuDEA molecule (Figure 3.18) which contains diethylamino groups at the 4,4'-positions on the bipy ligands. Figure 3.19 shows the aromatic regions of the NMR spectra of RuDEA as the concentration of

nc-ZnO is increased. Initially, RuDEA's peaks shift very slightly downfield, probably as a result of the solvent change as nc-ZnO are added in hexanes. As the concentration of nc-ZnO increases, the peaks from RuDEA are seen to diminish in the same way as have the other examples of adsorption of molecules to nanoparticle surfaces. A slight complication comes from contaminants in the hexylamine that was used as a capping agent during the nc-ZnO synthesis. As the concentration of nc-ZnO increases, these contaminants also increase, and care must be taken to watch the peaks belonging to RuDEA and not those belonging to the contaminants. The last point in the titration is shown in the blue spectrum.

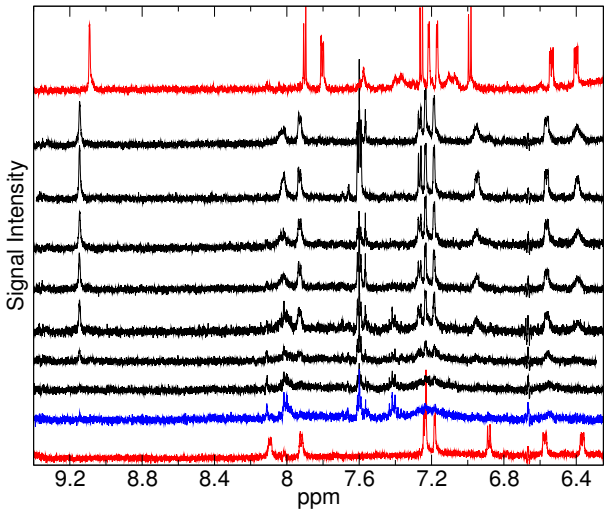

Figure 3.19: NMR spectra of the aromatic protons in RuDEA as the RuDEA dye is titrated by ZnO with hexylamine capping agents. The top spectrum is that of RuDEA with hexylamine, and the bottom spectrum is of RuDEA alone. From the top black spectrum (second from top) down is a 160:1 RuDEA:nc-ZnO sample, 80:1 sample, 60:1 sample, 46:1 sample, 28:1 sample, 16:1 sample, 12:1 sample, and a 7:1 sample.

Analysis of the PL spectra in Figure 3.20 shows that the dye initially starts out with the appearance of neither the deprotonated form, nor the protonated form. The top black spectrum in Figure 3.20 belongs to the ratio of RuDEA:nc-ZnO, and the concentration of nc-ZnO in the samples increases as the reader follows the spectra

downwards. The luminescence reaches a minimum, after which the luminescence increases once again. This is quite similar to the previous discussions where the reversal of luminescence quenching occurs at the same sample as where the NMR spectra show complete adsorption of dyes onto the surface (i.e. no free dyes are detected). This provides evidence that the CQ mechanism is also active in the RuDEA:nc-ZnO system.

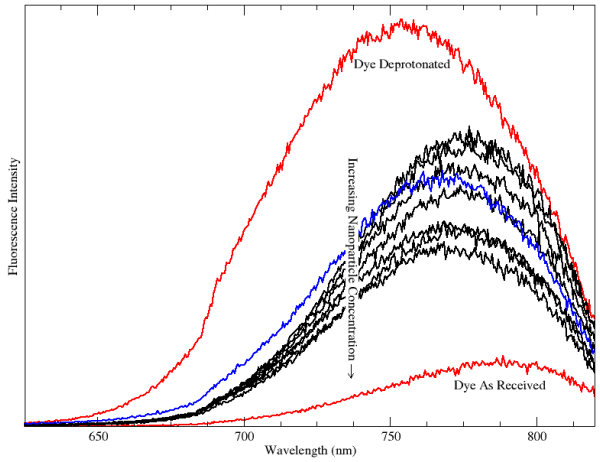

Figure 3.20: PL spectra of RuDEA in the protonated form, deprotonated (with hexylamine), and with varying concentrations of nc-ZnO using a 420 nm excitation wavelength. The samples in black with nc-ZnO are decreasing in RuDEA:nc-ZnO ratios as the intensities decrease, starting with 160:1. Following this is 80:1, 60:1, 46:1, 28:1, 16:1, and 12:1. The blue spectrum is a sample with 7:1 RuDEA:nc-ZnO.

Normally the possibility of CQ in a non-planar fluorophore would be dismissed because of the importance of aggregation in the CQ mechanism. However, it appears that aggregation may not be required; a set of adjacent dyes may continue to undergo CQ even if they are only closely associated without $\pi - \pi$ stacking. One should also be careful to not preclude aggregation of dye molecules simply based on their crystal structures, as it may be the case that the bipy ligands of the RuDEA dye are able to participate in $\pi - \pi$ stacking aggregation.

Figure 3.21 shows no signs of aggregation, but does show a consistent trend towards higher extinction coefficients as the concentration of nc-ZnO is increased. A problematic result of the adsorption of RuDEA is the MLCT's peak shifting towards the blue from

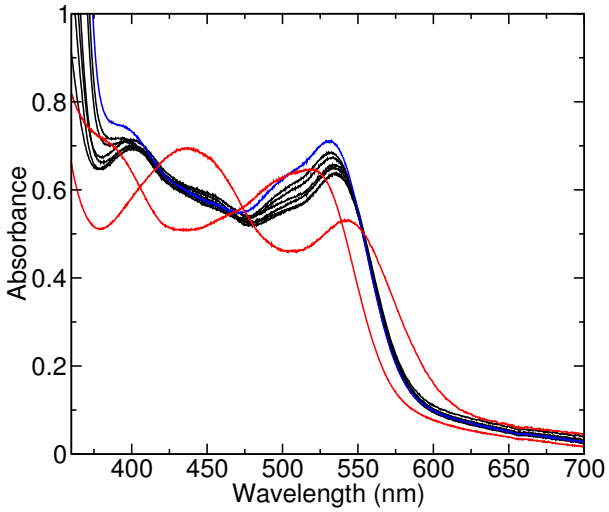

Figure 3.21: UV-Vis spectroscopy of RuDEA in presence and absence of nc-ZnO. The red spectra are of RuDEA alone, where the spectrum absorbing furthest to the red is the protonated version (as received) and the other is the deprotonated version. The black spectra are increasing in concentration as absorption increases at 535 nm, and the blue spectrum is the highest concentration of nc-ZnO.

535 nm to 530 nm. While the blue-shift is not as large as the one that is seen as RuDEA is deprotonated, a 5 nm blue-shift in the most intense region of the solar spectrum can cause problems for solar cell efficiency maximization should the RuDEA dye be used in such an application.

Ultrafast TA spectroscopy was performed on samples containing RuDEA and nc-ZnO, but these were unsuccessful.

3.5.2 1-CO_2H and nc-ZnO

Given the propensity of **1-CO_2H** to participate in CQ on nc-CdS, it would not be surprising for it to do the same on nc-ZnO surfaces as well. The nc-ZnO surface is similar to the surface of nc-CdS because they are both capped with aliphatic groups and are dispersed in non-polar solvents.

Figure 3.22 shows that as **1-CO_2H** is titrated by nc-ZnO, a similar trend forms where the luminescence intensity first decreases, and then increases once again. In

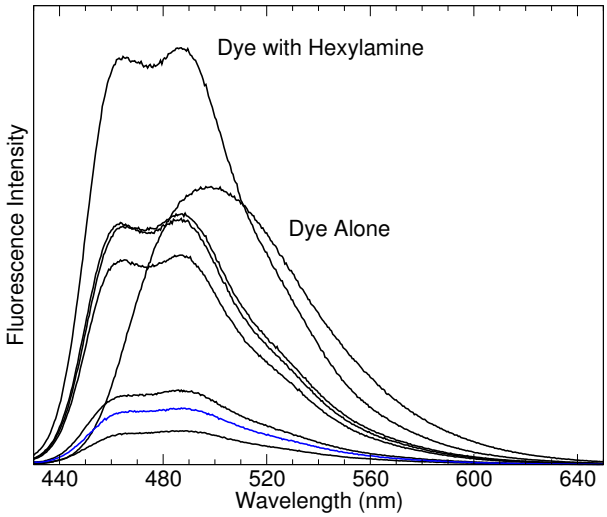

Figure 3.22: PL of **1-CO_2H** in the presence and absence of nc-ZnO with an excitation wavelength of 420 nm. Black traces are increasing in nc-ZnO concentration as intensity decreases with ratios of **1-CO_2H**:nc-ZnO of 180:1, 90:1, 68:1, 45:1, and 27:1. The blue trace is a sample with a ratio of **1-CO_2H**:nc-ZnO of 18:1. The samples of **1-CO_2H** alone and with hexylamine are labeled accordingly.

contrast to the previous example of **1-CO_2H** with nc-CdS, **1-CO_2H** starts out in the protonated form but quickly is deprotonated once the nc-ZnO dispersion is introduced. Evidence for the immediate deprotonation can be seen in the spectrum of the 180:1 sample, where the familiar shape of the deprotonated **1-CO_2H** can be seen in the vibrational progression and the blue-shifted peak position. This is likely a result of the presence of hexylamine in the nc-ZnO dispersion.

NMR results (Figure 3.23) agree with the PL results regarding the protonation state of **1-CO_2H**, as the protons near 7.1 ppm show deprotonation of the carboxylic acid functional group. In addition, the NMR results indicate that the titration of **1-CO_2H** by nc-ZnO is almost exactly at the equivalence point at the 27:1 sample, as the signals in that sample are indistinguishable from the baseline. It should be noted that there is a possibility that the equivalence point came before the 27:1 sample, however, from this data, we can only conclude that the equivalence point is between the 45:1 ratio and the 18:1 ratio.

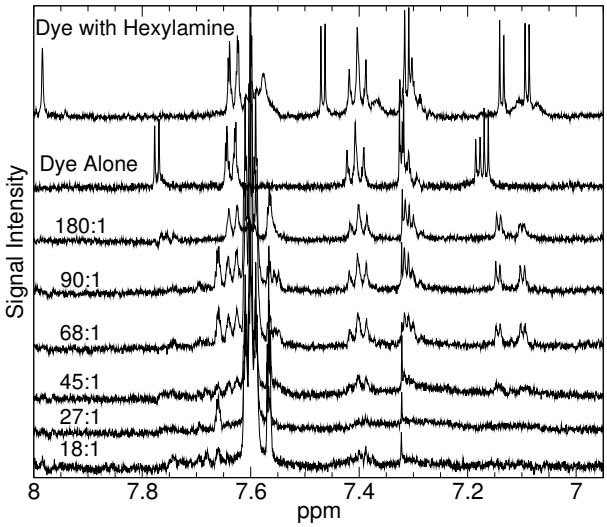

Figure 3.23: NMR of the aromatic region of **1-CO_2H** in the presence and absence of nc-ZnO. The ratios of **1-CO_2H**:nc-ZnO are included on top of the spectra that they correspond to. The large peak slightly below 7.6 ppm is a contaminant from the hexylamine that was not removed by distillation.

The recovery of **1-CO_2H**'s protons at the end of the titration is not observed because the ratio of **1-CO_2H** to nc-ZnO was not taken to high enough levels. Had the concentration of nc-ZnO been high enough that the ratio of **1-CO_2H** to nc-ZnO went lower than 10:1, we expect that the peaks would have recovered as before. However, other factors could also inhibit the recovery of the protons' signals, which we will not explore here.

Just as before, the UV-Vis spectra of **1-CO_2H** near the equivalence point shows two isosbestic points forming near the 450 nm region that was observed to contain an isosbestic point earlier. The isosbestic point in the nc-CdS example was indicative of the environment of the dye molecules changing from surface-saturation to surface-isolation. In this case the interpretation is identical — from the 27:1 ratio to the 18:1 ratio there should be a transition to nc-ZnO surfaces that are sparsely covered.

The luminescence recovery (Figure 3.22) and the NMR results (Figure 3.23) point to an equivalence point of binding sites to adsorbates (**1-CO_2H** molecules) near the 27:1 ratio. The UV-Vis results (Figure 3.24) suggests a transition from surface saturation

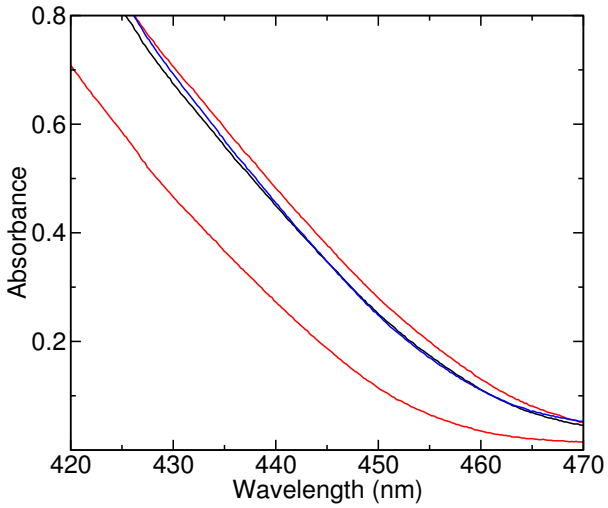

Figure 3.24: UV-Vis of **1-CO_2H** in the presence and absence of nc-ZnO.

to isolation on the surface of **1-CO_2H** at this point in the titration. The ratio is notable because the nc-ZnO used in this study are 4.7 nm in diameter. The difference in surface area between a 2.5 nm CdS particle and a 4.7 nm ZnO particle (assuming spherical geometry) is roughly a factor of 3.5. Such a huge difference in the surface area would be expected to translate into a larger capacity of dye loading, however, the maximum coverage is very similar to that of the titration of **1-CO_2H** by nc-CdS. The most likely reason for this discrepancy is that, where the nc-CdS system has a well-studied extinction coefficient that can be used to measure concentrations of nc-CdS dispersions, no such figures are available for nc-ZnO. The lack of extinction coefficient leads to approximations and estimations as to the amount of nc-ZnO in solution, creating possible errors. Thus the uncertainty in the equivalence point in ZnO titrations of **1-CO_2H** is greater than that of the nc-CdS titrations.

3.5.3 1-CO_2H and Acetate-Capped ZnO

In previous publications [120,121] using the same dye molecule (**1-CO_2H**) but on ZnO dispersions made of acetate-capped ZnO (ac-ZnO), ultrafast transient absorption results were reported to suggest decreasing ratios of dye:nanoparticle would lower electron transfer efficiencies and yields. Steady-state luminescence quenching behavior in these

publications was very similar to all of the previous titrations of dye with nanoparticles outlined above. The luminescence intensity reached a minimum at a ratio 20 **1-CO_2H** molecules to 1 ZnO nanoparticle of 3 nm diameter, after which the intensity increased once again and settled to a level of 1/3 of the intensity of the **1-CO_2H** alone sample. The explanation of the quenching behavior offered was that Zn^{2+} can form a soluble complex with terthiophene and this complex is emissive.[120,121] It was hypothesized that Zn^{2+} dissociated from the surface of a ZnO nanoparticle and complexed with **1-CO_2H**. This would produce the same type of PL Stern-Volmer plot as we observe, where the luminescence is diminished by a small amount of nanoparticle dispersion, but then the luminescence increases again as more nanoparticles (and therefore more Zn^{2+}) are added. The hypothesis is a well-composed one, but problems appear in its foundation upon inspection.

Scattering in the UV-Vis spectra found in the publications at hand showed that solubility was a problem, but in the samples which showed no evidence of scattering a significant red-shift was observed in the red-side of the **1-CO_2H** absorption band. A red shift of this type typically indicates $\pi - \pi$ stacking or aggregation of some type amongst fluorophores. Just as in the case of **1-CO_2H** with nc-CdS, the red shift disappears as the concentration of nanoparticles is increased.

The ultrafast results in Huss, et al.[120] that were interpreted to show a diminished electron transfer yield at lower ratios of **1-CO_2H**:ac-ZnO also contained similarities with the **1-CO_2H**/nc-CdS system. Specifically, the cation radical feature at 2.05 eV which was used to make the claim of the presence of ET, showed up more prominently in the samples towards the end of the titration than it did at the beginning. The feature correlated quite well with the cation radical that was created in spectroelectrochemical experiments, giving credence to the identification of the feature at 2.05 eV as the cationic product of the dye undergoing an electron transfer oxidation. This feature's prominent appearance at the end of the titration indicates a higher quantum yield for the ET reaction as the ratio of **1-CO_2H**:ac-ZnO decreases.

NMR studies were not performed at the time of publication, and given their usefulness in the past, they were conducted here. Figure 3.25 shows the NMR spectra of various ratios of **1-CO_2H** to ac-ZnO. It can be seen that there are no sharp peaks in any of the spectra containing nanoparticles. Based on the binding constants reported

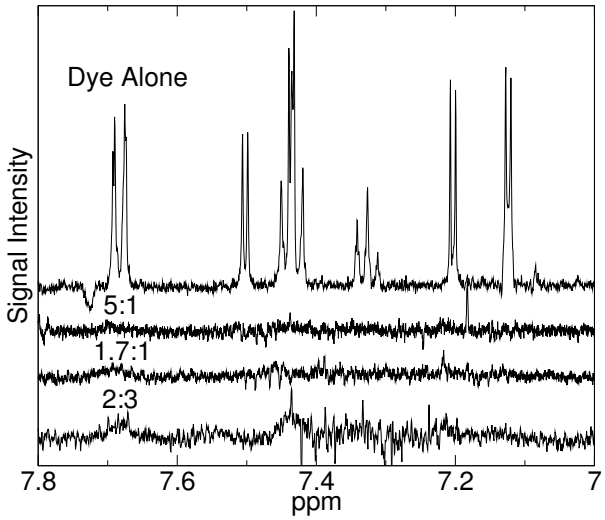

Figure 3.25: NMR spectra of **1-CO$_2$**$^-$ alone and **1-CO$_2$H** in the presence and absence of ac-ZnO. The ratios listed correspond to the ratios of **1-CO$_2$H** to ac-ZnO nanoparticles.

in Rossini et al. for the reaction where **1-CO$_2$H** binds to ac-ZnO and for the reaction where **1-CO$_2$H** binds to Zn^{2+}, Zn^{2+} binds to **1-CO$_2$H** more than an order of magnitude more strongly. With this strength of binding, one would expect to see the complex Zn(**1-CO$_2$**)$_2$ appear in one of the NMR spectra shown in Figure 3.25. Furthermore, the 2:3 sample seems to show some structure recovering in the positions that the phenyl peaks would be expected. The higher ratios of **1-CO$_2$H** to ac-ZnO are not shown as they had the same solubility issues as was reported in Rossini, et al.

Figure 3.26 explores the sample containing a 1.7:1 ratio of **1-CO$_2$H** to ac-ZnO more thoroughly. This sample was created and analyzed and the spectrum is labeled 1.7 (a). One week after the original sample was created it was analyzed once more, and this is the spectrum labeled 1.7 (b). To test the hypothesis that Zn^{2+}, if present, would extract dye molecules from the surface of ac-ZnO, a four-fold excess (versus **1-CO$_2$H**) was added to the sample 1.7 (b). Spectrum 1.7 (c) shows that added Zn^{2+} did not have any effect on the NMR spectrum of **1-CO$_2$H**, and it continued to be adsorbed to the surface of ac-ZnO. To eliminate the possibility of a slow reaction with Zn^{2+}, the sample from spectrum 1.7 (c) was re-run after 3 days and this is spectrum 1.7 (d). The insensitivity of **1-CO$_2$H** adsorbed to ac-ZnO to Zn^{2+} is inconsistent with the claim that

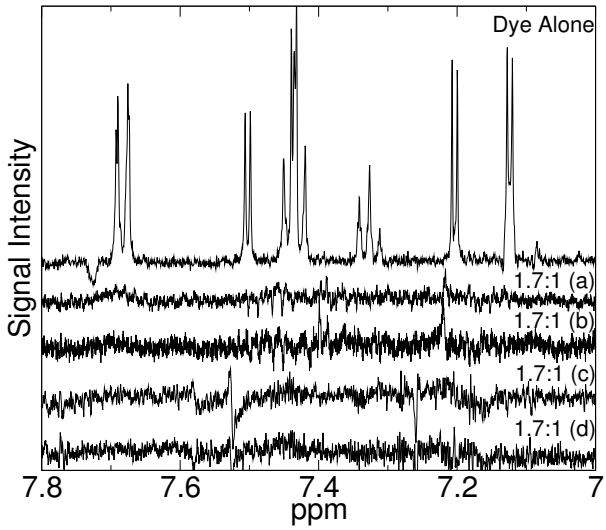

Figure 3.26: NMR spectra of **1-CO$_2$**$^-$ alone (top) and **1-CO$_2$H** with ac-ZnO (lower four spectra). The spectrum labeled 1.7:1 (a) corresponds to a sample with a 1.7:1 ratio of **1-CO$_2$H**:ac-ZnO, 1.7:1 (b) is a spectrum of 1.7:1 (a) after 1 week, 1.7 (c) is sample 1.7 (b) with a four-fold excess of $Zn(NO_3)_2$, and 1.7 (d) is sample 1.7 (c) after three days. The solutions tested here remained clear throughout the course of this study.

Zn^{2+} is capable of binding **1-CO$_2$H** much more strongly than the surface of ac-ZnO.

Based on the discussion above and the NMR data presented in Figures 3.25 and 3.26, the conclusion reached here is that the system of **1-CO$_2$H** and ac-ZnO is likely susceptible to CQ, as is the case for nc-ZnO, and nc-CdS. It is quite likely that there exists some quantity of dissolved Zn^{2+} in some form in the system comprised of ac-ZnO, but the insensitivity to this ion by the surface-adsorbed **1-CO$_2$H** means that CQ is the most probable explanation for the steady-state luminescence results.

3.6 Conclusion

The prevalence of CQ in the studies outlined above is interesting given that it has been overlooked in literature reports. For example, a high surface coverage of terthiophene dyes on the surface of CdS nanoparticles is the situation found in Antoun et

al.[116] In this environment, as well as others found in similar studies using an oligothiophene molecule adsorbed onto a nanoparticle surface, a CQ mechanism is probable.[113,115,163] Specifically, studies which include steady-state luminescence measurements[113,116] show that the best PL quench is found at levels of around 20 oligothiophene molecules to 1 nanoparticle for a 2-3 nm particle, which is almost exactly the maximum coverage in our studies. This is the point where oligothiophenes have been shown in the past two chapters to have the best CQ efficiency. More evidence that the dyes are in a position conducive to forming "contact dimers" is found in Beek and Janssen where a red shift in the UV-Vis is referred to and also a smaller steady state quench is found when the oligothiophene dye is replaced by the more bulky OPVn.[113] An excellent experiment by these authors elucidating a key aspect of this phenomenon is found in another work[115] where the linkages are lengthened between the carboxylate and the oligothiophene. These authors find that a longer linkage leads to a diminished PL quench of the dye when they are adsorbed onto TiO_2 — something that could be expected if the "contact dimer" hypothesis was correct. Extra conformational flexibility imparted by an aliphatic group between the oligothiophene and the carboxylate anchoring group would decrease the likelihood that "contact dimers" would form for an appreciable amount of time.

It is not to say, however, that electron or energy transfer to the nanoparticles is not involved in quenching the luminescence in the studies in question. In fact, in a paper that does not discuss the possibility of CQ, Milliron et al. point out that a quench of terthiophene's fluorescence upon adsorption to CdSe nanoparticles leads to an increase in the luminescence of the nanoparticle.[122] This is evidence that electron injection or energy transfer to the CdSe nanoparticle has occurred. In our studies as well, we observe an electron transfer component of the S_1 quench at the point of maximal coverage (see Figure 2.21).

The current chapter's data shows that CQ is an active pathway in many dyes and nanoparticles, and it also provides a bit more insight into possible CQ mechanisms. The most instructive experiment is the RuDEA/nc-ZnO case, where concentration quenching is seen to operate. As noted above, this case is surprising because the RuDEA molecule is not a planar aromatic dye. The octahedral center should create a sphere-like shape that will adequately prevent aggregates which, in turn, should also prevent CQ. The presence

of CQ suggests that the virtual photon hypothesis may not be correct. The reader will recall that in order for the virtual photon process to occur, an aggregate must form and this aggregate must have a red-shifted absorption peak such that a Stokes-shifted emission can excite it. In the RuDEA case there is no such red-shift. Furthermore, RuDEA is expected to undergo intersystem crossing (ISC) so quickly that the emission of the RuDEA molecule is almost certainly phosphorescence. This emission, as can be seen in Figure 3.20, does not have substantial overlap with any portion of the absorption spectrum (Figure 3.21).

If FRET-type CQ mechanisms are discarded, possible explanations for the data are the presence of Zn^{2+} in solution, experimental errors, or a Dexter-type energy transfer CQ mechanism. Zn^{2+} in solution is unlikely to have a role because NMR spectroscopy suggests that the dye remains bound to a slowly rotating object in the dispersed phase, and Zn^{2+} does not fit this description. Experimental errors, while possible, are unlikely because of the match between the NMR and PL data. The NMR signals disappear at the same time that the PL intensity recovers, just as had happened in the previous examples. This leaves us with the possibility of a Dexter-type energy transfer reaction where the molecules undergoing the reaction exchange electrons and the chances of one of the molecules dissipating the energy increases as more molecules cluster together. The RuDEA molecule, which has lifetimes of nanoseconds in the solution phase, would only need to dissipate energy slightly more rapidly to observe CQ in the steady-state PL. Clustering of RuDEA molecules on nc-ZnO surfaces serves to increase the number of nuclei known to enable spin-orbit coupling in a particular area, and this could provide a mechanism by which the energy could be dissipated either radiatively or non-radiatively, with or without the Dexter energy transfer mechanism.

The final conclusion to draw from the current chapter is that the RuDEA dye takes an enormous amount of space on the surface of nc-ZnO. Only about 10 RuDEA dye molecules can fit on nc-ZnO, but about 25 **1-CO_2H** dye molecules can fit on the same surface of nc-ZnO. This comparison is important because the nc-ZnO came from the same synthetic batch and should have identical properties on average. If an organic dye has 1/2 the extinction coefficient as does a ruthenium complex dye which absorbs in a similar area of the solar spectrum, the organic dyes will absorb more incident light than will the ruthenium dyes. Assuming that the drive to replace ruthenium complex

dyes continues, these studies of coverage by dyes on the surfaces of nanoparticles will be useful.

Chapter 4

Interaction Between Terthiophene Dye and Small CdS Particles

Previous chapters outlined the interaction between terthiophene dye molecules (**1-CO_2H**) and cadmium sulfide nanoparticles of 2.5 nm diameter. This chapter studies the dependence of the electron transfer rate on the diameter of CdS particles to which **1-CO_2H** is attached. Specifically, this chapter outlines a series of experiments where the electron transfer reaction from **1-CO_2H** to CdS nanoparticles has been shut off by increasing the size and therefore the energy of the conduction band to a point that is inaccessible by excited state **1-CO_2H** dye molecules. The fact that quantum confinement created an inaccessible conduction band is convenient because we are now able to conclude with reasonable certainty that **1-CO_2H** had been injecting into the conduction band of the 2.5 nm particles. Furthermore, with the electron transfer pathway removed, concentration quenching (CQ) remains as the only fast excited state relaxation pathway, allowing it to be studied more closely.

4.1 Introduction

It is known that the size of a nanoparticle dictates important materials properties such as melting point and surface reactivity.[60–62,99] For the purposes of dye-sensitized solar cell (DSSC) applications where a nanoparticle participates in electron transfer (ET) reactions with either adsorbed molecules or other nanoparticles, these properties must be closely monitored.[164] In addition, control of the band gap structure is important and can also be realized by modification of nanoparticle size. Control over, or at least knowledge of band positions is necessary to determine in which direction a given ET reaction will proceed. If band positions are incorrect for example, a DSSC will not complete a circuit and the device will not function.

Changing the band positions of an electron-accepting semiconductor has been achieved in prior reports by addition of adsorbates[12,69,87] or dopants,[85] but the principles of quantum mechanics make it possible to achieve the same goal without modifying the surface and introducing the associated complications. Size-induced changes in band positions can be useful in the DSSC field to align the energy levels such that the system as a whole can use a particular electrolyte or a particular dye molecule which would otherwise be too inefficient. Particle size-dependence on electron transfer rates has been shown,[165–167] meaning that changing the size also changes the distribution of the density of states (DDOS) inside the particles. Modification of the DDOS has an influence on the rates of electron transfer to and from the nano-sized material being studied.

The theory that best describes electron transfer reaction rates comes from a derivation of Fermi's golden rule, which states that the rate of a transition between reactants and products is proportional to the square of the matrix element of the first order term of the zero order states.[130] This theory, commonly referred to as, Marcus theory[168] (outlined in Equation 4.1) has grown to be widely accepted as a result of Closs and Miller's proof of concept reaction.[169]

$$\mathsf{Rate}(k) = \frac{2\pi}{\hbar} \left|H_{\mathsf{AB}}\right|^2 \frac{1}{\sqrt{4\pi\lambda k_b \mathsf{T}}} \exp \frac{-(\lambda + \Delta\mathsf{G}^\circ)^2}{4\lambda k_b \mathsf{T}} \tag{4.1}$$

Equation 4.1 shows that the reaction rate of an electron transfer reaction depends on the coupling between product and reactant states ($|H_{\mathsf{AB}}|^2$), but also on the reorganization energy (λ) and the free energy driving force ($\Delta\mathsf{G}^\circ$). If any of these becomes

substantially disfavorable for the electron transfer reaction to proceed, the rate will slow to a negligible pace.

In this chapter, we aim to change the free energy driving force, $\Delta G°$, by changing the size of the nc-CdS nanoparticles that are used as electron acceptors in such a way that we can disrupt the ET reaction from **1-CO_2H** to nc-CdS. In doing so, we will be able to develop a better understanding of the ET process. In the absence of ET, we will also be able to better understand the CQ process.

4.2 Experimental

Cadmium oxide (99.999 atom % Cd) was obtained from Strem Chemicals, oleic acid and dichloromethane were obtained from Fisher Chemicals, sulfur (USP grade) was obtained from JT Baker, and dichloromethane-D_2 (99.9 % D atom), hexanes (spectroscopy grade), and octadecene (90%) were obtained from Sigma Aldrich. All chemicals were used without further purification.

The terthiophene dye, 3',4'-dibutyl-5"-phenyl-[2,2':5',2"-terthiophene]-5-carboxylic acid (**1-CO_2H**) shown in Figure 2.2 was synthesized by the reported method.[120] Oleate-capped CdS nanocrystals (nc-CdS) were synthesized by a literature procedure,[95] with the exception that the quantity of all reagents and solvents was doubled.

The following procedures were performed in air. The steady-state emission spectra were recorded through two Spex Fluorolog 1680 0.22 m double spectrometer gratings equipped with a 450 W xenon source. All spectroscopy was performed in quartz cuvettes with a 3 mm path length in CD_2Cl_2 unless otherwise noted. ^{1}H NMR spectra were recorded on a 500 MHz Varian Inova with the standard 1D ^{1}H pulse sequence at a gain of 60 dB and 256 transients per spectrum. ^{1}H-NMR spectra for the dye/NC dispersions were scaled to render the noise level between 7.85 and 7.95 ppm equal in each spectrum. UV-Vis spectra were recorded using a DH 2000 BAL Mikropack deuterium/halogen source and an Ocean Optics USB4000 detector. IR spectra were measured on specimens drop cast from solution onto a NaCl plate and dried under a stream of $N_{2(g)}$. A Thermo Nicolet 670 FTIR was used with each spectrum comprising 128 scans.

4.3 Results and Discussion

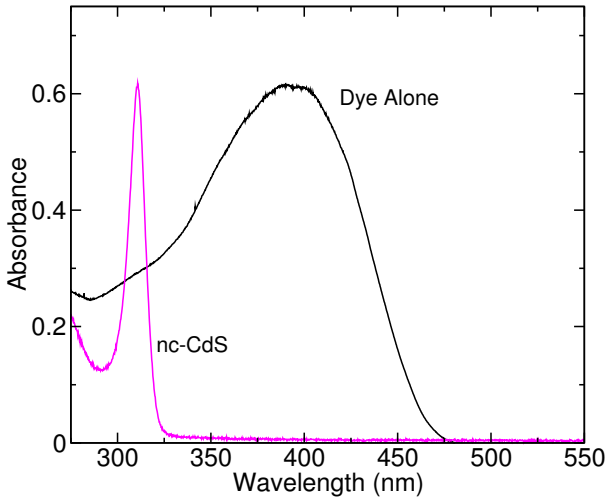

Figure 4.1: UV-Visible spectrum of small nc-CdS and spectrum of **1-CO_2H** alone that has been scaled down by a factor of 1/3. The peak position for the nc-CdS indicates a 1.5 nm diameter. Both spectra have been subtracted by the spectrum of the cuvette filled with the respective solvent.

Oleate-capped cadmium sulfide nanoparticles (nc-CdS) were synthesized according to the usual procedure, but with a shorter time of ripening as prescribed by Yu and Peng.[95] The resulting nc-CdS had a first exciton peak at 311 nm (Figure 4.1), which indicated an average diameter of 1.5 nm, a full nanometer smaller in diameter than the previously studied nc-CdS batches.

Given the discussion from the previous chapter in which it was stated that according to simple calculations the conduction band was slightly below the excited state oxidation potential of **1-CO_2H**, an increase in the band gap from 3.3 eV (2.5 nm particles) to almost 4 eV (1.5 nm particles) is expected to shut off the ET pathways from **1-CO_2H** to nc-CdS (so long as the original ET reaction we observed previously was from **1-CO_2H** into the conduction band of nc-CdS). Figure 4.2 shows that this appears to be the case. The initial spectrum of **1-CO_2H** alone shows a fluorescence which decreases after addition of nc-CdS. The sample containing a 7.5 to 1 ratio of **1-CO_2H** to nc-CdS appears to be the equivalence point in the titration where the CQ pathway is most active,

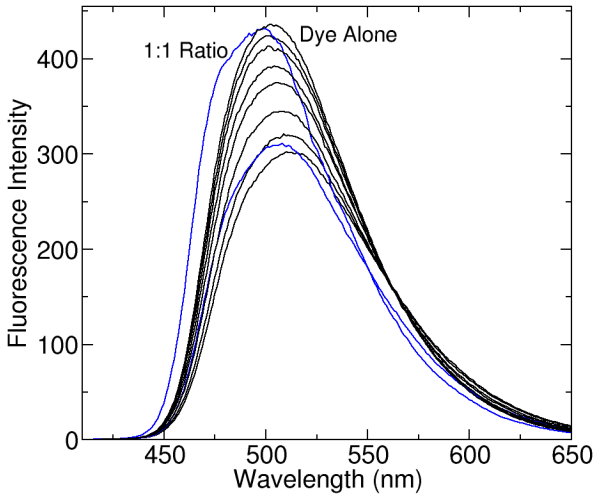

Figure 4.2: Photoluminescence data of a titration of **1-CO_2H** with nc-CdS of small size using an excitation wavelength of 400 nm. The black spectra are increasing in concentration of nc-CdS as they decrease in intensity, while the two blue spectra are increasing in concentration of nc-CdS as they increase (blue-shift) in intensity (peak position). From the top, black spectra contain **1-CO_2H**:nc-CdS ratios of 100:1, 50:1, 30:1, 20:1, 15:1, 10:1, and 7.5:1. From the bottom upwards, blue spectra contain ratios of 2:1 and 1:1.

and after arriving at the 1:1 ratio the luminescence intensity does not show quenching as compared to the dye alone sample. The lack of quenching at the 1:1 sample suggests that there is no ET pathway available for the dye, in contrast to the experiment with 2.5 nm particles which showed roughly a three-fold quench at the 1:1 ratio.

The fact that the CQ pathway appears to be present in this sample is illustrative of the fact that the surface does not change in ways other than dimension (i.e. the crystallographic faces presented do not differ radically from previous studies) as the particle size decreases. That the equivalence point comes at the 7.5:1 ratio of **1-CO_2H** to nc-CdS indicates that the crystallographic faces which template the aggregations that give rise to CQ are much smaller. Previously it was concluded that 20 dye molecules could fit onto the 2.5 nm nc-CdS particles. The decrease from 20 to roughly 8 is expected, given that the surface area change (assuming spherical particles) from the 2.5

nm particle to the 1.5 nm particle is almost a three-fold reduction.

It should be noted that the 7.5:1 ratio found at the maximum quenching point is debatable, as the empirical fit that was used to determine the extinction coefficient (and therefore the concentration) is at the small end of the experimental data that was used by Yu, et al. to create the fit.[104] The reliability of the fit at this point is therefore reduced, meaning that the concentrations that determine the ratios enumerated here may be incorrect. However, it does not appear that there is a significant error because the fluorescence level at maximum quenching is reduced significantly, which would be expected if the crystallographic faces were smaller and less able to serve as a template to aggregation. The experiments containing 2.5 nm particles with **1-CO_2H** showed an eight-fold quench when 400 nm light was used for excitation, while the 1.5 nm particles in the same experiment show only a 70% quench.

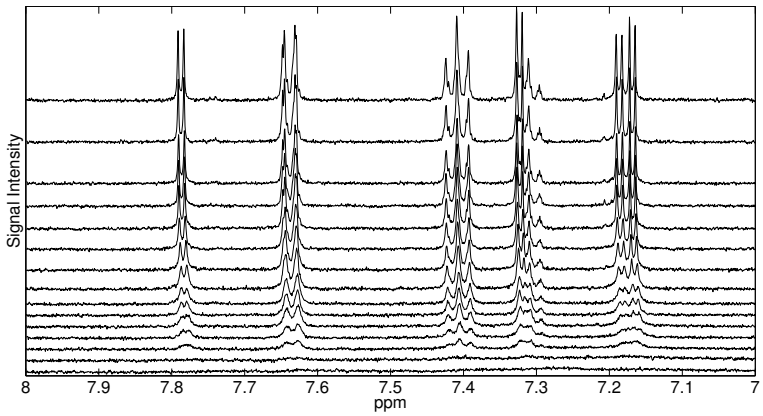

Figure 4.3: NMR spectra of the aromatic region of **1-CO_2H** as it is added to increasing concentrations of nc-CdS. The ratios of **1-CO_2H**:nc-CdS from the top downwards are 100:1, 70:1, 50:1, 40:1, 30:1, 25:1, 20:1, 17:1, 15:1, 12:1, 10:1, 7.5:1, 5:1, 2:1, and 1:1.

Just as before, the NMR spectrum (Figure 4.3) of **1-CO_2H** in the presence of 1.5 nm nc-CdS shows that the aromatic protons are broadened into the baseline at some point in the titration. The broadening of the peaks from **1-CO_2H** into the baseline correlated before and continue to correlate in this study with CQ. Unlike before, the proton signals do not recover, and the reasons for this are unknown.

Also in common with previous experiments containing **1-CO_2H** and 2.5 nm nc-CdS, the UV-Vis spectra showed signs of red-shifted absorptions in the samples where NMR

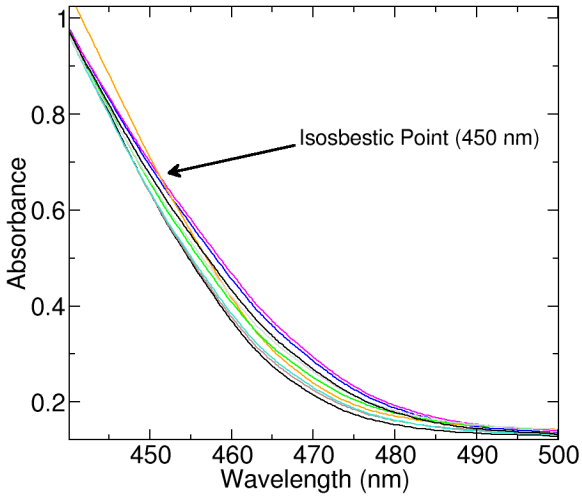

Figure 4.4: UV-Vis of **1-CO_2H** in the presence of small particles, with constant concentration of dye. The development of a red-shifted absorption onset and an isosbestic point at 450 nm are similar to what was previously observed.

broadening was greatest. Additionally, an isosbestic point was formed at 450 nm once again between the sample showing greatest quenching and the end of the titration. The position of the isosbestic point is nearly identical to that of the previous isosbestic point with **1-CO_2H** and 2.5 nm nc-CdS.

Ultrafast transient absorption spectroscopy provides a crucial confirmation of the absence of ET pathways in the sample containing **1-CO_2H** and small nc-CdS. Figure 4.5 contains the full-frequency spectra of an array of probe delay times on this sample. Most notable in these spectra is the lack of the cation radical feature near 630 nm (1.97 eV). The intersystem crossing (ISC) event is still active in this sample and can be seen as a very broad peak near 600 nm, but the familiar shape of a cation radical emerging from the ISC feature is no longer observed.

Figure 4.6 shows nearly an identical set of spectra as was collected previously on **1-CO_2H** alone in solution, and is a simple check to make sure the ultrafast setup is functioning properly. One important difference is that the array of probe delay times in Figure 4.6 is larger than in the previously collected array of spectra. In Figure 4.6 the longest probe delay time is 900 ps, which is much longer than the 500 ps of past

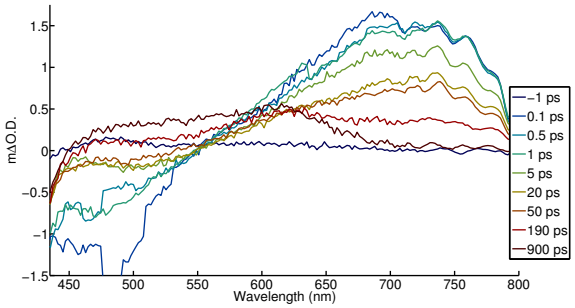

Figure 4.5: Full frequency ultrafast transient absorption spectroscopy results of a sample containing **1-CO_2H** and 1.5 nm diameter nc-CdS in a 1:1 ratio.

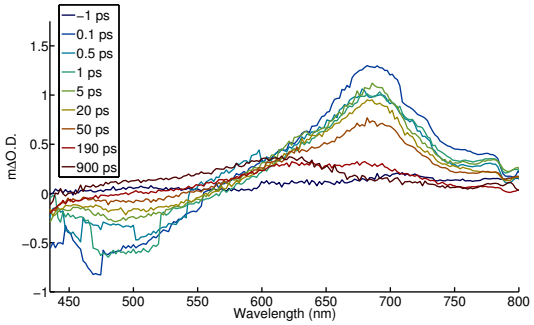

Figure 4.6: Full frequency ultrafast transient absorption spectroscopy results of a sample containing **1-CO_2H** alone.

experiments. The 900 ps probe delay time allows the T_1 signal to develop more strongly.

Comparison between the arrays of spectra in Figures 4.5 and 4.6 reveals a difference in the peak shape of the S_1 feature at 700 nm. In Figure 4.5, this feature is quite broad and probably would be even more broad were it possible to collect spectral data near 800 nm. In the sample containing only **1-CO_2H**, the S_1 feature is much more narrow. It appears that the broadening seen in Figure 2.18c is a result of changing the state of the carboxylic acid group of **1-CO_2H**, in this case to that of a surface-bound carboxylate group.

Figures 4.7 and 4.8 show slices of the full-frequency spectra from Figures 4.5 and 4.6 at 690 nm. These slices should avoid much of the ISC signal and capture the essential dynamics of the S_1 decay pathway. The slices show that the decay of the S_1 state of

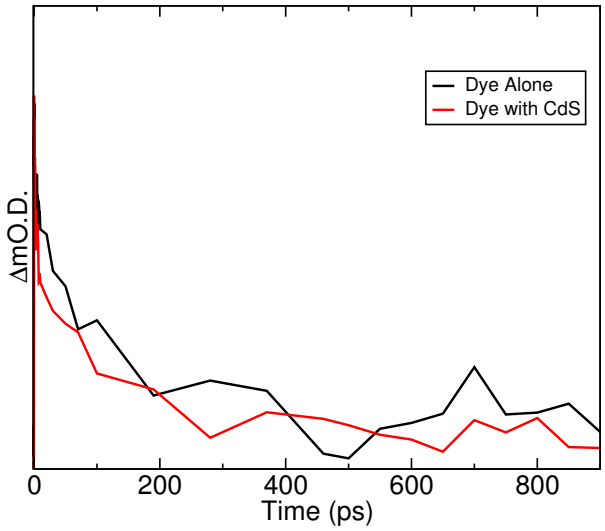

Figure 4.7: Slice at 690 nm from Figures 4.5 and 4.6 showing decay of the dye alone sample compared with the sample of dye and nc-CdS. The comparison between the two plots does not show a systematic difference even when the probe delay times are very long.

the sample with **1-CO_2H** and nc-CdS does not contain fast processes of the type that would indicate ET from **1-CO_2H** to nc-CdS.

4.4 Conclusion

The use of small nc-CdS particles of 1.5 nm diameter has been shown to shut off the ET pathways from **1-CO_2H** to nc-CdS that were formerly available in 2.5 nm nc-CdS particles. This is likely a result of the conduction band's energy shifting to a level that is too high for the excited state oxidation potential of **1-CO_2H**. The dependence of the ET rate (or the presence of an ET channel at all) on the energy of the conduction band suggests that **1-CO_2H** was injecting into the conduction band of 2.5 nm nc-CdS particles in previous experiments.

The equivalence point in the titration of small particles with **1-CO_2H** appears to be roughly 5:1 or 7:1 **1-CO_2H**:nc-CdS. The equivalence point arrives substantially later in the titration than it does in the titration of **1-CO_2H** by 2.5 nm nc-CdS (which arrives

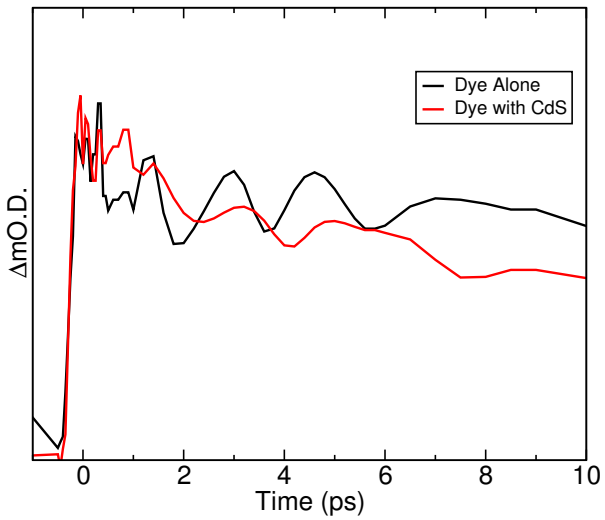

Figure 4.8: Slice at 690 nm from Figures 4.5 and 4.6 showing decay of the dye alone sample compared with the sample of dye and nc-CdS. This array of decay times shows that the short-delay probes do not capture significant sub-10 ps decay processes.

at a **1-CO_2H**:nc-CdS ratio of 20:1). The difference in the maximum coverages is not surprising given that the 1.5 nm particle has roughly 1/3 the surface area that the 2.5 nm particle does.

Spectral differences at the equivalence point can be seen in the level of luminescence at the optimal quench. In titrations using 2.5 nm particles with a 400 nm excitation wavelength the luminescence of the sample at optimum quenching is about eight-fold smaller than that of **1-CO_2H** alone. The same figure for titrations using 1.5 nm particles is much smaller; only about a 30% quench is observed, and this can be explained by alluding to the surface environment of the smaller nc-CdS. From data presented in previous chapters, it seems that there are certain nc-CdS surfaces that are available for **1-CO_2H** adsorption, and it also seems that these surfaces are flat, or nearly flat crystallographic faces. In the situation of a 1.5 nm particle, these surfaces must be smaller than those in the 2.5 nm particle, which would lead to larger interfaces and more adsorbed **1-CO_2H** occupying positions on these interfaces. Such interfacial dyes would have a lower probability of participating in CQ because they would have fewer **1-CO_2H** nearest neighbors, which would make it much less likely that **1-CO_2H** on

the surface of 1.5 nm particles would undergo CQ than **1-CO_2H** on the surface of 2.5 nm particles. Thus the data presented in this chapter are consistent with the overall hypothesis of dye adsorption to specific crystallographic faces.

Chapter 5

Computational and Experimental Studies of Aggregation and Molecular Packing on Nanocrystal Surfaces

Recent experimental data for terthiophene dye molecules grafted to CdS nanoparticles have implicated the formation of dye aggregates in a concentration quenching-based energy loss mechanism.[Vatassery, R. et al., *J. Phys. Chem. C* **117**, 10708 (2013)] Here, molecular dynamics (MD) simulations for terthiophene dye molecules on featureless nanospheres in explicit solvent are used to probe the extent of aggregate formation. The MD simulations reveal onset of dye aggregation at very low coverages, and a structural analysis shows that the extent of concentration quenching is consistent with the fraction of aggregated dyes. The MD simulations and Langmuir fits of the experimental isotherms indicate that limiting coverages are not due to the packing requirements of the dye molecules indicating that some of the CdS nanoparticle surface is not covered by dye molecules.

5.1 Introduction

Dye sensitization, a technology originally developed for color photography,[170,171] has also been investigated for applications in conversion of solar energy to electrical energy.[49,79,82,172] The functional unit that carries out this conversion, the dye-sensitized solar cell (DSSC), is attractive because it can be made with cheap processing methods[79] and abundant raw materials.[20,22] The performance of the DSSC is also better than the more popular crystalline silicon cell in situations where solar energy is incident upon the cell at low angles or low intensities because of its ability to minimize the dark current [82,171]. The dark current, while less detrimental in the DSSC than in silicon cells, is still a problem and reduces fill factor and efficiency. The electrolyte that is needed to complete the circuit between electrodes is a major source of DSSC dark current because it provides a pathway for recombination between conduction band electrons (e_{CB}) in the semiconductor nanoparticles and oxidizing electrolyte species.[6,71,173]

The most recent champion DSSCs have been designed to block access of the electrolyte to the surface of the sensitized nanoparticle in order to eliminate the recombination events that contribute to the dark current and efficiency losses. Many of the designs that achieve this goal rely on bulky, aliphatic chains extending from dye molecules.[21,23–26] There are also examples of planar dye molecules packing together and forming a barrier on their own.[23] While the rates and properties of charge transfer events within these DSSC systems can be measured experimentally, the packing morphologies are not known because of limitations on experimental techniques.

In this article we report a study of the packing efficiency of a model DSSC system applying molecular dynamics simulations using the NAMD software[174] with the CHARMM molecular mechanics force field.[175,176] There are several reports on the ligand morphology of passivated nanoparticles of various types where passivating ligands are alkylthiols or other surfactant molecules.[177–181] However, to our knowledge, there are no reports where this approach has been applied to dye molecules as they pack around the surface of a nanoparticle. In our simulations, the nanoparticle is a featureless sphere but the terthiophene dye molecules and dichloromethane solvent molecules are modeled with full atomistic detail.

The system we study here is similar to a previously reported experimental system

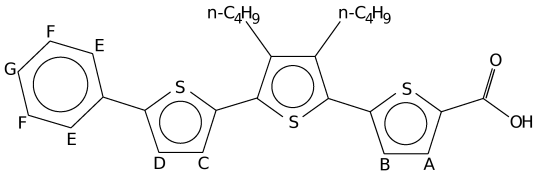

Figure 5.1: The terthiophene dye molecule

where evidence of dye aggregation has been seen.[156] In that system, it was found that a 2.5 nm diameter CdS nanoparticle could accommodate only about 20 terthiophene dye molecules. Assuming a perfectly spherical particle, this corresponds to a surface coverage of 1 nm^2 per dye molecule. Such a large projected area per dye molecule on the surface of the nanoparticle far exceeds the footprint of the dye molecule's fairly small carboxylate head group that is only about 0.16 nm^2 (see Appendix B). This suggests that the surface of the CdS nanoparticle is not completely saturated. Sachleben et al. [124,182] have provided evidence that a similar CdS nanoparticle surface does not reach complete saturation by thiophenol molecules, and that the surface coverage is dependent on the size of the particle. Hence, an opportunity exists to use computational tools to calculate the areal coverage of the entire terthiophene dye molecule to determine if, in the presence of both solvent and thermal energy it requires more space than does the head group, or if there is an insufficient number of sites on the nanoparticle onto which dye molecules can adsorb.

Molecular dynamics simulations were performed probing the packing of the dye molecules around the surface of nanospheres of diameter 1.5 nm, 1.76 nm, and 2.0 nm. These simulations demonstrate that the dye molecules tend to aggregate and can pack much more densely than the experimental evidence suggests, thus we hypothesize that there are islands of dye molecules on the surface of the actual nanoparticles. We use data derived from MD simulations to show that trimers and larger aggregates are likely implicated in the concentration quenching mechanism.

5.2 Methods

5.2.1 Simulation Details

The terthiophene molecule (Fig. 5.1) was modeled using the CHARMM force field parameters.[175,176] In cases where parameters were not available, suitable replacements were found for force constants, and the equilibrium measurements of distances and angles were taken from a B3LYP/6-31G** electronic structure calculation. The adapted parameters can be found in Appendix B. The CH_2Cl_2 molecule was modeled using the OPLS 3-site model,[183,184] which was adapted by using force constants of stretching and bending modes from Cournia et al.[185] All simulations were performed using the NAMD software (Version 2.8).[174]

Initial Configuration of Simulations

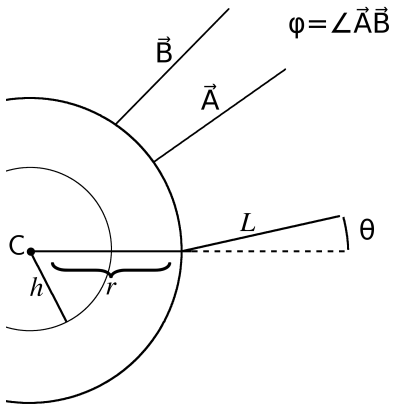

Figure 5.2: Schematic of arrangement of dye molecules around the sphere's surface, where r represents the distance that each carboxylate oxygen sits from the center C of the sphere, h represents the distance that the helium "blocking" atoms sit from C, and L represents the length of a terthiophene dye molecule from head to tail.

Varying numbers (n) of terthiophene molecules were placed around the surface of a

sphere of diameter 1.5 nm that served as a simplified model for the faceted, atomistic nanoparticles probed experimentally. The n terthiophene dye molecules were arranged on the sphere with phenyl groups pointing radially outward, and with the carboxylate oxygens harmonically constrained to a given distance from the center of the sphere (Fig. 5.2). In order to avoid the complications of a limited number of surface binding sites, the carboxylate oxygens sat on a featureless sphere with no discreet binding sites. Inside of the 1.5 nm sphere was a hollow sphere consisting of densely packed helium atoms (i.e. essentially hard spheres) needed to prevent penetration of solvent molecules into the interior of the model nanoparticle. The helium atoms were placed in harmonically constrained positions at a distance h from the center of the sphere (Fig. 5.2), where h is a scalar defined for the 1.5 nm nanosphere as:

$$h = r - r_{\mathsf{vdW}} = 0.75 \text{ nm} - 0.318 \text{ nm} = 0.432 \text{ nm} \tag{5.1}$$

and where

$$r_{\mathsf{vdW}} = \frac{R_{\mathsf{min,O}} + R_{\mathsf{min,He}}}{2} \tag{5.2}$$

In other words, the helium sphere is situated with reference to the outer sphere upon which the carboxylate oxygen atoms sit such that there is no vdW energy gradient from the interaction between helium atoms and carboxylate oxygens. The process described in this paragraph was repeated with spheres of 1.76 nm diameter and 2.0 nm diameter.

As an initial guess, dye molecules were placed on the sphere to maximize the distance from nearest neighbor dye molecules. In order to avoid non-physical superpositions of atoms and molecules arising from the initial guess, the dyes were initially placed further away from the center of the sphere than what the harmonic restraints dictated. Once the minimization of the initial structures started, the harmonic force pulled the carboxylate oxygens to the surface of the nanoparticle (r in Fig. 5.2). The calculations required to space points evenly on the surface of a sphere, and the process used to initially place the dye molecules are both described in Appendix B.

To solvate the ensembles of terthiophene molecules, three separate cubic boxes of m OPLS CH_2Cl_2 solvent molecules were minimized for 1,000 steps, slowly heated to 298 K, and equilibrated, followed by a microcanonical (NVE) production run of 20 ns. The molecular potential energy of the CH_2Cl_2 solvent ($E_{CH_2Cl_2}$) at T=298 K and P=1.013 bar was extracted from this production run by dividing the total potential energy by m.

The nanospheres composed of helium atoms arranged at a distance h from the center of the sphere (Fig. 5.2) were then solvated, minimized, and equilibrated in a similar fashion, followed by a 20 ns production run. The potential energy of the simulation, E_{HeSph}, was extracted from this production run. Finally, n terthiophene molecules were superimposed onto this structure and solvent molecules which were overlapping or close to overlapping with terthiophene molecules were moved outwards to the edges of the periodic box. The minimization of n terthiophene dye molecules around the solvated sphere proceeded for 10,000 steps, after which the temperature was slowly raised to 298 K at constant pressure (P=1.013 bar) and the system was allowed to equilibrate. A 20 ns production run was performed for each increment n, and the total potential energy, $E_{\mathrm{FS}}(n)$, was extracted from these production runs. Lastly, a single terthiophene dye molecule was solvated, minimized, allowed to equilibrate, and subjected to a production run of 20 ns. We refer to the potential energy of this simulation as E_{DyeSol}.

In order to calculate the energy of interaction (E_{int}) between terthiophene dye molecules in an ensemble, all other contributors to the total energy are subtracted out. Eq. 5.3 shows the process of removing the various contributors to the potential energy:

$$E_{\mathrm{int}}(n) = E_{\mathrm{FS}}(n) - E_{\mathrm{HeSph}} - nE_{\mathrm{DyeSol}} + nmE_{\mathrm{CH_2Cl_2}} \tag{5.3}$$

where n is the number of terthiophene dye molecules, and m is the number of CH_2Cl_2 molecules. Because $\mathrm{E_{int}}(n)$ is dependent on n, $\mathrm{E_{int}}(n)$ is divided by n from here on, and reported as potential energy.

5.2.2 Langmuir Isotherm

Oleate-capped cadmium sulfide nanocrystals were synthesized as previously reported,[95] with minor modifications as previously reported.[156] The terthiophene dye, 3',4'-dibutyl-5"-phenyl-[2,2':5',2"-terthiophene]-5-carboxylic acid, was also synthesized by the reported method.[120]

The steady-state emission spectra were recorded through two Spex Fluorolog 1680 0.22 m double spectrometer gratings equipped with a 450 W xenon source. All spectroscopy was performed in front-face mode with quartz cuvettes with a 3 mm path length in CH_2Cl_2.[156]

The experimental data to be fit using the Langmuir isotherm model was produced using a standard solution containing terthiophene dye in CH_2Cl_2, and another standard solution containing nc-CdS in CH_2Cl_2. Aliquots of the dye solution were dispensed into vials in two equivalent arrays with increasing amounts of terthiophene dye, from 5.8×10^{-9} mol up to 1.75×10^{-7} mol. One set of aliquots was left as is, and to the other array of aliquots was added 8.7×10^{-9} mol nc-CdS per vial from the standard solution. The linear regime of fluorescence of the terthiophene dye versus concentration in CH_2Cl_2 is from 0 M to 2.0×10^{-4} M, and the highest concentration of terthiophene dye used was 1.67×10^{-4} M. At the time of fluorescence measurement, each solution had a total volume of 700 μL.

The fluorescence of the array with only terthiophene dye (F_{DA}) was subtracted by the fluorescence of the array containing nc-CdS ($F_{\mathrm{D:CdS}}$), and dividing this difference by F_{DA} gave the fraction of bound dye (χ_{BD}), according to Eq. 5.4.

$$\chi_{\mathrm{BD}} = \frac{F_{\mathrm{DA}} - F_{\mathrm{D:CdS}}}{F_{\mathrm{DA}}} \tag{5.4}$$

The calculation in Eq. 5.4 assumes that all dyes that are fluorescing are unbound and all that are bound are no longer fluorescing. This is not always the case, but at the best quenching levels in the present system comprised of terthiophene dye adsorbed to nc-CdS there are only one out of eight dyes that are bound but still fluorescing. The calculation of the size of the nanoparticle, along with the concentrations of various nc-CdS dispersions are based on empirical fits that have been previously reported.[104] The surface area of the nanoparticle (SA_{NP}) is calculated by assuming a spherical shape. Using Eq. 5.5, the coverage for each sample is calculated:

$$\theta_{\mathrm{c}} = \frac{n_{\mathrm{D}} \chi_{\mathrm{BD}} (0.16 \mathrm{nm}^2)}{n_{\mathrm{NP}} SA_{\mathrm{NP}}} \tag{5.5}$$

where n_{D} is the number of dye molecules, n_{NP} is the number of CdS nanoparticles, and the 0.16 nm^2 factor is the area of the carboxylate head group (Appendix B). After θ_{c} is calculated from Eq. 5.5, a plot of it versus concentration of terthiophene dye can be created and fit to the Langmuir model:

$$\theta_{\mathrm{c}} = \frac{K[\mathrm{dye}]}{1 + K[\mathrm{dye}]} \tag{5.6}$$

from which the value of K can be extracted.[186]

5.2.3 Stern-Volmer Experiment

The Stern-Volmer experiment was run previously,[156] and the data is plotted in Fig. 5.3. This data shows a peak at the ratio of dye:nc-CdS of 20:1, and this peak has been previously attributed to an aggregation-induced concentration quenching mechanism that is in addition to the electron transfer pathway that is operative at lower dye:nc-CdS ratios. Thus we can deduce the amount of aggregation in the sample based on the amount of concentration quenching present. The amount of concentration quenching present in the samples with ratios between 1:1 (dye:nc-CdS) and 20:1 is simply taken to be the amount of quenching observed above the 1:1 sample (where electron transfer has been shown to be dominant). This means that quenching levels higher than 2.5 in the 400 nm experiment and 2.25 in the 420 nm experiment are attributed to concentration quenching. To compare with simulation data, the data in Fig. 5.3 are subtracted by either 2.5 (400 nm data) or 2.25 (420 nm data), and then normalized so that the highest point (the 20:1 sample point) corresponds to a y-value of 1.

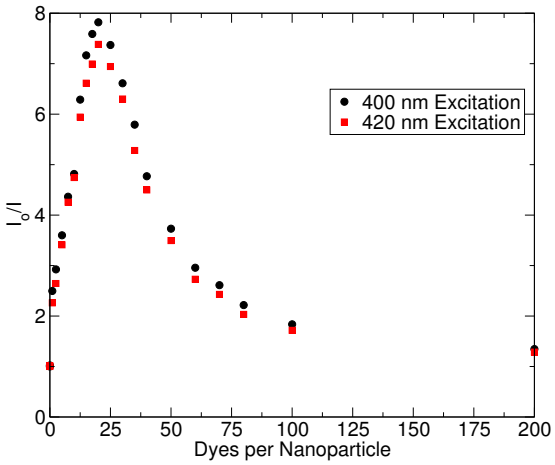

Figure 5.3: Depiction of Stern-Volmer experiment with the usual x-axis units of concentration of quencher being replaced in favor of the ratio of dyes to nc-CdS. The black circles and red squares come from the same samples. The black circles were run with a 400 nm excitation wavelength while the red squares were run with a 420 nm excitation wavelength.

5.3 Results and Discussion

5.3.1 Langmuir Isotherm

The Langmuir isotherm,[186] a model for fitting titrations of surface adsorption sites with adsorbates, has been used previously [170,187–189] to determine binding constants of dye molecules to metal-chalcogenide surfaces. The binding constant, K, can then be used to calculate the free energy of binding using Eq. 5.7:

$$K = \mathrm{e}^{-\frac{\Delta G}{k_{\mathrm{B}}T}} \tag{5.7}$$

In the case of terthiophene dye attaching via the carboxylic acid functional group to the surface of the CdS nanoparticle, the equilibrium constant for binding and free energy of binding are 35000 and -6.2 kcal/mol, respectively. The reliability of these numbers is diminished by the fact that some of the assumptions of the Langmuir isotherm are not strictly valid. For example, the inhomogeneity of the surface, interactions between molecules on the surface, and the relatively high concentration of molecules in solution all mean that the numbers which we call the "equilibrium constant for binding" and "free energy of binding" are approximations for these quantities.[164]

The previous discussion taken into consideration, the fit to the Langmuir Isotherm is reasonable. The binding energy of roughly -6.2 kcal/mol means that, in the first approximation where an excess of equivalent binding sites is assumed to exist, the steric energy between the (n) dyes adsorbed to the surface and the $(n{+}1)^{\mathrm{th}}$ dye must exceed $\sim$6.2 kcal/mol. If steric strain does not destabilize the monolayer of adsorbed dyes to this extent, then it can be reasoned that the binding energy will provide sufficient energetic impetus for the $(n{+}1)^{\mathrm{th}}$ molecule to adsorb. Thus the $\sim$6.2 kcal/mol level is denoted in the subsequent graphs featuring potential energy versus number of terthiophene dye molecules with a dashed line, as it is the most steric energy that can be offset by the binding energy.

In addition to the "free energy of binding" that can be deduced from the fit to the Langmuir isotherm model, we can also see from the titration of theoretical surface sites with dyes that the surface coverage does not appear to approach full saturation. Full saturation is characterized by the surface coverage nearing a value of 1 on the y-axis. From the fit derived from this Langmuir isotherm, it appears that the surface carries

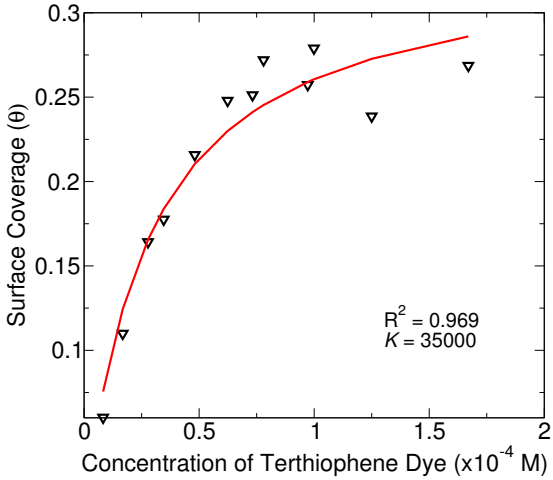

Figure 5.4: Langmuir isotherm showing coverage dependence on concentration of terthiophene dye molecules. The fit produces an "equilibrium constant for binding" of 35000 with a correlation coefficient of 0.969. The fit to the data shows that the nc-CdS surface carries only about 1/3 of the dye molecules that should be able to adsorb to the surface with the sizes of the terthiophene dye and the nanocrystal.

only about 1/3 of the dye molecules that could fit according to the parameters we have chosen. If the points towards the high-concentration end of the isotherm were weighted more heavily in the least-squares fitting of the data, this fraction would be even lower. There are two reasons that the coverage on the surface studied here is low: the dye could be too bulky to be accommodated in larger numbers, or the nanoparticle's surface may not contain sufficient binding sites for the dye to saturate it every 0.16 nm^2. The simulations described in the next section are intended to identify which of the reasons is correct.

5.3.2 Classical Mechanical Simulations

Experimental measurement of steric bulk is not straightforward, but this problem can be approached using atomistic simulations. Classical molecular dynamics (MD) simulations with suitable molecular mechanics force fields can correctly reproduce the experimental densities of most solvents, meaning that these simulations accurately capture the interplay between thermal energy, intermolecular forces, and steric bulk. This includes the

OPLS parameter set for the CH_2Cl_2 solvent that is used in this study.[183]

The potential energy (Eq. 5.3) of the system as reported here is mostly a function of the non-bonded Lennard-Jones and electrostatic interactions because harmonic bond stretching and angle bending modes generally contain energy equivalent to $\frac{1}{2}k_{\mathrm{B}}T$. The entire ensemble's potential energy is not as useful, because it will increase or decrease in proportion to n, the number of terthiophene molecules. To correct this problem, we report the average potential energy obtained from Eq. 5.3 divided by n, as was mentioned above.

Comparison with Previous Experimental Data

In addition to the Langmuir isotherm experiment, Stern-Volmer-type experiments were carried out in a previous publication discussed above.[156] In the latter experiment, a set concentration of terthiophene dye was titrated with a stock dispersion of nanocrystalline CdS of diameter 2.5 nm, and it was found that the maximum number of terthiophene dye molecules that could exchange onto the surface of these nanoparticles falls into the range from 20-25 (Fig. 5.3). Fig. 5.5 shows the results of classical mechanical simulations as potential energy of interaction (E_{int}) is plotted versus number of terthiophene molecules around three different sized nanospheres. It can be seen that, in contrast to the experimental data showing a limitation of 20-25 dye molecules on the surface of a CdS nanoparticle of 2.5 nm diameter, even a sphere of 1.5 nm diameter is capable of accommodating more terthiophene dye molecules around its surface. For the largest size nanosphere used in this study, E_{int} does not exceed 6.2 kcal/mol until almost 85 terthiophenes are placed on the surface, suggesting that the dye molecules' steric bulk is not the limiting factor in adsorption to CdS surfaces.

Recasting the data from Fig. 5.5 to make a plot of E_{int} versus the surface area per terthiophene molecule produces Fig. 5.6. Observing the point where the potential energy exceeds the 6.2 kcal/mol value in Fig. 5.6, a value of area per terthiophene molecule can be seen that is smaller than, but close to, the theoretical value of 0.16 nm^2/molecule that was described in the Introduction. This means that the head group in the terthiophene dye molecule is a major limiting factor in packing of the dye molecules around the surface of the nanospheres studied here. It appears that the dye molecules' n-butyl functional groups do not significantly interrupt the packing of the dyes on the surfaces

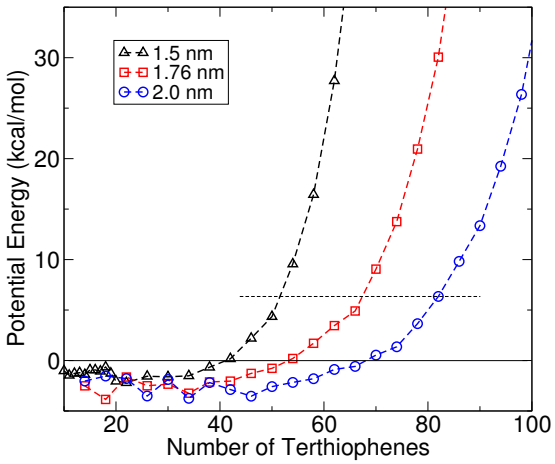

Figure 5.5: Potential energy of interaction (E_{int}) as function of the number of terthiophenes placed on a sphere of a given radius. The dashed line indicates 6.2 kcal/mol, the point at which the binding energy may not be able to overcome steric repulsions.

we have studied. It is expected that as the radii of the spheres to which the dyes are attached grows, the butyl functional groups will become more relevant in the packing efficiency.

Plotting the areal coverage values at which the data sets in Fig. 5.6 cross the dashed line yields Fig. 5.7. A trend where dye molecules are able to pack more closely on smaller nanospheres is visible in Fig. 5.7. This is because the higher curvature of a smaller nanosphere reduces interactions at a given distance from the nanosphere's surface. Fig. 5.7 also shows this trend is not linear. Non-linearity in plots of maximum coverage versus diameter of particle is expected because at very low curvature such as is found in large particles or flat surfaces, the dye should approach a limiting value of surface coverage density. In the case of alkylthiol molecules adsorbed to gold surfaces, this has been previously reported to be slightly larger than 0.20 nm^2/molecule for nanoparticles and planar surfaces.[190,191] The non-linearity that is observed in Fig. 5.7 may be a result of the *n*-butyl groups playing a larger role as curvature decreases.

If we define a monolayer as the number of molecules required to cover the surface of a nanosphere such that the potential energy of interaction, E_{int}, reaches 6.2

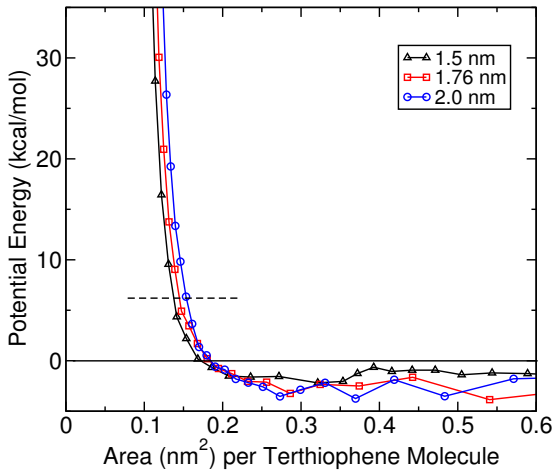

Figure 5.6: Potential energy as area per terthiophene molecule is increased. This is the same potential energy data as in Fig. 5.5, with x axis values changed.

kcal/mol we can see the density of such a monolayer is much higher than experimentally observed. For the 1.5 nm, 1.76 nm, and 2.0 nm spheres, the areal coverage per terthiophene dye molecule and the number of molecules in the complete monolayer are 0.138 nm^2/molecule and 50 molecules, 0.145 nm^2/molecule and 66 dye molecules, and 0.153 nm^2/molecule and 82 molecules, respectively. Compared with the area per terthiophene molecule obtained experimentally of 1 nm^2/molecule,[156] these coverages are much more dense. Thus the computational data supports the argument that the dye's steric bulk is not limiting adsorption, and that the nanoparticle's surface must be the limiting factor.

Morphology Analysis

Figs. 5.8 and 5.9 display the angular pair distribution function (PDF) and the Cartesian distance PDF, respectively, for the carboxylate head groups, where the carboxylate carbon is the basis for these measurements. Fig. 5.8 shows that the onset of the angular PDF is regular across the range from 1/4 of a monolayer, up to a full monolayer coverage. The x-axis value of the valleys after the first peak in Fig. 5.8 are 45°, 41°, and 36° for sphere sizes of 1.5 nm, 1.76 nm, and 2.0 nm, respectively. Fig. 5.9 shows that the onset of the Cartesian PDF's peak is similarly regular across the range of 1/4

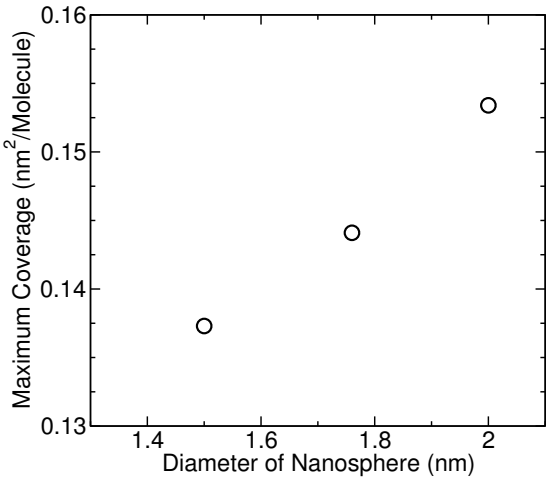

Figure 5.7: Plot of maximum coverage (area/molecule) as the diameter of the nanospheres increase. The maximum coverage is found by calculating the value at which the respective potential energy curves cross the dashed line at 6.2 kcal/mol in Fig. 5.6.

of a monolayer up to a full monolayer, and that the valley in the data occurs at roughly 0.65 nm.

Figs. 5.10 and 5.11 are analogous to Figs. 5.8 and 5.9, with the exception that in the case of Figs. 5.10 and 5.11 the PDF is calculated on the phenyl group at the other end of the molecule from the head group. A center of mass is computed for the six carbons in the phenyl ring and this is used as the basis for the PDFs in Figs. 5.10 and 5.11. The phenyl group's PDF is important because NMR experiments previously reported showed that the aggregation-induced energy losses could be predicted by the loss of the phenyl groups' NMR signals, which we believe to be a result of $\pi - \pi$ stacking amongst phenyls.[156] As with the PDFs based on the head groups, the PDFs based on the phenyl groups are similar across the sizes of nanospheres that were studied. In addition, the onsets of the first peaks in the graphs are regular across the range from 1/4 of a monolayer to a full monolayer.

That the sets of data in Figs. 5.8, 5.9, 5.10, and 5.11 show a very similar picture across sizes of nanospheres is noteworthy. It signals that the morphologies of the simulations at 1/4, 1/2, 3/4, and a full monolayer bear resemblance to one another in spite

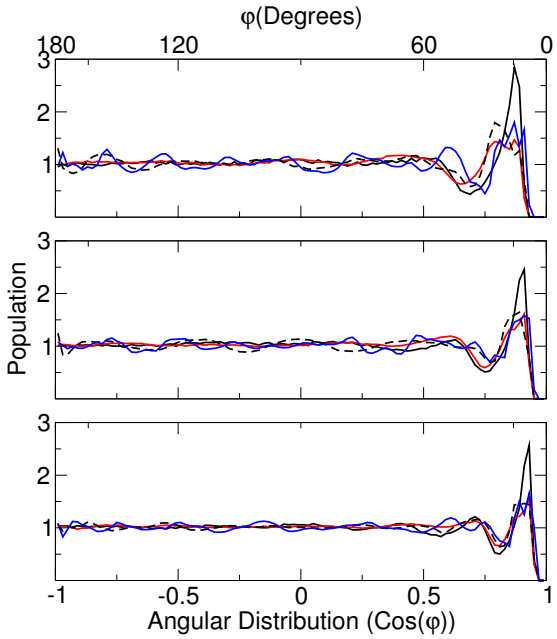

Figure 5.8: Plots showing the angular PDF of head groups on spheres of diameter 1.5 nm (top), 1.76 nm (middle), and 2.0 nm (bottom). In all graphs 1/4 of a monolayer is solid black, 1/2 monolayer is red, 3/4 monolayer is dashed black, and the full monolayer is blue.

of the fact that they contain different numbers of molecules around differently-sized nanospheres.

The uniformity of the onset of the first peaks in the above graphs (Figs. 5.8 to 5.11) shows that at low surface coverage of dye molecules on the nanosphere the dye molecules can translate around the surface of the sphere to interact with other dye molecules. If the solvent contained in the simulations or the experimental systems is a bad solvent, the molecules will randomly walk on the sphere's surface and, upon encountering other dye molecules, form n-mers (dimers, trimers or larger aggregates). If the solvent is a good solvent, the molecules will randomly walk in a similar fashion, but upon encountering other dye molecules, they will form associations with one another that are not stronger than the associations the dye molecules form with the solvent molecules. This will result in n-mers being dissolved on the surface as quickly as they are formed. Experimentally in the case of terthiophene dye on the surface of a nanoparticle in the presence of CH_2Cl_2,

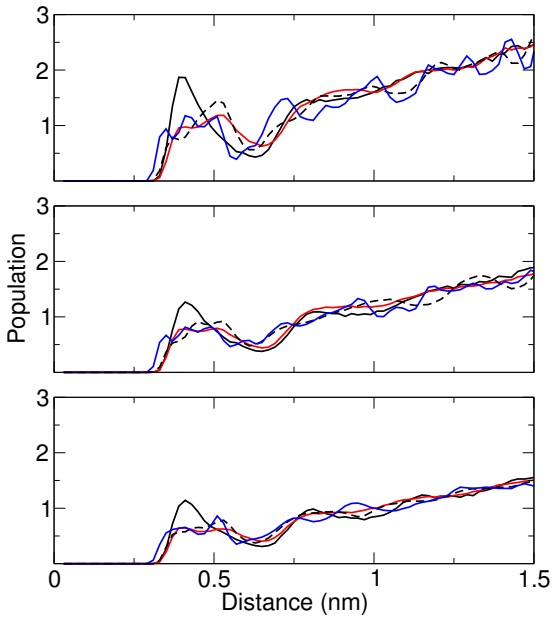

Figure 5.9: Plots showing the Cartesian PDF of head groups on spheres of diameter 1.5 nm (top), 1.76 nm (middle), and 2.0 nm (bottom). In all graphs 1/4 of a monolayer is solid black, 1/2 monolayer is red, 3/4 monolayer is dashed black, and the full monolayer is blue.

aggregates can be seen in UV-Vis and NMR spectroscopies — thus the CH_2Cl_2 solvent is not a sufficiently good solvent to break up surface-templated aggregates.[156] Aggregates should then be observed in our simulations at low surface coverage as a result of dye molecules' ability to traverse the sphere's surface and form n-mers. Fig. 5.12 shows images of the dye molecules forming such aggregates at low surface coverage.

Analysis of a more representative sample size yields Fig. 5.13, which shows the presence of monomers quickly decreases as coverage increases. Here, the term "aggregate" as it pertains to the simulations is defined as a group of any number of terthiophene molecules that are closer to each other than the position of the valley after the first peak in Figs. 5.9 and 5.11. For measurements based on the carboxylate head group, the carboxylate carbons must be within 0.65 nm of one another to be defined as aggregating and for measurements based on the phenyl tail-group the center of the phenyl ring must be within 1.3 nm of one another. Monomers are defined as molecules that do not fit

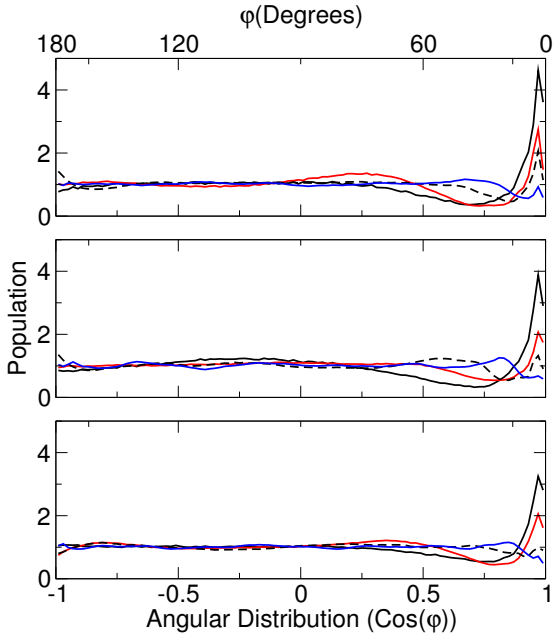

Figure 5.10: Plots showing the angular PDF of phenyl groups on spheres of diameter 1.5 nm (top), 1.76 nm (middle), and 2.0 nm (bottom). In all graphs 1/4 of a monolayer is solid black, 1/2 monolayer is red, 3/4 monolayer is dashed black, and the full monolayer is blue.

the criteria outlined above. Fig. 5.13 also shows that, while there is a slight difference between the tendencies of aggregation on the three differently-sized nanospheres, the terthiophene dyes behave fairly similarly on the surfaces of nanospheres of vastly different sizes. This, along with the fact that the nc-CdS surface does not seem to be completely saturated by terthiophene dyes and therefore has less surface area than it would otherwise, means that the smaller nanospheres used in these studies to make the computations tractable are still representative of the experimental system.

Evidence of aggregate formation at low coverage can also be found in the distribution of mutual angles φ, where φ is defined in Fig. 5.2. The distribution in question was restricted to those molecules whose headgroups were within 0.65 nm, and the distribution was scaled such that a randomly oriented population has a value of 1 throughout the range of angles. Analysis of the distributions of a few increments of surface coverage, seen in Fig. 5.14, provides additional insight into the morphology of the ligand

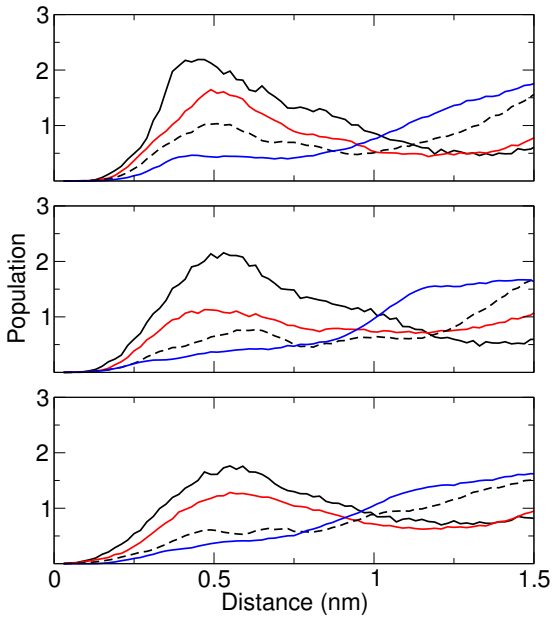

Figure 5.11: Plots showing the Cartesian PDF of phenyl groups on spheres of diameter 1.5 nm (top), 1.76 nm (middle), and 2.0 nm (bottom). In all graphs 1/4 of a monolayer is solid black, 1/2 monolayer is red, 3/4 monolayer is dashed black, and the full monolayer is blue.

environment. At low surface coverages the dye molecules are generally close to parallel with their nearest neighbors. However, in addition to the large peak at 0° representing the preference for most terthiophene molecules to align in parallel, the smaller, broad features near 70° in Fig. 5.14 show that some molecules deviate significantly from parallel with some of their nearest neighbors. This results from interfaces forming between separate islands of aggregated dyes on different sectors of the sphere's surface. Support for the hypothesis that the feature at 70° in Fig. 5.14 arises from interfaces forming between islands of aggregates comes from the fact that the height of the 70° feature decreases as the nanoparticle becomes larger. This is expected because the curvature of the larger particles is less thus the interfaces should not only be less numerous, but the aggregated islands should also have smaller mutual angles with each other.

Increasing surface coverage has the expected effect of coalescing all the islands of

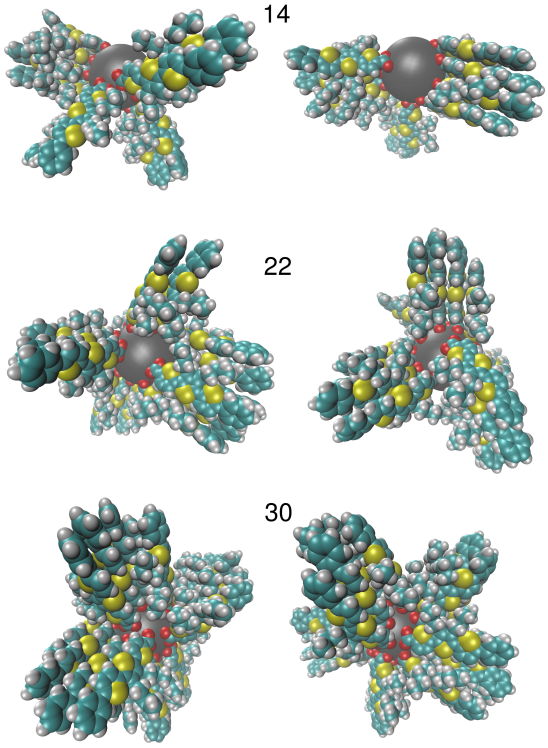

Figure 5.12: Dye molecules adsorbed to the surface of a sphere with diameter 1.5 nm. The top two images show 14 dyes around the sphere, the middle two show 22, and the bottom two show 30. The gray spheres shown are for visualization purposes, and have a diameter of 1.5 nm.

aggregates into one large aggregate. This eliminates the large angles from the distribution of φ, as seen in Fig. 5.14 where the higher coverages no longer have broad features around 70°. The presence of a sizable peak appearing around 30° at these higher surface coverages results from poor packing around the surface of a sphere. This is against the trend of a more orderly and efficient packing (where one would expect all parallel orientations amongst nearest neighbors), but it is logical that dye molecules at high coverages have several nearest-neighbors with which they can pack together and form small aggregates, thereby creating opportunities for dyes to be oriented away from parallel with neighbors. Also, the curvature of the surface of the nanosphere limits the packing efficiency at high surface coverages, and it is not as good as would be seen in

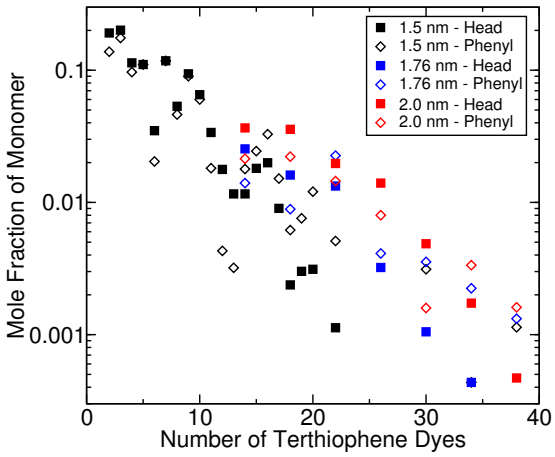

Figure 5.13: Graph showing the mole fraction in log units of monomers (unaggregated dyes) as a function of number of terthiophene molecules around the surface of a sphere. Black, blue, and red squares and diamonds correspond to the 1.5 nm sphere, the 1.76 nm sphere, and the 2.0 nm sphere, respectively. Squares indicate that the measurement is based on the head group and diamonds indicate the measurement is based on the phenyl tail-group.

flat surfaces. This point has been brought up before in reference to singularities forming on spherical surfaces.[177,192]

The distribution of angles θ, where θ is defined in Fig. 5.2 paints a similar picture. At low coverages of dye molecules the angles can take large values, meaning that the molecules are significantly off surface-normal. As the surface coverage increases and the area per terthiophene molecule decreases, the molecules pack together more efficiently. This increase in packing efficiency can be seen in Fig. 5.15, where as the packing density increases, θ also becomes smaller (as evidenced by the value of the cosine function approaching 1). Upon reaching a fairly small angle from surface normal, or roughly $\cos(\theta) = 0.95$, the packing efficiency cannot increase further. At this point, the potential energy (Fig. 5.6) grows and eventually exceeds the quantity where the binding energy can be expected to overcome. Computations were carried out to very large surface coverages, and the energies increased with increasing surface coverage.

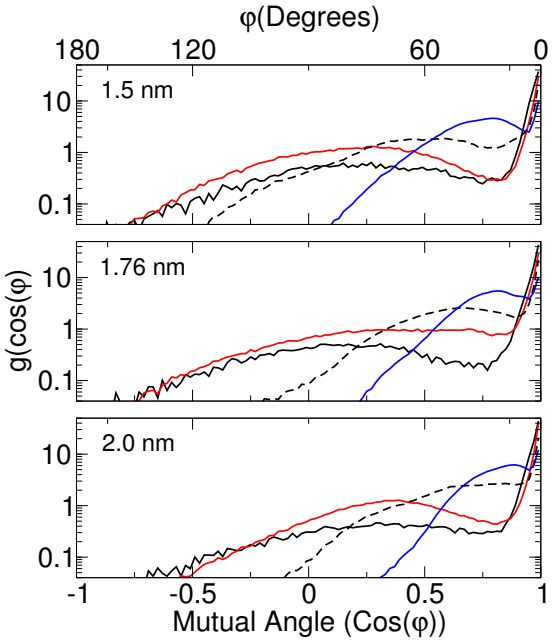

Figure 5.14: Log-scale histogram describing distribution of cosine of mutual angles φ, defined in Fig. 5.2, for spheres of diameter 1.5 nm (top), 1.76 nm (middle), and 2.0 nm (bottom). The distributions were scaled such that a random distribution would give a value of 1 for each value of $\cos(\varphi)$. In all graphs 1/4 of a monolayer is solid black, 1/2 monolayer is red, 3/4 monolayer is dashed black, and the full monolayer is blue.

5.3.3 Simulation Data Versus Experimental Data

In addition to providing a measurement of the packing efficiency of the terthiophene dye on the nanosphere surface and providing a glimpse into the morphology of the surface environment, the simulations can also be used to compare the propensity of aggregation predicted by the CHARMM parameter set with the experimentally observed aggregation. If the simulation-based data matches well with the experimental data, it not only lends credence to the simulation model, but it also gives additional opportunity to extract information from it.

The experimental data that is best suited for a comparison with our simulation data is in the form of a Stern-Volmer experiment, where the coverage of dye molecules on a surface of nc-CdS is decreased by increasing the available nc-CdS surface with the

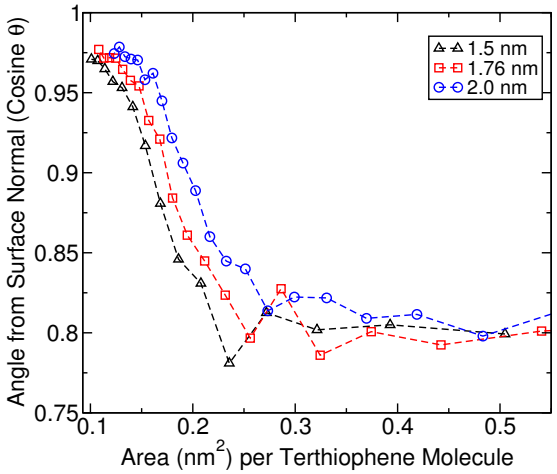

Figure 5.15: Average values of cosine(θ) as area per terthiophene is increased. θ, defined in Fig. 5.2, represents the angle that a terthiophene dye molecule takes from the surface normal.

concentration of dye kept constant. Isolating the concentration quenching component of the fluorescence quenching (as described in section 5.2.3) allows for analysis of only the contribution of the quenching which arises from aggregation. This in turn allows us to study the aggregation of the dyes in the experimental system.

Fig. 5.16 shows the comparison between the experimental data and the data derived from simulations. When plotted against the fraction of dimers and higher-order aggregates (red diamonds in Fig. 5.16), the experimental data do not correlate. However, plotted against trimers and higher-order aggregates (black squares), the experimental data show a good match. From these observations we propose that lone dimers do not contribute significantly to the aggregation-induced quenching processes, but trimers and higher-order aggregates are effective in this role. We suspect that the dimers are too transient to be a major factor in the concentration quenching pathway.

In addition to a comparison of the experimental data with simulation-derived data, we have also found agreement between the experimental data and a combinatorial method that we developed to model aggregating dyes in a purely mathematical formulation.

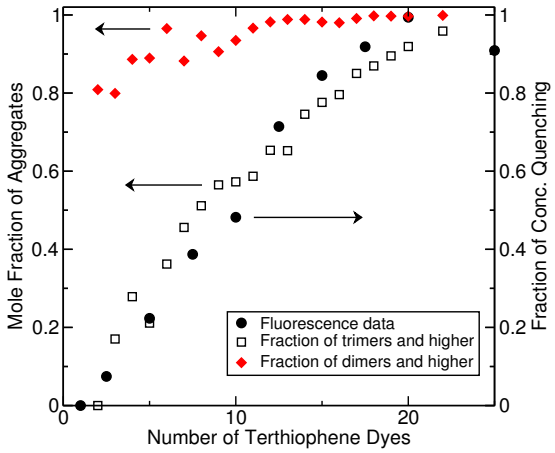

Figure 5.16: Fraction of aggregates as number of terthiophene dyes is increased around the 1.5 nm sphere, compared with the fraction of concentration quenching that is observed experimentally.

5.4 Conclusions

In this report, we present experimental evidence in the form of a Langmuir isotherm that suggests the surface of the CdS nanocrystal as synthesized previously[95] in the presence of carboxylic acid-bearing dye molecules is undersaturated. Specifically, we find that the Langmuir isotherm model, when fit to our data, shows that the number of dye molecules per nc-CdS is roughly 1/3 of what it should be if we assume a spherical surface of the nc-CdS and a head group size of 0.16 nm^2 for the terthiophene dye. This limitation of the saturation of the nc-CdS surface by terthiophene dyes was also observed in a previous report.[156] Simulations were conducted to determine what was the source of the limitation of terthiophene dye molecules on the surface.

The classical MD simulations show that the steric bulk of the dye molecule is not the factor limiting the dyes' surface coverage of the CdS nanoparticles. Questions remain regarding the origin of the limitation of the dye molecules' adsorption onto the CdS surface. During synthesis of CdS nanocrystals[95], oleate surfactant molecules adsorb to the surface of the CdS. These surface-passivating molecules serve to prevent aggregation and further growth, and must be replaced in order for the terthiophene dye to

completely saturate the available Cd^{2+} binding sites. It is possible that some passivating surfactant molecules attach too strongly to specific sites on the nanoparticle surface for a replacement reaction to occur. Literature precedent of this type of phenomenon exists in the alkylthiol-gold nanoparticle literature, where Hostetler et al.[193] showed that certain surface sites readily undergo ligand-exchange while others do not undergo these reactions under normal conditions.

Alternatively, the limitation of coverage of CdS nanocrystalline surface by terthiophene dye molecules could be due to a scarcity of surface sites suitable for attachment to any carboxylate functional group. This could arise from a surface excess of sulfur atoms which likely are not able to bind to carboxylates, or a predominance of crystallographic faces with hindered Cd^{2+} sites. Sachleben et al.[124,182] and Antoun et al.[116] presented research that is supportive of this hypothesis. In studies on thiophenol surface-adsorption to CdS nanoparticles, Sachleben et al. reported that the thiophenol molecule does not reach complete saturation on CdS surfaces. Based on their NMR studies the surface of the CdS nanoparticle is covered by islands of thiophenol ligand.[124,182] Antoun et al. showed that when using the terthiophene molecule as a capping ligand, one still calculates that roughly 20 terthiophene dye molecules fit around the surface of the nanocrystal of similar dimensions. This is notable because of the lack of pre-existing capping ligand that Antoun et al. used in their synthesis — the terthiophene acid was the surfactant used in their synthesis to arrest agglomeration and growth.

These simulations provide a framework for a similar study of other dye molecules such as the ruthenium coordination compounds that are much more bulky. In the case of these ruthenium-based molecules, their steric bulk may indeed be the limitation to their adsorption onto metal-chalcogenide surfaces, and we aim to study these complexes in the future. We also plan to extend the detail of the nanoparticle surface to make it contain the correct atomic detail.

Chapter 6

Combinatorial Analysis Modeling of Aggregation

6.1 Introduction

Aggregation amongst dye molecules on the surface of nanoparticles has been shown to cause the concentration quenching phenomenon seen at high surface coverages in the PL experiments.[156] Spectral signatures of aggregation can be seen in the UV-Vis, ultrafast TA spectroscopy, and NMR in the samples where high surface coverages are expected.

Studies of aggregates are generally limited to the spectral analyses mentioned above. These analyses can provide clues as to when aggregation is occurring, but an effective model does not appear to exist for this phenomenon. Given the evidence presented heretofore in this thesis that suggests carboxylate adsorbates are confined to particular crystallographic faces, a very simple model of the nanoparticle surface with discrete surface binding sites on a planar surface may be useful as a model for aggregation in this environment.

Combinatorial mathematics[194] is the branch of mathematics that will be most useful to us in creating this model. Using generating functions to describe components of the crystallographic faces presented to the carboxylate adsorbates (in this case, the terthiophene dye, **1-CO$_2$H**) creates the simplified picture that we can use to guide our research forward. Using these generating functions, we have developed a mathematical

model describing the probability of aggregation amongst dyes on the nanoparticle surface. The goal of the model is to calculate the relative population of aggregates versus unaggregated monomers as a function of the number of molecules on the nanoparticle surfaces. We then compare this model to the fluorescence quenching data of the region in which concentration quenching, and therefore aggregation, is active.

6.2 Methods

6.2.1 Combinatorial Analysis

Theoretical analysis was carried out using combinatorial methods, wherein the nanoparticle surface was approximated to be a flat grid of binding sites to which dye molecules could attach. Because the dye molecule is planar, we chose to consider only N-S contact as aggregation. That is to say, we restricted our description of aggregation to being only 1 dimensional.

The grid to approximate the surface of the nanoparticle was chosen to be 4x5. This means that we were able to take four 1x5 N-S strips of the grid, using generating functions to carry data about the different possible configurations on a strip. Out of the 32 possible ways to fill a 1x5 strip ($2^5 = 32$), 5 generating functions, f_1, f_2, f_3, f_4, and f_5 were calculated:

$$f_1 = 1 + 5t + 5t^2, f_2 = 5t^2 + 5t^3, f_3 = 5t^3, f_4 = 5t^4, f_5 = t^5. \tag{6.1}$$

These generating functions encode the degree of aggregation in each N-S strip as a function of the number of molecules present in each strip. For example, f_1 corresponds to a strip having no aggregation, and can be described by 1 distribution with zero molecules, 5 distributions with 1 molecule, and 5 distributions with two molecules. The function f_2 similarly describes a strip with only a dimer, and there are 5 distributions with 2 molecules and 5 distributions with three molecules that satisfy this situation. It can be seen from these examples that the exponent represents the number of molecules in the configuration.

The generating functions are then combined into function **F**:

$$\mathbf{F} = \sum_{a_1=0}^{C} \sum_{a_2=0}^{C} \sum_{a_3=0}^{C} \sum_{a_4=0}^{C} f_1^{a_1} f_2^{a_2} \dots f_4^{a_4} \binom{4}{a_1, a_2, a_3, a_4, a_5} M, \tag{6.2}$$

where a_i is the number of instances of each situation f_i occurring in the 4x5 grid, bound by the fact that there are four strips:

$$4 = a_1 + a_2 + a_3 + a_4 + a_5, \tag{6.3}$$

and $\mathbf{F}$ is scaled by M, where

$$M = 2a_2 + 3a_3 + 4a_4 + 5a_5. \tag{6.4}$$

Clearly, M accounts for the fact that in an n-fold aggregate, there are n dye molecules and the probability of picking a dye from this aggregate should be scaled by the number of dyes aggregated. $\mathbf{F}$ is an expanded polynomial that, because it is composed of generating functions (Eq. 6.1), contains information in its coefficients that describes the possible distributions of n molecules distributed randomly across S binding sites, where $S = 4 \times 5$. The expanded form of function $\mathbf{F}$ and the 32 microstates that led to the generating functions can be seen in Equation 6.5.

$$\begin{aligned}\mathbf{F} = \quad & 25t^{25} + 600t^{24} + 6875t^{23} + 50050t^{22} + 259875t^{21} + 1024100t^{20} + 3182025t^{19} + \dots \\ & 7994250t^{18} + 16521450t^{17} + 28424000t^{16} + 41037150t^{15} + 49968100t^{14} + \dots \\ & 51437750t^{13} + 44767800t^{12} + 32865250t^{11} + 20252100t^{10} + 10392525t^{9} + \dots \\ & 4389000t^{8} + 1499575t^{7} + 404250t^{6} + 82775t^{5} + 12100t^{4} + 1125t^{3} + 50t^{2}\end{aligned} \tag{6.5}$$

The probability of randomly picking a dye molecule that was part of an aggregate as a function of number n of molecules on the grid is

$$\mathbf{P}_n = \frac{\mathbf{F}_n}{n\binom{S}{n}} \tag{6.6}$$

where $\mathbf{F}_n$ is the coefficient of the n^{th} degree component of $\mathbf{F}$.

6.3 Combinatorial Results

The two-component Stern-Volmer model shows that we can separate the concentration quenching effect on the PL quenching from the electron transfer (ET) effect because of the additive nature of the two quenching processes in Equation 6.7 (as derived in Appendix A):

$$\frac{[F]_T}{[F]} = K_{S1}[Q_1] + K_{S2}[Q_2] + 1 \tag{6.7}$$

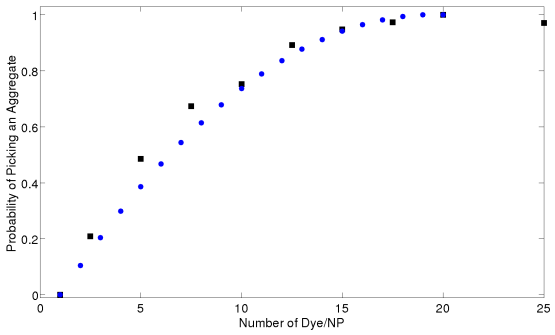

Figure 6.1: Combinatorial analysis of the probability of picking an aggregated dye at varying numbers of dye molecules on a grid of 20 open spaces, plotted alongside the experimental data of photoluminescence quenching.

We arbitrarily assign the first component to be the electron transfer process, thus the Stern-Volmer constant K_{S1} should be related to the binding constant:

$$K_{S1} \propto K_b \tag{6.8}$$

where K_b can be taken from the Langmuir Isotherm experiment. The value for K that has been derived from this data is 3.5×10^4. The second component is the aggregation-induced energy-loss quenching, which is likely some internal conversion pathway that non-radiatively depopulates the excited states of the dye molecules. This energy transfer quenching process can occur if an excited-state dye molecule is within a certain distance of a set of aggregated dyes. This process has been proposed before and, in the case of **1-CO$_2$H** on nc-CdS, should be energetically downhill.[138,195] The ability for excited-state dyes to transfer energy to aggregates depends on the presence of the aggregates, therefore the K_{S2} term should have a contribution that is based on the probability of formation of aggregates.

We have previously obtained a function that allows us to determine the probability of encountering aggregates on a 4x5 grid that approximates the experimental surface of the CdS nanoparticles which possess 20 binding sites. Fig. 6.1 shows this function plotted alongside experimental data showing fluorescence intensity data plotted in Stern-Volmer fashion at various ratios of dye:CdS nanoparticle.

Figure 6.1 shows that there is a close correlation between the model described above

and the experimental data plotted along with it. It should be noted that the experimental data has been scaled and subtracted (as described in Section 5.2.3) to offer a relevant comparison with the model. The fact that the model is consistent with the experimental data gives support to the idea that the crystallographic surfaces of the nc-CdS can be approximated as planar.

6.4 Conclusion

In light of the close match between the experimental data and the theoretical function we believe that the combinatorial analysis adequately describes the surface of the nanoparticle as the dye molecules begin to saturate the surface. We propose that the form of the K_{S2} term should contain this information:

$$K_{S2} \propto \mathbf{P}_n \tag{6.9}$$

so that we can combine the two Stern-Volmer constants to yield Eq. 6.10.

$$\frac{[F]_T}{[F]} = cK_b[Q_1] + d\mathbf{P}_n[Q_2] + 1 \tag{6.10}$$

The inclusion of the probability function $\mathbf{P}_n$ allows for an accurate description of both processes into the two-component Stern-Volmer model.

Chapter 7

Conclusion

In this thesis it has been shown that several dye molecules participate in concentration quenching (CQ) mechanisms on various nanoparticle surfaces. The data obtained from studies of **1-CO_2H** adsorbed onto the surfaces of cadmium sulfide nanoparticles show that the concentration quenching pathway is dependent upon a surface-templated aggregation event that can be detected by a combination of simple ^{1}H-NMR spectroscopy and UV-Vis spectroscopy. These spectroscopic techniques revealed a propensity for **1-CO_2H** to aggregate on the surface of cadmium sulfide nanoparticles in a $\pi - \pi$ stacking configuration. It is thought that perturbation of the electronic structures of **1-CO_2H** molecules in these aggregates facilitates the CQ pathway. Attempts to discover the structure of the aggregates with NMR or Raman techniques were unsuccessful and were not described in this thesis, however it is noted that these techniques should be well suited for this purpose.

Study of the structure of the aggregates composed of **1-CO_2H** molecules was carried out computationally on featureless nanospheres using molecular dynamics with explicit OPLS 3-site CH_2Cl_2 solvent included and at a temperature of 298 K. These analyses provided three important pieces of information. First, the aggregates were confirmed to form computationally, giving credibility to the computational methodology used. Second, these aggregates appear to form and behave similarly across a range of nanospheres used as models for the nanoparticles described above. Lastly, comparison of the energy of ensembles with varying coverages of **1-CO_2H** enabled a measurement of the bulkiness of **1-CO_2H** and this measurement shows that **1-CO_2H** molecules likely do not

saturate the surface of the cadmium sulfide nanoparticle. It is believed that this type of computational analysis will prove useful for researchers who wish to develop new dyes that can effectively block electrolyte species from the surface of a nanoparticle, or who wish to create a dye that will pack efficiently on a surface.

Further experimental research also showed that CQ pathways were active in similar studies using other dye molecules with CdS and ZnO nanoparticle surfaces. Taken along with the conclusions drawn from the system comprised of **1-CO_2H** and nanocrystalline CdS, studies of BODIPY adsorbed to cadmium sulfide elucidate important details of the surface structure of the oleate-capped CdS nanoparticles to which they were adsorbed. Specifically, it seems that the BODIPY molecule packs much more sparsely on the nanocrystalline CdS surface than does **1-CO_2H** and this may reveal details about the facets to which they are adsorbed. More interestingly, however, is the data obtained from the studies of RuDEA on the surface of hexylamine-capped ZnO nanoparticles (nc-ZnO). If this data is confirmed, the previously-accepted theories requiring red-shift-inducing aggregates to be present for CQ to exist will need to be re-examined.

The final point to be made here relates to the incomplete saturation of the cadmium sulfide nanocrystalline system by a variety of ligands. As mentioned above, the computations suggest that the dye molecules are able to pack much more densely onto a featureless sphere than they are onto the nanocrystalline CdS surfaces. It appears that this occurs in other types of nanoparticles as well, but the case is strongest with nanocrystalline CdS. It appears that the available binding sites for molecules containing carboxylic acid groups are found on nearly-flat crystallographic faces that are good templates for dye aggregation.

References

[1] Nathan S. Lewis, George Crabtree, Arthur J. Nozik, Michael R. Wasielewski, Paul Alivisatos, Harriet Kung, Jeffrey Tsao, Elaine Chandler, Wladek Walukiewicz, Mark Spitler, Randy Ellingson, Ralph Overend, Jeffrey Mazer, Mary Gress, James Horwitz, Christie Ashton, Brian Herndon, Leslie Shapard, and Renee M. Nault. Basic Resarch Needs For Solar Energy Utilization. Technical report, Office of Science, US Department of Energy, April 2005.

[2] NREL: National Center for Photovoltaics. NREL: National Center for Photovoltaics Home Page. http://www.nrel.gov/ncpv/, Accessed June 13 2013.

[3] Thomas Surek. Crystal growth and materials research in photovoltaics: progress and challenges. *Journal of Crystal Growth*, 275:292–304, 2005.

[4] William Shockley and Hans J. Queisser. Detailed Balance Limit of Efficiency of p-n Junction solar cells. *Journal of Applied Physics*, 32:510–519, 1961.

[5] Martin A. Green. Crystalline and thin-film silicon solar cells: state of the art and future potential. *Solar Energy*, 74:181–192, 2003.

[6] David Cahen, Gary Hodes, Michael Grätzel, Jean Francois Guillemoles, and Ilan Riess. Nature of Photovoltaic Action in Dye-Sensitized Solar Cells. *Journal of Physical Chemistry, B*, 104:2053–2059, 2000.

[7] Thomas E. Mallouk. Bettering Nature's Solar Cells. *Nature*, 353:698–699, 1991.

[8] Brian O'Regan and Michael Grätzel. A Low-Cost, High-Efficiency Solar Cell Based on Dye-Sensitized Colloidal TiO_2 Films. *Nature*, 353:737–740, 1991.

[9] Brian A. Gregg, Francois Pichot, Suzanne Ferrere, and Clark L. Fields. Interfacial Recombination Processes in Dye-Sensitized Solar Cells and Methods To Passivate the Interfaces. *Journal of Physical Chemistry, B*, 105:1422–1429, 2001.

[10] D. Mao, M. A. Ibrahim, and A. J. Frank. A Plasticized Polymer-Electrolyte-Based Photoelectrochemical Solar Cell. *Journal of the Electrochemical Society*, 145(1):121–124, 1998.

[11] Shigeki Hattori, Yuji Wada, Shozo Yanagida, and Shunichi Fukuzumi. Blue Copper Model Complexes with Distorted Tetragonal Geometry Acting as Effective Electron-Transfer Mediators in Dye-Sensitized Solar Cells. *Journal of the American Chemical Society*, 127:9648–9654, 2005.

[12] G. Schlichthorl, S. Y. Huang, J. Sprague, and A. J. Frank. Band Edge Movement and Recombination Kinetics in Dye-Sensitized Nanocrystalline TiO_2 Solar Cells: A Study by Intensity Modulated Photovoltage Spectroscopy. *Journal of Physical Chemistry B*, 101:8141–8155, 1997.

[13] S. Y. Huang, G. Schlichthorl, A. J. Nozik, M. Grätzel, and A. J. Frank. Charge Recombination in Dye-Sensitized Nanocrystalline TiO_2 Solar Cells. *Journal of Physical Chemistry*, 101:2576–2582, 1997.

[14] Wataru Kubo, Shingo Kambe, Shogo Nakade, Takayuki Kitamura, Kenji Hanabusa, Yuji Wada, and Shozo Yanagida. Photocurrent-Determining Processes in Quasi-Solid-State Dye-Sensitized Solar Cells Using Ionic Gel Electrolytes. *Journal of Physical Chemical, B*, 107:4374–4381, 2003.

[15] Yu Bai, Yiming Cao, Jing Zhang, Mingkui Wang, Renzhi Li, Peng Wang, Shaik M Zakeeruddin, and Michael Grätzel. High-performance dye-sensitized solar cells based on solvent-free electrolytes produced from eutectic melts. *Nature materials*, 7(8):626–630, 2008.

[16] Peng Wang, Shaik M. Zakeeruddin, and Michael Grätzel. Solidifying liquid electrolytes with fluorine polymer and silica nanoparticles for quasi-solid dye-sensitized solar cells. *Journal of Fluorine Chemistry*, 125:1241–1245, 2004.

[17] Ryuji Kawano and Masayoshi Watanabe. Equilibrium potentials and charge transport of an I_2/I_3^- redox couple in an ionic liquid. *Chemical Communications*, pages 330–331, 2003.

[18] Timothy P. Lodge. A Unique Platform for Materials Design. *Science*, 321:50–51, 2008.

[19] Thomas W. Hamann, Rebecca A. Jensen, Alex B. F. Martinson, Hal Van Ryswykac, and Joseph T. Hupp. Advancing beyond current generation dye-sensitized solar cells. *Energy & Environmental Science*, 1:66–78, 2008.

[20] Shahzada Ahmad, Takeru Bessho, Florian Kessler, Etienne Baranoff, Julien Frey, Chenyi Yi, Michael Grätzel, and Mohammad K. Nazeeruddin. A new generation of platinum and iodine free efficient dye-sensitized solar cells. *Phys. Chem. Chem. Phys.*, 14:10631–10639, 2012.

[21] Miguel Garcia-Iglesias, Laia Pelleja, Jun-Ho Yum, David Gonzalez-Rodriguez, Mohammad K. Nazeeruddin, Michael Grätzel, John N. Clifford, Emilio Palomares, Purificacion Vazquez, and Tomas Torres. Effect of bulky groups in ruthenium heteroleptic sensitizers on dye sensitized solar cell performance. *Chemical Science*, 3:1177–1184, 2012.

[22] Jun-Ho Yum, Etienne Baranoff, Florian Kessler, Thomas Moehl, Shahzada Ahmad, Takeru Bessho, Arianna Marchioro, Elham Ghadiri, Jacques-E. Moser, Chenyi Yi, Md. K. Nazeeruddin, and Michael Grätzel. A cobalt complex redox shuttle for dye-sensitized solar cells with high open-circuit potentials. *Nature Communications*, 3:631, 2012.

[23] Miquel Planells, Amparo Forneli, Eugenia Martinez-Ferrero, Antonio Sanchez-Diaz, Maria Angeles Sarmentero, Pablo Ballester, Emilio Palomares, and Brian C. O'Regan. The effect of molecular aggregates over the interfacial charge transfer processes on dye sensitized solar cells. *Appl. Phys. Lett.*, 92:153506, 2008.

[24] Peng Wang, Shaik M. Zakeeruddin, Pascal Comte, Raphael Charvet, Robin Humphry-Baker, and Michael Grätzel. Enhance the performance of dye-sensitized

solar cells by co-grafting amphiphilic sensitizer and hexadecylmalonic acid on tio2 nanocrystals. *J. Phys. Chem. B*, 107:14336–14341, 2003.

[25] Nagatoshi Koumura, Zhong-Sheng Wang, Shogo Mori, Masanori Miyashita, Eiji Suzuki, and Kohjiro Hara. Alkyl-functionalized organic dyes for efficient molecular photovoltaics. *J. Am. Chem. Soc.*, 128:14256–14257, 2006.

[26] Jessica E. Kroeze, Narukuni Hirata, Sara Koops, Md. K. Nazeeruddin, Lukas Schmidt-Mende, Michael Grätzel, and James R. Durrant. Alkyl chain barriers for kinetic optimization in dye-sensitized solar cells. *J. Am. Chem. Soc.*, 128:16376–16383, 2006.

[27] Aswani Yella, Hsuan-Wei Lee, Hoi Nok Tsao, Chenyi Yi, Aravind Kumar Chandiran, Md. Khaja Nazeeruddin, Eric Wei-Guang Diau, Chen-Yu Yeh, Shaik M Zakeeruddin, and Michael Grtzel. Porphyrin-Sensitized Solar Cells with Cobalt (II/III)Based Redox Electrolyte Exceed 12 Percent Efficiency. *Science*, 334:629–634, 2011.

[28] H. Gerischer. Electrochemical techniques for the study of photosensitization. *Photochemistry and Photobiology*, 16:243–260, 1972.

[29] M. K. Nazeeruddin, A. Kay, I. Rodicio, R. Humphry-Baker, E. Mueller, P. Liska, N. Vlachopoulos, and M. Grätzel. Conversion of light to electricity by cis-X2bis(2,2'-bipyridyl-4,4'-dicarboxylate)ruthenium(II) charge-transfer sensitizers (X = Cl-, Br-, I-, CN-, and SCN-) on nanocrystalline titanium dioxide electrodes. *Journal of the American Chemical Society*, 115:6382–6390, 1993.

[30] Neil Robertson. Optimizing Dyes for Dye-Sensitized Solar Cells. *Angewandte Chemie, International Edition*, 45:2338–2345, 2006.

[31] Seigo Ito, Paul Liska, Pascal Comte, Raphael Charvet, Peter Pechy, Udo Bach, Lukas Schmidt-Mende, Shaik Mohammed Zakeeruddin, Andreas Kay, Mohammad K. Nazeeruddin, and Michael Grätzel. Control of dark current in photoelectrochemical (TiO_2/I_2I_3) and dye-sensitized solar cells. *Chemical Communications*, pages 4351–4353, 2005.

[32] Elaine A. M. Geary, Lesley J. Yellowlees, Lorna A. Jack, Iain D. H. Oswald, Simon Parsons, Narukuni Hirata, James R. Durrant, and Neil Robertson. Synthesis, Structure, and Properties of [Pt(II)(diimine)(dithiolate)] Dyes with 3,3'-, 4,4'-, and 5,5'-Disubstituted Bipyridyl: Applications in Dye-Sensitized Solar Cells. *Inorganic Chemistry*, 44:242–250, 2005.

[33] J. M. Kroon, N. J. Bakker, H. J. P. Smit, P. Liska, K. R. Thampi, P. Wang, S. M. Zakeeruddin, M. Grätzel, A. Hinsch, S. Hore, U. Wurfel, R. Sastrawan, J. R. Durrant, E. Palomares, H. Pettersson, T. Gruszecki, J. Walter, K. Skupien, and G. E. Tulloch. Nanocrystalline Dye-sensitized Cells Having Maximum Performance. *Progress in Photovoltaics: Research and Applications*, 15:1–18, 2007.

[34] Mohammad K. Nazeeruddin, Filippo De Angelis, Simona Fantacci, Annabella Selloni, Guido Viscardi, Paul Liska, Seigo Ito, Bessho Takeru, and Michael Grätzel. Combined Experimental and DFT-TDDFT Computational Study of Photoelectrochemical Cell Ruthenium Sensitizers. *Journal of the American Chemical Society*, 127:16835–16847, 2005.

[35] Mohammad K. Nazeeruddin, Peter Pechy, Thierry Renouard, Shaik M. Zakeeruddin, Robin Humphry-Baker, Pascal Comte, Paul Liska, Le Cevey, Emiliana Costa, Valery Shklover, Leone Spiccia, Glen B. Deacon, Carlo A. Bignozzi, and Michael Grätzel. Engineering of Efficient Panchromatic Sensitizers for Nanocrystalline TiO_2-Based Solar Cells. *Journal of the American Chemical Society*, 123:1613–1624, 2001.

[36] Yasuo Chiba, Ashraful Islam, Yuki W Atanabe, Ryoichi K Omiya, Naoki K Oide, and Liyuan Han. Dye-Sensitized Solar Cells with Conversion Efficiency of 11.1 *Japanese Journal of Applied Physics*, 45(25):L638–L640, 2006.

[37] Michael Grätzel. Dye-Sensitized Solid State Heterojunction Solar Cells. *MRS Bulletin*, 30:23–27, 2005.

[38] T. Stergiopoulos, S. Karakostas, and P. Falaras. Comparative studies of substituted ruthenium(II)pyrazoylpyridine complexes with classical N3 photosensitizer:

the influence of NCS dye ligands on the efficiency of solid-state nanocrystalline solar cells. *Journal of Photochemistry and Photobiology A: Chemistry*, 163:331–340, 2004.

[39] P.R. Somani, C. Dionigi, M. Murgia, D. Palles, P. Nozar, and G. Ruani. Solid-state dye PV cells using inverse opal TiO2 films. *Solar Energy Materials & Solar Cells*, 87:513–519, 2005.

[40] Kei Murakoshi, Ryuichiro Kogure, Yuji Wada, and Shozo Yanagida. Fabrication of solid-state dye-sensitized TiO_2 solar cells combined with polypyrrole. *Solar Energy Materials and Solar Cells*, 55:113–125, 1998.

[41] K. Tennakone, G.R.R.A. Kumara, K.G.U. Wijayantha, I.R.M. Kottegoda, V.P.S. Perera, and G.M.L.P. Aponsu. A nanoporous solid-state photovoltaic cell sensitized with copper chlorophyllin. *Journal of Photochemistry and Photobiology A: Chemistry*, 108:175–177, 1997.

[42] David D Graf, John Campbell, Larry Miller, and Kent Mann. Single-Crystal X-ray Structure of the Cation Radical of 3',4'-Dibutyl-2,5"-diphenyl-2,2':5',2"-terthiophene: Definitive Evidence for π-Stacked Oxidized Oligothiophene. *Journal of the American Chemical Society*, 118:5480–5481, 1996.

[43] Ted M. Pappenfus, Jonathan D. Raff, Eric J. Hukkanen, Jason R. Burney, Juan Casado, Steven M. Drew, Larry L. Miller, and Kent R. Mann. Dinitro and Quinodimethane Derivatives of Terthiophene That Can Be Both Oxidized and Reduced. Crystal Structures, Spectra, and a Method for Analyzing Quinoid Contributions to Structure. *Journal of Organic Chemistry*, 67:6015–6024, 2002.

[44] G.A. Reynolds and K.H. Drexhage. New Coumarin Dyes with Rigidized Structure for Flashlamp-Pumped Dye Lasers. *Optics Communications*, 13(3):222–225, 1975.

[45] Sule Erten-Ela, M. Deniz Yilmaz, Burcak Icli, Yavuz Dede, Siddik Icli, and Engin U. Akkaya. A Panchromatic Boradiazaindacene (BODIPY) Sensitizer for Dye-Sensitized Solar Cells. *Organic Letters*, 10(15):3299–3302, 2008.

[46] Neil Robertson. Catching the Rainbow: Light Harvesting in Dye-Sensitized Solar Cells. *Angewandte Chemie, International Edition*, 47:1012–1014, 2008.

[47] Aidan G. Young, Najeh Al-Salim, David P. Green, and A. James McQuillan. Attenuated Total Reflection Infrared Studies of Oleate and Trioctylphosphine Oxide Ligand Adsorption and Exchange Reactions on CdS Quantum Dot Films. *Langmuir*, 24:3841–3849, 2008.

[48] Yu-Xiang Weng, Long Li, Yin Liu, Li Wang, and Guo-Zhen Yang. Surface-Binding Forms of Carboxylic Groups on Nanoparticulate TiO_2 Surface Studied by the Interface-Sensitive Transient Triplet-State Molcular Probe. *Journal of Physical Chemistry, B*, 107:4356–4363, 2003.

[49] Shane Ardo and Gerald J. Meyer. Photodriven heterogeneous charge transfer with transition-metal compounds anchored to TiO_2 semiconductor surfaces. *Chemical Society Reviews*, 38:115–164, 2009.

[50] HyoJoong Lee, Henry C. Leventis, Soo-Jin Moon, Peter Chen, Seigo Ito, Saif A. Haque, Tomas Torres, Frank Nuesch, Thomas Geiger, Shaik M. Zakeeruddin, Michael Grätzel, and Md. Khaja Nazeeruddin. PbS and CdS Quantum Dot-Sensitized Solid-State Solar Cells: "Old Concepts, New Results". *Advanced Functional Materials*, 19:2735–2742, 2009.

[51] Kurtis S. Leschkies, Ramachandran Divakar, Joysurya Basu, Emil Enache-Pommer, Janice E. Boercker, C. Barry Carter, Uwe R. Kortshagen, David J. Norris, and Eray S. Aydil. Photosensitization of ZnO Nanowires with CdSe Quantum Dots forPhotovoltaic Devices. *Nano Letters*, 7(6):1793–1798, 2007.

[52] Jin Ho Bang and Prashant Kamat. Quantum Dot Sensitized Solar Cells. A Tale of Two Semiconductor Nanocrystals: CdSe and CdTe. *ACS Nano*, 3(6):1467–1476, 2009.

[53] Jing Chen, J. L. Song, X. W. Sun, W. Q. Deng, C. Y. Jiang, W. Lei, J. H. Huang, and R. S. Li. An oleic acid-capped CdSe quantum-dot sensitized solar cell. *Applied Physics Letters*, 94:153115, 2009.

[54] Blake Farrow and Prashant V. Kamat. CdSe Quantum Dot Sensitized Solar Cells. Shuttling Electrons Through Stacked Carbon Nanocups. *Journal of the American Chemical Society*, 131:11124–11131, 2009.

[55] Wonjoo Lee, Soon Hyung Kang, Jae-Yup Kim, Govind B Kolekar, Yung-Eun Sung, and Sung-Hwan Han. TiO_2 nanotubes with a ZnO thin energy barrier for improved current efficiency of CdSe quantum-dot-sensitized solar cells. *Nanotechnology*, 20:1–7, 2009.

[56] I. Mora-Sero, J. Bisquert, Th. Dittrich, A. Belaidi, A. S. Susha, and A. L. Rogach. Photosensitization of TiO_2 Layers with CdSe Quantum Dots: Correlation between Light Absorption and Photoinjection. *Journal of Physical Chemistry, C*, 111:14889–14892, 2007.

[57] G. D. Sharma, D. C. Dube, and S. C. Mathur. CdS and AgBr Sensitized Eriochrome Black T (EBT) Dye solar cells. *Solar Cells*, 15:189–197, 1985.

[58] Yu-Jen Shen and Yuh-Lang Lee. Assembly of CdS quantum dots onto mesoscopic TiO_2 films for quantum dot-sensitized solar cell applications. *Nanotechnology*, 19:045602, 2008.

[59] Wen-Tao Sun, Hua-Yong Pan Yuan Yu, Xian-Feng Gao, Qing Chen, and Lian-Mao Peng. CdS Quantum Dots Sensitized TiO2 Nanotube-Array Photoelectrodes. *Journal of the American Chemical Society*, 130:1124–1125, 2008.

[60] L. E. Brus. Electron-eletron and electron-hole interactions in small semiconductor crystallites: The size dependence of the lowest excited electronic state. *Journal of Chemical Physics*, 80(9):4403–4409, 1984.

[61] L. E. Brus. A Simple Model for the ionization potential, electron affinity, and aqueous redox potentials of small semiconductor crystallites. *Journal of Chemical Physics*, 79(11):5565–5571, 1983.

[62] Louis Brus. Electronic Wave Functions in Semiconductor Clusters: Experiment and Theory. *Journal of Physical Chemistry*, 90:2555–2560, 1986.

[63] Hyo Joong Lee, Jun-Ho Yum, Henry C. Leventis, Shaik M. Zakeeruddin, Saif A. Haque, Peter Chen, Sang Il Seok, Michael Grätzel, and Md. K. Nazeeruddin. CdSe Quantum Dot-Sensitized Solar Cells Exceeding Efficiency 1Full-Sun Intensity. *Journal of Physical Chemistry, C*, 112:11600–11608, 2008.

[64] Darren Lawless, Sudhir Kapoor, and Dan Meisel. Bifunctional Capping of CdS Nanoparticles and Bridging to Ti02. *Journal of Physical Chemistry*, 99:10329–10335, 1995.

[65] Brooke Carlson, Kurtis Leschkies, Eray S. Aydil, and X.-Y. Zhu. Valence Band Alignment at Cadmium Selenide Quantum Dot and Zinc Oxide (1010) Interfaces. *Journal of Physical Chemistry, C*, 112:8419–8423, 2008.

[66] Ivan Mora-Sero, Sixto Giminez, Thomas Moehl, Francisco Fabregat-Santiago, Teresa Lana-Villareal, Roberto Gomez, and Juan Bisquert. Factors determining the photovoltaic performance of a CdSe quantum dot sensitized solar cell: the role of the linker molecule and of the counter electrode. *Nanotechnology*, 19:424007, 2008.

[67] Youngjo Tak, Suk Joon Hong, Jae Sung Leeb, and Kijung Yong. Fabrication of ZnO/CdS core/shell nanowire arrays for efficient solar energy conversion. *Journal of Materials Chemistry*, 19:5945–5951, 2009.

[68] Hui Zhang, Xie Quan, Shuo Chen, Hongtao Yu, and Ning Ma. "Mulberry-like" CdSe Nanoclusters Anchored on TiO2 Nanotube Arrays: A Novel Architecture with Remarkable Photoelectrochemical Performance. *Chemistry of Materials*, 21:3090–3095, 2009.

[69] Menny Shalom, Sven Ruhle, Idan Hod, Shay Yahav, and Arie Zaban. Energy Level Alignment in CdS Quantum Dot Sensitized Solar Cells Using Molecular Dipoles. *Journal of the American Chemical Society*, 131:9876–9877, 2009.

[70] Kajari Das and S. K. De. Optical Properties of the Type-II Core#Shell TiOCdS Nanorods for Photovoltaic Applications. *Journal of Physical Chemistry, C*, 113(9):3494–3501, 2009.

[71] Alex B. F. Martinson, Thomas W. Hamann, Michael J. Pellin, and Joseph T. Hupp. New Architectures for Dye-Sensitized Solar Cells. *Chem. Eur. J.*, 14:4458–4467, 2008.

[72] A. Zaban, O. I. Micic, B. A. Gregg, and A. J. Nozik. Photosensitization of Nanoporous TiO2 Electrodes with InP Quantum Dots. *Langmuir*, 14:3153–3156, 1998.

[73] J. L. Blackburn, D. C. Selmarten, R. J. Ellingson, M. Jones, O. Micic, and A. J. Nozik. Electron and Hole Transfer from Indium Phosphide Quantum Dots. *Journal of Physical Chemistry, B*, 109:2625–2631, 2005.

[74] Pingrong Yu, Kai Zhu, Andrew G. Norman, Suzanne Ferrere, Arthur J. Frank, and Arthur J. Nozik. Nanocrystalline TiO_2 Solar Cells Sensitized with InAs Quantum Dots. *Journal of Physical Chemistry, B*, 110:25451–25454, 2006.

[75] Rachel S. Dibbell and David F. Watson. Distance-Dependent Electron Transfer in Tethered Assemblies of CdS Quantum Dots and TiO_2 Nanoparticles. *Journal of Physical Chemistry, C*, 113(8):3139–3149, 2009.

[76] Anders Hagfeldt and Michael Grätzel. Molecular Photonics. *Accounts of Chemical Research*, 33:269–277, 2000.

[77] Greg Smestad and Michael Grätzel. Demonstrating Electron Transfer and Nanotechnology: A Natural Dye-Sensitized Nanocrystalline Energy Converter. *Journal of Chemical Education*, 75(6):752–756, 1998.

[78] B. I. Lemon, L. A. Lyon, and J.T. Hupp. *Nanoparticles and Nanostructured Films*, chapter 14 - Charge Transfer at Nanocrystalline Metal Oxide Semiconductor-Solution Interfaces: Mechanistic and Energetic Links between Electrochromic-Battery Interfaces and Photovoltaic-Photocatalytic Interfaces. Wiley-VCH, 1998.

[79] K. Kalyanasundaram and M. Grätzel. Applications of functionalized transition metal complexes in photonic and optoelectronic devices. *Coordination Chemistry Reviews*, 77:347–414, 1998.

[80] Allen J. Bard. Design of Semiconductor Photoelectrochemical Systems for Solar Energy Conversion. *Journal of Physical Chemistry*, 86:172–177, 1982.

[81] L. Kronik, N. Ashkenasy, M. Leibovitch, E. Fefer, S. Gorer Yoram Shapira, and G. Hodes. Surface States and Photovoltaic Effects in CdSe quantum dot films. *Journal of the Electrochemical Society*, 145(5):1748–1756, 1998.

[82] Michael Grätzel. Solar Energy Conversion by Dye-Sensitized Photovoltaic Cells. *Inorganic Chemistry*, 44:6841–6851, 2005.

[83] Arie Zaban, Andreas Meier, and Brian A. Gregg. Electric Potential Distribution and Short-Range Screening in Nanoporous TiO_2 Electrodes. *Journal of Physical Chemistry, B*, 101:7985–7990, 1997.

[84] Suzanne Ferrere and Brian A. Gregg. Large Increases in Photocurrents and Solar Conversion Efficiencies by UV Illumination of Dye Sensitized Solar Cells. *Journal of Physical Chemistry, B*, 105:7602–7605, 2001.

[85] Craig Kelly, Fereshteh Farzad, David Thompson, Jeremy Stipkala, and Gerald Meyer. Cation-Controlled Interfacial Charge Injection in Sensitized Nanocrystalline TiO_2. *Langmuir*, 15:7047–7054, 1999.

[86] Andreas Kay and Michael Grätzel. Artificial Photosynthesis. 1. Photosensitization of $Ti0_2$ Solar Cells with Chlorophyll Derivatives and Related Natural Porphyrins. *Journal of Physical Chemistry*, 97:6272–6277, 1993.

[87] Nathan R. Neale, Nikos Kopidakis, Jao van de Lagemaat, Michael Grätzel, and Arthur J. Frank. Effect of a Coadsorbent on the Performance of Dye-Sensitized TiO2 Solar Cells: Shielding versus Band-Edge Movement. *Journal of Physical Chemistry, B*, 109:23183–23189, 2005.

[88] Louis Brus. Model for carrier dynamics and photoluminescence quenching in wet and dry porous silicon thin films. *Physical Review B*, 53(8):4649–4657, 1996.

[89] P. E. de Jongh and D. Vanmaekelbergh. Trap-Limited Electronic Transport in Assemblies of Nanometer-Size TiO_2 Particles. *Physical Review Letters*, 77(16):3427–3430, 1996.

[90] K. Schwarzburg and F. Willig. lnfluence of trap filling on photocurrent transients in polycrystalline TiO_2. *Applied Physics Letters*, 58(22):2520–2523, 1991.

[91] G.K. Boschloo, A. Goossens, and J. Schoonman. Investigation of the potential distribution in porous nanocrystalline TiO_2 electrodes by electrolyte electroreflection. *Journal of Electroanalytical Chemistry*, 428:25–32, 1997.

[92] Albert Goossens, Barbara van der Zanden, and Joop Schoonman. Single-electron migration in nanostructured TiO_2. *Chemical Physics Letters*, 331:1–6, 2000.

[93] Janne Halme. Dye-sensitized nanostructured and organic photovoltaic cells: technical review and preliminary tests. Master's thesis, Helsinke University of Technology, Department of Engineering Physics and Mathematics, 2002.

[94] Wayne Gladfelter, Kent Mann, and David Blank. Monodispersed Zinc Oxide Nanoparticle-Dye Dyads and Triads: Characterization of the Early Events in Dye-Sensitized Solar Cells. *DOE Proposal, Basic Research for Solar Energy Utilization*, pages 1–17, 2006.

[95] W. William Yu and Xiaogang Peng. Formation of High-Quality CdS and Other II-VI Semiconductor Nanocrystals in Noncoordinating Solvents: Tunable Reactivity of Monomers. *Angewandte Chemie, International Edition*, 41(13):2368–2371, 2002.

[96] C. B. Murray, D. J. Norris, and M. G. Bawendi. Synthesis and characterization of nearly monodisperse CdE (E = sulfur, selenium, tellurium) semiconductor nanocrystallites. *Journal of the American Chemical Society*, 115:8706–8715, 1993.

[97] Z. Adam Peng and Xiaogang Peng. Formation of High-Quality CdTe, CdSe, and CdS Nanocrystals Using CdO as Precursor. *Journal of the American Chemical Society*, 123:183–184, 2001.

[98] Xiaogang Peng, J. Wickham, and A. P. Alivisatos. Kinetics of II-VI and III-V Colloidal Semiconductor Nanocrystal Growth: "Focusing" of Size Distributions. *Journal of the American Chemical Society*, 120(21):5343–5344, 1998.

[99] A. P. Alivisatos. Perspectives on the Physical Chemistry of Semiconductor Nanocrystals. *Journal of Physical Chemistry*, 100:13226–13239, 1996.

[100] Mathias Brust, Merryl Walker, Donald Bethell, David J. Schiffrin, and Robin Whyman. Synthesis of Thiol-derivatised Gold Nanoparticles in a Two-phase Liquid-Liquid System. *Journal of the Chemical Society, Chemical Communications*, pages 801–802, 1994.

[101] P. Davide Cozzoli, Andreas Kornowski, and Horst Weller. Low-Temperature Synthesis of Soluble and Processable Organic-Capped Anatase TiO_2 Nanorods. *Journal of the American Chemical Society*, 125:14539–14548, 2003.

[102] Mia G. Berrettini, Gary Braun, Jerry G. Hu, and Geoffrey F. Strouse. NMR Analysis of Surfaces and Interfaces in 2-nm CdSe. *Journal of the American Chemical Society*, 126:7063–7070, 2004.

[103] J. A. Mielczarski, J. M. Cases, E. Bouquet, 0. Barres, and J. F. Delon. Nature and Structure of Adsorption Layer on Apatite Contacted with Oleate Solution. 1. Adsorption and Fourier Transform Infrared Reflection Studies. *Langmuir*, 9:2370–2382, 1993.

[104] W. William Yu, Lianhua Qu, Wenzhuo Guo, and Xiaogang Peng. Experimental Determination of the Extinction Coefficient of CdTe, CdSe, and CdS Nanocrystals. *Chemistry of Materials*, 15(14):2854–2860, 2003.

[105] Chunlei Wang, Hao Zhang, Junhu Zhang, Minjie Li, Kun Han, and Bai Yang. The influence of oxygen on the fluorescence enhancement of fatty-acid-capped CdS nanocrystals. *Journal of Colloid and Interface Science*, 294:104–108, 2006.

[106] Ranjani Viswanatha, Sameer Sapra, B. Satpati, P. V. Satyam, B. N. Devb, and D. D. Sarma. Understanding the quantum size effects in ZnO nanocrystals. *Journal of Materials Chemistry*, 14:661–668, 2004.

[107] Martin A. Green. Third Generation Photovoltaics: Ultra-high Conversion Efficiency at Low Cost. *Progress in Photovoltaics: Research and Applications*, 9:123–135, 2001.

[108] Neil A. Anderson and Tianquan Lian. Ultrafast Electron Transfer at the Molecule-Semiconductor Nanoparticle Interface. *Annu. Rev. Phys. Chem.*, 56:491–519, 2005.

[109] Nathan Lewis and Daniel Nocera. Powering the Planet: Chemical Challenges in Solar Energy Utilization. *Proceedings of the National Academy of Sciences*, 43:15729–15735, 2006.

[110] Jacques Moser and Michael Grätzel. Photosensitized electron injection in colloidal semiconductors. *J. Am. Chem. Soc.*, 106:6557–6564, 1984.

[111] Xiaojun Dang and Joseph T. Hupp. Interfacial Charge-Transfer Pathways: Evidence for Marcus-Type Inverted Electron Transfer in Metal Oxide Semiconductor/Inorganic Dye Systems. *J. Am. Chem. Soc.*, 121:8399–8400, 1999.

[112] Dennis A. Gaal and Joseph T. Hupp. Thermally Activated, Inverted Interfacial Electron Transfer Kinetics: High Driving Force Reactions between Tin Oxide Nanoparticles and Electrostatically-Bound Molecular Reactants. *J. Am. Chem. Soc.*, 122:10956–10963, 2000.

[113] Waldo J. E. Beek and René A. J. Janssen. Photoinduced Electron Transfer in Heterosupramolecular Assemblies of TiO_2 Nanoparticles and Terthiophene Carboxylic Acid in Apolar Solvents. *Adv. Funct. Mater.*, 12:519–525, 2002.

[114] Tao Huang and Royce W. Murray. Quenching of $[Ru(bpy)_3]^{2+}$ Fluorescence by Binding to Au Nanoparticles. *Langmuir*, 18:7077–7081, 2002.

[115] Waldo J. E. Beek and René A. J. Janssen. Spacer Length Dependence of Photoinduced Electron Transfer in Heterosupramolecular Assemblies of TiO_2 Nanoparticles and Terthiophene. *J. Mater. Chem.*, 14:2795–2800, 2004.

[116] Tarek Antoun, Roberta Brayner, Seham Al terary, Fernand Fievet, Mohamed Chehimi, and Abderrahim Yassar. Facile Synthesis of Oligothiophene-Capped CdS Nanoparticles. *European Journal of Inorganic Chemistry*, pages 1275–1284, 2007.

[117] William R. McNamara, Robert C. Snoeberger III, Gonghu Li, James M. Schleicher, Clyde W. Cady, Macarena Poyatos, Charles A. Schmuttenmaer, Robert H. Crabtree, Gary W. Brudvig, and Victor S. Batista. Acetylacetonate Anchors for Robust Functionalization of TiO_2 Nanoparticles with Mn(II)-Terpyridine Complexes. *J. Am. Chem. Soc.*, 130:14329–14338, 2008.

[118] Renata Marczak, Fabian Werner, Jan-Frederik Gnichwitz, Andreas Hirsch, Dirk M. Guldi, and Wolfgang Peukert. Communication via Electron and Energy Transfer between Zinc Oxide Nanoparticles and Organic Adsorbates. *J. Phys. Chem. C*, 113:4669–4678, 2009.

[119] Shankar Varaganti and Guda Ramakrishna. Dynamics of Interfacial Charge Transfer Emission in Small Molecule Sensitized TiO_2 Nanoparticles: Is It Localized or Delocalized? *J. Phys. Chem. C*, 114:13917–13925, 2010.

[120] Adam Huss, Julia Rossini, Darren Ceckanowicz, Jon Bohnsack, Kent Mann, Wayne Gladfelter, and David Blank. Photoinitiated electron transfer dynamics of a terthiophene carboxylate on monodispersed zinc oxide nanocrystals. *J. Phys. Chem. C*, 115:2–10, 2011.

[121] Julia E Rossini, Adam S Huss, Jon Bohnsack, David Blank, Kent Mann, and Wayne Gladfelter. Binding and Static Quenching Behavior of a Terthiophene Carboxylate on Monodispersed Zinc Oxide Nanocrystals. *J. Phys. Chem. C*, 115:11–17, 2011.

[122] Delia J. Milliron, A. Paul Alivisatos, Claire Pitois, Carine Edder, and Jean M. J. Frechet. Electroactive Surfactant Designed to Mediate Electron Transfer Between CdSe Nanocrystals and Organic Semiconductors. *Adv. Mater.*, 15:58–61, 2003.

[123] Chris Van de Walle and J. Neugebauer. Universal Alignment of Hydrogen Levels in Semiconductors, Insulators and Solutions. *Nature*, 423:626–629, 2003.

[124] Joseph R. Sachleben, E. Wrenn Wooten, Lyndon Emsley, Alexander Pines, Vicki Colvin, and A. Paul Alivisatos. NMR Studies of the Surface Structure and Dynamics of Semiconductor Nanocrystals. *Chem. Phys. Lett.*, 198:431–436, 1992.

[125] A. Badia, W. Gao, S. Singh, L. Demers, L. Cuccia, and L. Reven. Structure and Chain Dynamics of Alkanethiol-Capped Gold Colloids. *Langmuir*, 12:1262–1269, 1996.

[126] Olaf Kohlmann, Wayne E. Steinmetz, Xi-An Mao, W. Peter Wuelfing, Allen C. Templeton, Royce W. Murray, and Charles S. Johnson Jr. NMR Diffusion, Relaxation, and Spectroscopic Studies of Water Soluble, Monolayer-Protected Gold Nanoclusters. *Journal of Physical Chemistry, B*, 105:8801–8809, 2001.

[127] Brian S. Zelakiewicz, Angel C. de Dios, and YuYe Tong. ^{13}C NMR Spectroscopy of $^{13}C_1$-Labeled Octanethiol-Protected Au Nanoparticles: Shifts, Relaxations, and Particle-Size Effect. *Journal of the American Chemical Society*, 125:18–19, 2003.

[128] Hongyu Zhou, Fenfang Du, Xi Li, Bin Zhang, Wei Li, and Bing Yan. Characterization of Organic Molecules Attached to Gold Nanoparicle Surface Using High Resolution Magic Angle Spinning ^1H NMR. *Journal of Physical Chemistry, C*, 112:19360–19366, 2008.

[129] D. Fassler, X. Baezold, and D. Baezold. Energy and Electron Transfer Processes of Adsorbed Polymethine Dyes. *J. Mol. Struct.*, 174:383–387, 1988.

[130] Nicholas Turro. *Modern Molecular Photochemistry.* Benjamin/Cummings Publishing Company, 1978.

[131] D. Scott Bohle and Carla J. Spina. Cationic and Anionic Surface Binding Sites on Nanocrystalline Zinc Oxide: Surface Influence on Photoluminescence and Photocatalysis. *J. Am. Chem. Soc.*, 131:4397–4404, 2009.

[132] P.J. Hore. *Nuclear Magnetic Resonance.* Oxford University Press, 1995.

[133] Joseph Lambert, Herbert Shurvell, David Lightner, and R. Graham Cooks. *Organic Structural Spectroscopy.* Prentice Hall, 1998.

[134] P. E. Lippens and M. Lannoo. Calculation of the band gap for small CdS and ZnS crystallites. *Phys. Rev. B*, 39:10935–10942, 1989.

[135] K. Kalyanasundaram, N. Vlachopoulos, V. Krishnan, A. Monnier, and M. Grätzel. Sensitization of TiO_2 in the Visible Light Region Using Zinc Porphyrins. *The Journal of Physical Chemistry*, 91(9):2342–2347, 1987, http://pubs.acs.org/doi/pdf/10.1021/j100293a027.

[136] R. Kietzmann, F. Willig, H. Weller, R. Vogel, D. N. Nath, R. Eichberger, P. Liska, and J. Lehnert. Picosecond Time Resolved Electron Injection from Excited Cresyl Violet Monomers and Cd_3P_2 Quantum Dots into TiO_2. *Mol. Cryst. Liq. Cryst.*, 194:169–180, 1991. Not printed.

[137] Y. Liang, A. M. Ponte Goncalves, and D. K. Negus. Picosecond fluorescence lifetime measurements on dyes adsorbed at semiconductor and insulator surfaces. *The Journal of Physical Chemistry*, 87(1):1–4, 1983, http://pubs.acs.org/doi/pdf/10.1021/j100224a001.

[138] Nobuaki Nakashima, Keitaro Yoshihara, and Frank Willig. Time-Resolved Measurements of Electron and Energy Transfer of Rhodamine B Monolayer on the Surface of Organic Crystals. *J. Chem. Phys.*, 73:3553–3559, 1980.

[139] A. A. Muenter, D. V. Brumbaugh, J. Apolito, L. A. Horn, F. C. Spano, and S. Mukamel. Size Dependence of Excited-State Dynamics for J-Aggregates at AgBr Interfaces. *J. Phys. Chem.*, 96:2783–2790, 1992.

[140] Tadaaki Tani, Takeshi Suzumoto, Klaus Kemnitz, and Keitaro Yoshihara. Picosecond Kinetics of Light-Induced Electron Transfer from J-Aggregated Cyanine Dyes to AgBr Microcrystals: Effect of Aggregate Size. *J. Phys. Chem.*, 96:2778–2783, 1992.

[141] Saji Alex, U. Santhosh, and Suresh Das. Dye sensitization of nanocrystalline TiO_2: enhanced efficiency of unsymmetrical versus symmetrical squaraine dyes. *J. Photochem. Photobio A*, 172:63–71, 2005.

[142] Ali Chami Khazraji, Surat Hotchandani, Suresh Das, and Prashant Kamat. Controlling Dye (Merocyanine-540) Aggregation on Nanostructured TiO_2 Films. An Organized Assembly Approach for Enhancing the Efficiency of Photosensitization. *J. Phys. Chem. B*, 103:4693–4700, 1999.

[143] Kazuhiro Sayamaa, Shingo Tsukagoshib, Tohru Morib, Kohjiro Haraa, Yasuyo Ohgac, Akira Shinpouc, Yoshimoto Abeb, Sadaharu Sugac, and Hironori Arakawa. Efficient sensitization of nanocrystalline TiO_2 films with cyanine and merocyanine organic dyes. *Sol. Energy Mater. Sol. Cells*, 80:47–71, 2003.

[144] Sergio Tatay, Saif A. Haque, Brian O'Regan, James R. Durrant, W. J. H. Verhees, J. M. Kroon, A. Vidal-Ferran, Pablo Gavina, and Emilio Palomares. Kinetic competition in liquid electrolyte and solid-state cyanine dye sensitized solar cells. *J. Mater. Chem.*, 17:3037–3044, 2007.

[145] Kazuhiro Sayama, Kohjiro Hara, Nahoko Mori, Makoto Satsuki, Sadaharu Suga, Shingo Tsukagoshi, Yoshimoto Abe, Hideki Sugiharaa, and Hironori Arakawa. Photosensitization of a porous TiO_2 electrode with merocyanine dyes containing a carboxyl group and a long alkyl chain. *Chem. Commun.*, 0:1173–1174, 2000.

[146] A. Ehret, L. Stuhl, and M. T. Spitler. Spectral Sensitization of TiO_2 Nanocrystalline Electrodes with Aggregated Cyanine Dyes. *J. Phys. Chem. B*, 105:9960–9965, 2001.

[147] Jonathan R. Mann, Michael K. Gannon, Thomas C. Fitzgibbons, Michael R. Detty, and David F. Watson. Optimizing the Photocurrent Efficiency of Dye-Sensitized Solar Cells through the Controlled Aggregation of Chalcogenoxanthylium Dyes on Nanocrystalline Titania Films. *J. Phys. Chem. C*, 112:13057–13061, 2008.

[148] Kacie Mulhern, Michael Detty, and David Watson. Aggregation-Induced Increase of the Quantum Yield of Electron Injection from Chalcogenorhodamine Dyes to TiO_2. *J. Phys. Chem. C*, 115:6010–6018, 2011.

[149] R. Eichberger and F. Willig. Ultrafast electron injection from excited dye molecules into semiconductor electrodes. *Chem. Phys.*, 141:159–173, 1990.

[150] Klaus Kemnitz, Toshiro Murao, Iwao Yamazaki, Nobuaki Nakashima, and Keitaro Yoshihara. Picosecond Fluorescence Measurement of Submono- and Mono-layer of Adsorbed Rhodamine B on a Single Crystal of Naphthalene and on Glass. *Chem. Phys. Lett.*, 101:337–340, 1983.

[151] Joseph R. Lakowicz. *Principles of Fluorescence Spectroscopy*, chapter 8, page 282. Springer Science, third edition, 2006.

[152] E. Rosenthal and K.K.R. Zinn. *Optical Imaging of Cancer: Clinical Applications.* Springer London, Limited, 2009.

[153] Fabio Fernandes, Luis M S Loura, Manuel Prieto, Rob Koehorst, Ruud B Spruijt, and Marcus A Hemminga. Dependence of M13 major coat protein oligomerization and lateral segregation on bilayer composition. *Biophys. J.*, 85:2430–41, 2003.

[154] C.D. Geddes and J.R. Lakowicz. *Reviews in Fluorescence 2005*. Springer, 2007.

[155] Safacan Kolemen, O. Altan Bozdemir, Yusuf Cakmak, Gokhan Barin, Sule Erten-Ela, Magdalena Marszalek, Jun-Ho Yum, Shaik M. Zakeeruddin, Mohammad K. Nazeeruddin, Michael Grätzel, and Engin U. Akkaya. Optimization of distyryl-bodipy chromophores for efficient panchromatic sensitization in dye sensitized solar cells. *Chem. Sci.*, 2:949–954, 2011.

[156] Rajan Vatassery, Jonathan A. Hinke, Antonio Sanchez-Diaz, Ryan Hue, Kent R. Mann, David A. Blank, and Wayne L. Gladfelter. Excited-State Quenching Mechanism of a Terthiophene Acid Dye Bound to Monodisperse CdS Nanocrystals: Electron Transfer versus Concentration Quenching. *J. Phys. Chem. C*, 117:10708–10715, 2013.

[157] Bing Luo, Julia Rossini, and Wayne Gladfelter. Zinc Oxide Nanocrystals Stabilized by Alkylammonium Alkylcarbamates. *Langmuir*, 25(22):13133–13141, 2009.

[158] Torben Daeneke, Tae-Hyuk Kwon, Andrew B. Holmes, Noel W. Duffy, Udo Bach, and Leone Spiccia. High-efficiency dye-sensitized solar cells with ferrocene-based electrolytes. *Nat. Chem.*, 3:211–215, 2011.

[159] Paolo Salvatori, Gabriele Marotta, Antonio Cinti, Chiara Anselmi, Edoardo Mosconi, and Filippo De Angelis. Supramolecular Interactions of Chenodeoxycholic Acid Increase the Efficiency of Dye-Sensitized Solar Cells Based on a Cobalt Electrolyte. *J. Phys. Chem. C*, 117(8):3874–3887, 2013, http://pubs.acs.org/doi/pdf/10.1021/jp4003577.

[160] Joel Rosenthal, Alexander B. Nepomnyashchii, Julia Kozhukh, Allen J. Bard, and Stephen J. Lippard. Synthesis, Photophysics, Electrochemistry, and Electrogenerated Chemiluminescence of a Homologous Set of BODIPY-Appended Bipyridine Derivatives. *J. Phys. Chem. C*, 115:17993–18001, 2011.

[161] Kristine Kilsa, Elizabeth I. Mayo, Bruce S. Brunschwig, Harry B. Gray, Nathan S. Lewis, and Jay R. Winkler. Anchoring Group and Auxiliary Ligand Effects on the Binding of Ruthenium Complexes to Nanocrystalline TiO_2 Photoelectrodes. *Journal of Physical Chemistry, B*, 108:15640–15651, 2004.

[162] Paul J. Giordano, C. Randolph Bock, Mark S. Wrighton, Leonard V. Interrante, and Raymond F. X. Williams. Excited State Proton Transfer of a Metal Complex: Determination of the Acid Dissociation Constant for a Metal-to-Ligand Charge Transfer State of a Ruthenium(I1)Complex. *J. Am. Chem. Soc.*, 99:3187–3189, 1977.

[163] Julien Warnan, Yann Pellegrin, Errol Blart, Fabrice Odobel, Wei Zhang, Bin Liu, Veluru Jagadesh Babu, and Seeran Ramakrishna. Application of Poly(2-hexylthiophene) Functionalized with an Anchoring Group in Dye-Sensitized Solar Cells. *Macromol. Rapid Commun.*, 32:1190–1194, 2011.

[164] Paul C Hiemenz and Raj Rajagopalan. *Principles of Colloid and Surface Chemistry*. CRC Press, third edition, 1997.

[165] Adam S. Huss, Andrew Bierbaum, Raghu Chitta, Darren J. Ceckanowicz, Kent R. Mann, Wayne L. Gladfelter, and David A. Blank. Tuning Electron Transfer Rates via Systematic Shifts in the Acceptor State Density Using Size-Selected ZnO Colloids. *J. Am. Chem. Soc.*, 132(40):13963–13965, 2010.

[166] Kevin Tvrdy, Pavel A. Frantsuzov, and Prashant V. Kamat. Photoinduced electron transfer from semiconductor quantum dots to metal oxide nanoparticles. *Proc. Nat. Acad. Sci.*, 108(1):29–34, 2011.

[167] István Robel, Masaru Kuno, and Prashant V. Kamat. Size-Dependent Electron Injection from Excited CdSe Quantum Dots into TiO_2 Nanoparticles. *J. Am. Chem. Soc.*, 129(14):4136–4137, 2007.

[168] R. A. Marcus. On the Theory of Oxidation-Reduction Reactions Involving Electron Transfer. I. *J. Chem. Phys.*, 24(5):966–978, 1956.

[169] Gerhard L. Closs and John R. Miller. Intramolecular Long-Distance Electron Transfer in Organic Molecules. *Science*, 240(4851):440–447, 1988.

[170] Mark Spitler and B. A. Parkinson. Dye sensitization of single crystal semiconductor electrodes. *Acc. Chem. Res.*, 42(12):2017–2029, 2009.

[171] Michael Grätzel. Photoelectrochemical cells. *Nature*, 414:338–344, 2001.

[172] David F. Watson and Gerald J. Meyer. Electron Injection at Dye-Sensitized Semiconductor Electrodes. *Annu. Rev. Phys. Chem.*, 56:116–156, 2005.

[173] Thomas W. Hamann, Rebecca A. Jensen, Alex B. F. Martinson, Hal Van Ryswyk, and Joseph T. Hupp. Advancing beyond current generation dye-sensitized solar cells. *Energy Environ. Sci.*, 1:66–78, 2008.

[174] James C. Phillips, Rosemary Braun, Wei Wang, James Gumbart, Emad Tajkhorshid, Elizabeth Villa, Christophe Chipot, Robert D. Skeel, Laxmikant Kale, and Klaus Schulten. Scalable molecular dynamics with NAMD. *Journal of Computational Chemistry*, 26:1781–1802, 2005.

[175] B.R. Brooks, R.E. Bruccoleri, D.J. Olafson, D.J. States, S. Swaminathan, and M. Karplus. CHARMM: A Program for Macromolecular Energy, Minimization, and Dynamics Calculations. *Journal of Computational Chemistry*, 4:187–217, 1983.

[176] A.D. MacKerel Jr., C.L. Brooks III, L. Nilsson, B. Roux, Y. Won, and M. Karplus. *CHARMM: The Energy Function and Its Parameterization with an Overview of the Program*, volume 1 of *The Encyclopedia of Computational Chemistry*, pages 271–277. John Wiley & Sons: Chichester, 1998.

[177] Stefania Rapino and Francesco Zerbetto. Dynamics of Thiolate Chains on a Gold Nanoparticle. *Small*, 3:386–388, 2007.

[178] Pradip Kr. Ghorai and Sharon C. Glotzer. Molecular Dynamics Simulation Study of Self-Assembled Monolayers of Alkanethiol Surfactants on Spherical Gold Nanoparticles. *J. Phys. Chem. C*, 111:15857–15862, 2007.

[179] Robert J. B. Kalescky, Wataru Shinoda, Preston B. Moore, and Steven O. Nielsen. Area per Ligand as a Function of Nanoparticle Radius: A Theoretical and Computer Simulation Approach. *Langmuir*, 25:1352–1359, 2009.

[180] Alberto Jimenez, Antonio Sarsa, Manuel Blazquez, and Teresa Pineda. A Molecular Dynamics Study of the Surfactant Surface Density of Alkanethiol Self-Assembled Monolayers on Gold Nanoparticles as a Function of the Radius. *J. Phys. Chem. C*, 114:21309–21314, 2010.

[181] Andrew Hung, Steve Mwenifumbo, Morgan Mager, Jeffrey J. Kuna, Francesco Stellacci, Irene Yarovsky, and Molly M. Stevens. Ordering Surfaces on the Nanoscale: Implications for Protein Adsorption. *J. Am. Chem. Soc.*, 133:1438–1450, 2011.

[182] Joseph R. Sachleben, Vicki Colvin, Lyndon Emsley, E. Wrenn Wooten, and A. Paul Alivisatos. Solution-State NMR Studies of the Surface Structure and Dynamics of Semiconductor Nanocrystals. *J. Phys. Chem. B*, 102:10117–10128, 1998.

[183] Dongchul Lim, David A. Hrovat, Weston Thatcher Borden, and William L. Jorgensen. Solvent Effects on the Ring Opening of Cyclopropanones to Oxyallyls: A Combined ab Initio and Monte Carlo Study. *J. Am. Chem. Soc.*, 116:3494–3499, 1994.

[184] William L. Jorgensen, James M. Briggs, and M. Leonor Contreras. Relative Partition Coefficients for Organic Solutes from Fluid Simulations. *J. Phys. Chem.*, 94:1683–1686, 1990.

[185] Xavier de Hatten, Zoe Cournia, Ivan Huc, Jeremy C. Smith, and Nils Metzler-Nolte. Force-Field Development and Molecular Dynamics Simulations of Ferrocene-Peptide Conjugates as a Scaffold for Hydrogenase Mimics. *Chem. Eur. J.*, 13:8139–8152, 2007.

[186] Irving Langmuir. The adsorption of gases on plane surfaces of glass, mica and platinum. *J. Am. Chem. Soc.*, 40(9):1361–1403, 1918, http://pubs.acs.org/doi/pdf/10.1021/ja02242a004.

[187] Yunfeng Lu, Dae-jin Choi, Jimmy Nelson, O-Bong Yang, and B. A. Parkinson. Adsorption, Desorption, and Sensitization of Low-Index Anatase and Rutile Surfaces by the Ruthenium Complex Dye N3. *J. Electrochem. Soc.*, 153(8):E131–E137, 2006.

[188] Akiko Fillinger and B. A. Parkinson. The Adsorption Behavior of a Ruthenium-Based Sensitizing Dye to Nanocrystalline TiO_2: Coverage Effects on the External and Internal Sensitization Quantum Yields. *J. Electrochem. Soc.*, 146(12):4559–4564, 1999.

[189] Akiko Fillinger, David Soltz, and B. A. Parkinson. Dye Sensitization of Natural Anatase Crystals with a Ruthenium-Based Dye. *J. Electrochem. Soc.*, 149(9):A1146–A1156, 2002.

[190] Lou Strong and George M. Whitesides. Structures of Self-Assembled Monolayer Films of Organosulfur Compounds Adsorbed on Gold Single Crystals: Electron Diffraction Studies. *Langmuir*, 4:546–558, 1988.

[191] Muriel K. Corbierre, Neil S. Cameron, and R. Bruce Lennox. Polymer-Stabilized Gold Nanoparticles with High Grafting Densities. *Langmuir*, 20:2867–2873, 2004.

[192] Gretchen A. DeVries, Markus Brunnbauer, Ying Hu, Alicia M. Jackson, Brenda Long, Brian T. Neltner, Oktay Uzun, Benjamin H. Wunsch, and Francesco Stellacci. Divalent Metal Nanoparticles. *Science*, 315:358–361, 2007.

[193] Michael J. Hostetler, Allen C. Templeton, and Royce W. Murray. Dynamics of Place-Exchange Reactions on Monolayer-Protected Gold Cluster Molecules. *Langmuir*, 15:3782–3789, 1999.

[194] L. Lovasz, J. Pelikan, and K. Vesztergombi. *Discrete Mathematics: Elementary and Beyond*. Springer Science, 2003.

[195] Iwao Yamazaki, Naoto Tamai, and Tomoko Yamazaki. Electronic Excitation Transfer in Organized Molecular Assemblies. *J. Phys. Chem.*, 94:516–525, 1990.

[196] E.B. Saff and A.B.J. Kuijlaars. Distributing many points on a sphere. *The Mathematical Intelligencer*, 19(1):5–11, 1997.

Appendix A

Derivation of Two-Component Stern-Volmer Model

In light of the breakdown of the simple Stern-Volmer model of static quenching [151] in the case of two separate quenching mechanisms, it is clear that modifications to the model are required. A two-component Stern-Volmer equation needs to be derived. There are numerous situations where this would be useful, but we are unable to find previous reports of its derivation.

Finding the analytical form of the two-component Stern-Volmer requires definition of two separate Stern-Volmer constants for static quenching. We define them in an identical way as is done in the case of the one-component static quenching Stern-Volmer, as outlined in Lakowicz' fluorescence spectroscopy book.[151] $[F : Q]$ refers to a dye molecule bound to a quencher, which in this case is the CdS nanoparticle surface.

$$K_{S1} = \frac{[F : Q_1]}{[Q_1][F]} \tag{A.1}$$

and

$$K_{S2} = \frac{[F : Q_2]}{[Q_2][F]} \tag{A.2}$$

From these two elementary equilibrium constants, we can define a new constant:

$$\frac{K_{S1}}{K_{S2}} = \frac{[F : Q_1][Q_2]}{[Q_1][F : Q_2]} = K \tag{A.3}$$

Conservation of mass requires that the total concentration of dye molecule, $[F]_T$ is described in this way:

$$[F]_T = [F] + [F : Q_1] + [F : Q_2] \tag{A.4}$$

which can be rearranged to yield

$$[F : Q_1] = [F]_T - [F] - [F : Q_2] \tag{A.5}$$

The quantity $[F : Q_1]$ is then substituted into Eq. A.3

$$K = \frac{[Q_2][F]_T - [F][Q_2] - [F : Q_2][Q_2]}{[Q_1][F : Q_2]} \tag{A.6}$$

and this expression can be rearranged to yield

$$\frac{[F]_T[Q_2]}{[Q_1][F : Q_2]} = -K - \frac{[Q_2][F]}{[Q_1][F : Q_2]} - \frac{[F : Q_2][Q_2]}{[Q_1][F : Q_2]} \tag{A.7}$$

Dividing both sides by $\frac{[Q_2]}{[Q_1][F:Q_2]}$ gives

$$[F]_T = \frac{K[Q_1][F : Q_2]}{[Q_2]} + [F] + [F : Q_2] \tag{A.8}$$

which can be then divided by $[F]$ to yield Eq. A.9. Because the quantity $[F]_T$ corresponds to I_o and $[F]$ corresponds to I, Eq. A.9 has the proper LHS for a Stern-Volmer equation:

$$\frac{[F]_T}{[F]} = \frac{K[Q_1][F : Q_2]}{[F][Q_2]} + 1 + \frac{[F : Q_2]}{[F]} \tag{A.9}$$

Substituting K_{S2} from Eq. A.2 provides

$$\frac{[F]_T}{[F]} = KK_{S2}[Q_1] + K_{S2}[Q_2] + 1 \tag{A.10}$$

Given that $K = \frac{K_{S1}}{K_{S2}}$, the derivation of the two-component Stern-Volmer produces a simply formed result,

$$\frac{[F]_T}{[F]} = K_{S1}[Q_1] + K_{S2}[Q_2] + 1 \tag{A.11}$$

Appendix B

Special Procedures and Adapted Parameters for MD Simulations

B.1 Calculation of Head Group Size of Carboxylate

A simple geometric calculation can be performed which will provide the projected area that the headgroup (a carboxylate) will occupy on the surface. In this calculation the van der Waals radius of the oxygen atom is used for the effective radius, which is 1.70 Å. The distance between centers of oxygen atoms on the surface is determined by the O-C-O angle (123°, as per Table B.3) and the C-O distance (1.28 Å, as per Table B.2). The distance between oxygen atom nuclei is 2.25 Å, meaning that the oxygen atoms are slightly overlapping in their projected area on the surface. This means that the overlapping area must be subtracted so that it is not double counted. The overlapping area can be calculated by basic geometric reasoning. This quantity is 2.03 $Å^2$. The final area for a carboxylate group projected onto a surface calculated in this simple fashion is 16.13 $Å^2$.

B.2 Minimization of Coulombic Repulsions

The problem of spacing points evenly on a sphere does not have a closed-form analytical solution. However, the procedure to carry out the distribution on a sphere's surface using numerical techniques has been described earlier.[196] Here, we use a similar technique.

Fourteen particles with a charge of +0.10 and mass 16 AMU were placed in random locations on the surface of a sphere of radius 0.25 nm. The fourteen ions were then allowed to move on the surface of the sphere at 0 K in order to minimize the Coulombic energy of the system. After 3,000 steps of minimization, the system of ions had reached a minimum of the potential energy surface, and the calculations were stopped at the $10{,}000^{\text{th}}$ step. During the simulation, the ions were constrained to the surface by very large harmonic force constants (9999.99 kcal/mol).

This system was replicated many times, each time upwardly incrementing the number of ions on the surface, until the number of ions on the surface was in the hundreds. The output of these simulations provided the positions where a given number of objects could maximize their distances from one another on the surface of a sphere.

B.3 Initial Guess Details

Given that the n-Bu groups on the 3' and 4' positions extend outwards from the molecule, concern is warranted that upon their initial placement next to other molecules atoms in these groups may become superimposed with atoms from other molecules. Especially concerning is the possibility that the alkyl chains will penetrate the ring structures of the neighboring terthiophene molecules. This configuration will show only slightly elevated energies, as opposed to huge energy increases in the case where atoms are superimposed. This makes detection of such a problem difficult and for this reason, we have taken action to avoid it. This includes not only spacing the molecules apart on the surface of the sphere (described in previous section), but also starting the molecules further out from the center of the sphere than what their harmonic constraining potentials dictate. For the case of the 0.75 nm radius spheres, the carboxylate oxygen atoms were started 1.0 nm from the sphere's center, for 0.88 nm spheres, the carboxylate oxygen atoms were started 1.4 nm from the sphere's center, and for 1.0 nm radius spheres, the carboxylate oxygen atoms were started 1.5 nm from the sphere's center.

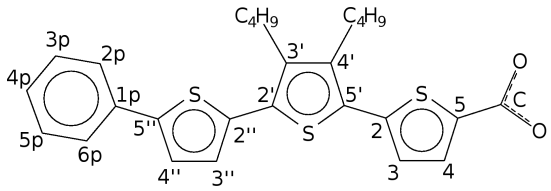

Figure B.1: Terthiophene molecule with labels for positions

B.4 Special Parameters

The CHARMM potential [175,176], described by Eq. B.1, is used to calculate the terthiophene dye molecule's bonded energies as well as the intra- and intermolecular Coulombic and Lennard-Jones energies.

$$V = \sum_{\text{bonds}} k_b(b - b_o)^2 + \sum_{\text{angles}} k_\theta(\theta - \theta_o)^2 + \sum_{\text{dihedrals}} k_\phi[1 + \cos(n\phi - \delta)] + \sum_{ij} \epsilon_{ij} \left[\left(\frac{R_{\text{min,ij}}}{r_{ij}} \right)^{12} - 2 \left(\frac{R_{\text{min,ij}}}{r_{ij}} \right)^{6} \right] + \sum_{ij} \frac{q_i q_j}{r_{ij}} \tag{B.1}$$

where

$$R_{\text{min,ij}} = R_{\text{min,i}}/2 + R_{\text{min,j}}/2 \tag{B.2}$$

and

$$\epsilon_{ij} = \sqrt{\epsilon_{\text{ii}} \epsilon_{\text{jj}}} \tag{B.3}$$

Special parameters were used for the terthiophene dye molecule and these atom types are shown in Table B.1. Table B.1 also contains the atom-specific parameters for all the atoms in the dye molecule, Table B.2 contains the bonding parameters, Table B.3 contains the angle bending parameters, and Table B.4 contains the dihedral/torsional parameters.

Table B.1: Atom types, and parameters for the atoms as labeled in Fig. B.1

Position	Element	Type	$R_{\min}/2$ (Å)	Charge	Mass
1,1',1"	Sulfur	SG2O3	2.0000	-0.100	32.0650
3,4,3',4',3",4"	Carbon	CG2R51	2.1000	-0.240	12.0107
3,4,3',4',3",4"	Hydrogen	HGR51	1.3582	0.170	1.0079
2,5,2',5',2",5"	Carbon	CG2R51	2.1000	0.120	12.0107
1p	Carbon	CG2R67	1.9924	0.000	12.0107
2p-6p	Carbon	CG2R61	1.9924	-0.115	12.0107
2p-6p	Hydrogen	HGR61	1.3582	0.115	1.0079
Methylene	Carbon	CTL2	2.010	-0.180	12.0107
Methylene	Hydrogen	HAL2	1.3400	0.090	1.0079
Methyl	Carbon	CTL3	2.040	-0.270	12.0107
Methyl	Hydrogen	HAL3	1.3400	0.090	1.0079
Carboxylate	Carbon	CG2O3	2.0000	0.500	12.0107
Carboxylate	Oxygen	OCL	1.7000	-0.250	15.9994
CH_2Cl_2	CH_2	CH2	2.13300	0.500	14.0268
CH_2Cl_2	Cl	Cl	1.90800	-0.250	35.4530
He	He	He	1.4800	0.000	4.0026

Table B.2: Bond stretching parameters for special bonds

Atom 1	Atom 2	Force Constant	Equilibrium Length (Å)
CO3	C51	200.000	1.4600
CO3	OCL	525.000	1.2800
C51	CT2	229.630	1.5100
C67	C51	305.000	1.4700
CH2	CL	135.394	1.7720

Table B.3: Angle bending parameters for special angles

Atom 1	Central Atom	Atom 3	Force Constant	Equilibrium Angle
CO3	CT2	CT2	52.00	108.00
C51	CO3	OCL	40.00	118.00
CT2	CO3	OG2	40.00	116.00
CO3	CT2	HA2	33.00	109.50
OCL	CO3	OCL	100.00	123.00
CO3	C51	C51	45.00	130.00
CO3	C51	S50	105.00	119.00
C51	C51	CT2	45.80	123.40
C51	CT2	CT2	51.80	114.00
C51	C51	C67	40.00	128.50
C51	C67	C61	40.00	121.00
C67	C51	S50	40.00	121.50
HA2	CT2	C51	55.500	109.50

Table B.4: Dihedral/torsional parameters for special dihedrals

Atom 1	Central Atom	Central Atom	Atom 4	Force Constant	Mult.	Equil. Angle
CO3	CT2	CT2	CT2	0.06450	2	0.00
CO3	CT2	CT2	CT2	0.14975	3	180.00
CO3	CT2	CT2	CT2	0.09458	4	0.00
CO3	CT2	CT2	CT2	0.11251	5	0.00
CO3	CT2	CT2	HA2	0.1950	3	0.00
OG2	CO3	CT2	HA2	0.0500	6	180.00
OG2	CO3	CT2	CT2	0.0500	6	180.00
OCL	CO3	C51	C51	3.1000	2	180.00
OCL	CO3	C51	S50	3.1000	2	180.00
C67	C51	C51	H51	4.2000	2	180.00
C51	C67	C61	H61	4.2000	2	180.00
CT2	C51	C51	C51	3.1000	2	180.00
CO3	C51	C51	C51	3.1000	2	180.00
C51	C51	CT2	HA2	0.0020	6	0.00
C51	C51	CT2	CT2	0.4000	1	0.00
S50	C51	C51	CT2	3.1000	2	180.00
CT2	C51	C51	CT2	2.4000	2	180.00
CO3	C51	C51	H51	2.4000	2	180.00
S50	C51	C51	S50	0.8900	2	180.00
C51	S50	C51	C67	3.1900	2	180.00
C51	C51	C51	C67	3.1900	2	180.00
C51	C51	C67	C61	0.8900	2	180.00
C51	C67	C61	C61	3.1000	2	180.00
S50	C51	C67	C61	0.8900	2	180.00
C51	S50	C51	CO3	3.1000	2	180.00

Appendix C

Glossary and Acronyms

Care has been taken in this thesis to minimize the use of jargon and acronyms, but this cannot always be achieved. This appendix defines jargon terms in a glossary, and contains a table of acronyms and their meaning.

C.1 Glossary

- **Dye Sensitized Solar Cell** (**DSSC**) – A photovoltaic cell that contains a dye molecule that sensitizes a layer of wide band gap semiconductor nanoparticles that otherwise would not absorb sunlight in the visible region.
- **Internal Conversion (IC)** – Relaxation of an excited state, usually from an excited singlet state to a lower energy singlet state.
- **Intersystem Crossing (ISC)** – The formally forbidden process of an excited state going from singlet to triplet, or vice versa.
- **Light Harvesting Efficiency (LHE)** – The wavelength-dependent quantity which represents the quotient obtained when total current output is divided by total photons input, usually at 0 V bias.
- **Photovoltaic (PV) Cell** – A cell that converts incident photons into useful current, generally also at a useful voltage.

- **Solar Cell Efficiency** – The quotient obtained when the total energy output of a solar cell is divided by the total light energy incident upon the cell.
- **Surface Saturation** – The state of the surface of a nanoparticle or other surface in which adsorbates are occupying every possible adsorption site.

C.2 Acronyms

Table C.1: Acronyms

Acronym	Meaning
ac-ZnO	Acetate-Capped ZnO Nanoparticles
BSH	Binding Site Heterogeneity
Bipy	Bipyridine
CQ	Concentration Quenching
DCA	Dicarboxylic Acid Bipyridine
DSSC	Dye Sensitized Solar Cell
E_f	Fermi Level
FF	Fill Factor
FRET	Förster Resonant Energy Transfer
FTIR	Fourier Transformed Infrared [spectroscopy]
HDA	Hexadecylamine
HWHM	Half Width Half Max
I_{mp}	Current at Maximum Power
I_{SC}	Short Circuit Current
IPCE	Incident Photon to Current Efficiency
IR	Infrared [spectroscopy]
LHE	Light Harvesting Efficiency
LUMO	Lowest Unoccupied Molecular Orbital
nc-CdS	Oleate-Capped CdS Nanoparticles
nc-ZnO	Hexylamine-Capped ZnO Nanoparticles

Continued on next page

Table C.1 – continued from previous page

Acronym	Meaning
NMR	Nuclear Magnetic Resonance
NOE(SY)	Nuclear Overhauser Effect (Spectroscopy)
PL	Photoluminescence
SAED	Selected Area Electron Diffraction
SILAR	Successive Ionic Layer Adsorption and Reaction
TCO	Transparent Conductive Oxide
TEM	Transmission Electron Microscopy
UV-Vis	Ultraviolet-Visible [spectroscopy]
V_{mp}	Voltage at Maximum Power
V_{OC}	Open Circuit Voltage
WRT	With Respect To
XRD	X-ray Diffraction